Volume 3 | Issue 1 | Apr 2018

www.ijcoe.org info@ijcoe.org

Journal of Coastal, Offshore and Environmental Engineering (IJCOE) Vol. 3 / Issue. 1 / Apr 2018

9 Volume 3 | Issue 1| Apr 2018

International Journal of Coastal, Offshore & Environmental Engineering

Since 2015

ISSN: 2580-8737 (online)

IJCOE

Editor-in-Chief: Prof. Hamid S.Bahai

International Journal of Coastal, Offshore & Environmental Engineering
Since 2015
ISSN: 2980-8721 (online)

In The Name of God

Message from the Editor-in-Chief

The IJCOE journal office was established in 2015,and its first issue was published in 2016. TheIJCOE covers a wide range of research in thefields of oceanography & ocean technology, aswell as marine industries & marine engineering.The editorial board of IJCOE consists of nearly130 of the greatest scientists and researchersfrom over 30 countries worldwide, and thejournal's review board comprises 1,000 membersfrom all five continents. The membership andapplication process for joining the editorial andreview boards of this journal is ongoing. IJCOE isa research-academic quarterly journal that haspublication and distribution permissions fromthe Press Organization and permission topublish scientific-research articles from theMinistry of Science, Research, and Technology(MSRT) with an "A" rating. It also holds a "Q1"rating from the ISC institute with an impactfactor (IF) of approximately 0.43 and isconsidered a "core journal" (prestigious andoutstanding journal). IJCOE is an open-accessjournal and allows the download and receipt ofaccepted articles in full text for free. It respectsand adheres to copyright and COPE regulations.The journal's office operates 24/7, providingservices to researchers. In addition to publishinga regular quarterly journal, IJCOE has 16 specialissues on specific topics in preparation. It alsoprovides conditions for publishing specializedbooks, references, and handbooks. Moreover, itis ready to cooperate with the secretariats ofreputable international conferences to publishtheir selected and outstanding articles. IJCOEevaluates, appraises, and publishes books,articles, and the scientific achievements andfindings of esteemed researchers and scientistsworldwide who are innovating and conductingin-depth research in the "important and strategicfield of the maritime technology & Oceanengineering." It welcomes any form of jointcooperation with universities, research institutes,and related research centers at the national,regional, and international levels, and extends ahand for collaboration.

Classification of Editorial Board in IJCOE

Editor-in-Chief

Director-in-Chief

Deputy Editor

Executive Managers

English Text Editor

Technical Editor

International Editorial Board

National Editorial Board

Editorial Board Associate

Editorial Board Assistant

Guest Editorial Board

Advisory Board

Administrative Coordinator

Honorary Board Member

Methodology Advisor

Author Benefits

- Open Access
- Rapid Publication
- Thorough Peer-Review
- No Copyright Constraints
- Coverage by Leading Indexing Services
- Discounts On Article Processing Charges (APC)
- No Space Constraints, No restriction on the maximum length of the papers, number of figures or colors

INTERNATIONAL JOURNAL OF IJCOE COASTAL, OFFSHORE & ENVIRONMENTAL ENGINEERING

Aims of IJCOE

Hydrodynamics

Marine equipment

Structural mechanics

Ocean environmental predictions

Stochastic calculations Experimental

Automatic Control of Marine Systems

Scope of IJCOE

Marine Hazards

Ocean Acoustics

Naval Architecture

Ocean Engineering

Coastal Engineering

Marine Meteorology

Marine Earth Sciences

Underwater Technology

Marine Renewable Energy

Polar & Arctic Engineering

Marine Renewable Energy

Marine Geography & Geodesy

Marine Environmental Engineering

Automatic Control of Marine Systems

Hydro Physics & Physical Oceanography

Type of papers

- Case Studies
- Book Reviews
- Review Article
- Letters to the Editor
- Methodology Papers
- Editorials and Commentaries
- Response or Rejoinder Papers
- Perspective or Opinion Papers
- Conceptual or Theoretical Papers
- Meta-Analysis and Systematic Reviews
- Short Communications or Brief Reports
- Research Articles (Original Research Papers)

Scientific Research Journal

Ministry of Science, Research And Technology (MSRT)

Jurnal Ranking 2023: A

Ministry Of Science, Research And Technology (ISC)

Citation Impact 2022: 0.429

Quartile 2022 : Q1

Core Collection

IJCOE is a Member of

Cantact Us

Office 1 | Research Institute of Meteorology and Atmospheric Science

Address | Tehran, Shahid Kharrazi Highway, Pajoohesh Blvd, Research Institute of Meteorology and Atmospheric Science, Sand and Dust Storm International Research Center (SDS-IRC), No. 13, 1st floor.

Phone | +982144787652

Postal code | 13611-14977

website | www.rimac.ac.ir

Office 2 | Iranian National Institute for Oceanography and Atmospheric Science

Address | Tehran, Dr. Fatemi Gharbi St., Shahid Etemadzade St., No. 3, third floor.

Phone | +982166944873

Postal code | 13389 – 14118

website | www.inio.ac.ir

Email | Info@ijcoe.org

Website | www.ijcoe.org

Follow Us

www.ijcoe.org

INTERNATIONAL JOURNAL OF IJCOE COASTAL, OFFSHORE & ENVIRONMENTAL ENGINEERING

Volume & Issue:

Volume 3, Issue 1, April 2018

Number of Articles: 6

Content

INTERNATIONAL JOURNAL OF
COASTAL & OFFSHORE ENGINEERING IJCOE Vol.3/No. 1/Spring 2018 (1-19)

Available online at: http://ijcoe.org/browse.php?a_code=A-10-116-1&sid=1&slc_lang=en

Reliability Assurance of Subsea Production Systems: A Systems Engineering Framework

Sirous Yasseri[1], Hamid Bahai[2], Ramin Yasseri[3]

[1]*PhD Brunel University London; Sirous.Yasseri@Brunel.ac.uk*
[2]*Professor, Brunel University London; Hamid.Bahai@Brunel.AC.Uk*
[3]*MSc Systems engineer Aker Solution London; Ramin.Yasseri@gmail.com*

ARTICLE INFO

Article History:
Received: 16 Jan. 2018
Accepted: 15 May. 2018

Keywords:
Subsea Production system
Reliability Assurance
Systems Engineering Framework
Verification, Validation & Testing
Qualification & Certification

ABSTRACT

Due to the high investment costs for deep-water subsea production systems of high-value subsea fields, it is crucial to ensure a high availability to recover the investment. The problem is compounded by the cost of recovery, repair and replacement of failed equipment. Testing and reliability analyses are two pillars of reliability assurance; neither of them on their own assures the delivery of a reliable system. Possibly with more imaginative use of reliability methods, it is possible to optimise testing. It is suggested to use reliability analysis as a guide for allocating resources for testing. This paper outlines a Systems Engineering Framework to link the Client's requirements for equipment reliability, as a means of proving the desired level of performance. This framework allows a better understanding of verification settings and strategies to handle constraints (e.g. costs, expandability, repair-ability, maintainability, intervention procedures, downtime, automation etc.) and performance measures, to achieve highly reliable production systems. The bilateral links between the Client's requirements and subsea equipment performance are established using the systems engineering V-model. These links relate equipment performance to one or more of the Client's requirements, which helps establish verification and validation testing strategies to enhance reliability and reduce project risk. The proposed procedure also assists risk management efforts by feeding the results of reliability analyses, testing and project risk analysis into validation processes, the systems engineering measurement process ensures enhanced reliability. We define reliability assurance as a part of the systems engineering processes to ensure the continued function and resilience of the production system from the downhole valve to the subsea equipment, housed on the topside or at an onshore terminal, in their operating environment and condition using the "Fit-For-Service" notion.

1. Introduction

High-value subsea production systems rely on high reliability and high availability to avoid loss of revenue since access and downtime are costly. The industry needs a comprehensive and integrative framework to assess and address ways and means of achieving high availability.

The Client sets the required reliability, which is then used to allocate the reliability for each piece of hardware/software. With reliability requirements specified, the primary task is to confirm "by examination and provision of evidence that the hardware (and software) meets the specified requirements for the intended use" (DNV-RP-A203 [8]). When completely new technology is involved, available data is likely to be insufficient, which means that the confidence in the gathered evidence may not be high; thus, more testing may be necessary (Yasseri et al [41]). Reliability may also be reduced by a possible mismatch between specification, design, manufacture, installation, commissioning and use. This means that the predicted performance demonstrated through the qualification process may be different from the actual performance realized in the field. This may be due to emergent behaviour, unidentified failure modes, unanticipated operating conditions, unforeseen failure mechanisms and causes, epistemic uncertainties or aleatory

uncertainties (Pecht [30]). Unanticipated operating conditions are either due to incorrect/inadequate specifications or because of unforeseen changes in the actual well conditions. A scenario-based approach can help to minimise the effect of uncertainties. The 'provision of evidence' is done through functional failure analysis (Viola, et al [34]), and testing; supplemented by experience from proven technologies and physics-based analyses.

The key to assuring system and equipment reliability is the insight gained during the specification writing and design activities, which are used to establish procedures to control the fabrication and manufacturing processes that will result in equipment with the desired quality attributes; specifically

- Understand the sources of variation;
- Detect the presence and degree of variation;
- Understand the impact of variation on the process and hence on the equipment attributes;
- Control the variation in a manner compatible with reliability need of the equipment.

Reliability methods that focus on using historical data to predict mechanical failures imply that design errors have little impact, and assume that all anomalies will be detected during design and fabrication. But design errors offer a challenge to reliability predictions based on historical data only (Feiler, et. al [13]) because it is unrealistic to assume that what we build now is the same as we built in the past. Verification and validation testing are supposed to fill this gap. However, there is a need for a more dependable approach for qualifying a system, rather than "test it until time and budgets are exhausted". Such an approach should allow detecting problems in the Development Phase of the life cycle to assure operational quality attributes, such as performance, timing, safety, reliability, and security. Such an approach must identify defects before a system is built, as well as deal with issues that are hard to test unless the entire system is built. It is necessary to ensure that unavoidable failures are addressed through risk management, providing resilience to counter undetected and emergent behaviour.

The reliability assurance framework which is outlined in this paper utilises systems engineering processes which are generally performed for the project; two of the primary processes are:

- Requirement analysis at the system, subsystem and components levels. Systems requirements are based on the Client's needs and the concept of operation (ConOp)- see INCOSE [20]. System requirements fall into two categories; Firstly, the required capabilities under normal conditions, such as functionality, behaviour, and performance. Secondly, specifying how the system is expected to perform under abnormal conditions, such as resilience and survivability (robustness). Requirements are linked to the concept of operation (ConOp) [20] and flowed down into requirements for subsystems, assemblies and components (Hull et. al [17]).
- System architecture. The subsea industry has recognized that a high reliability starts with the system architecture, i.e. arrangement and packing of components. The architecture should allow access to equipment to be retrieved by Remotely Operated Vehicles (ROVs) with minimal effort and time. Model-based analysis, simulations and analytical approaches can be used to identify problematic areas. The subsea Industry has embraced virtual system integration to achieve validation through Computer Aided Design (CAD) modelling. Analysis of integrated systems and detailed models are used for early discovery of likely problems (Youngblood and Pace[41]).

2. Fitness for Purpose or Service

This paper uses the concept of Fitness-For-Purpose (FFP), which is also referred to as Fit-For-Service (FFS) in this paper. It can be said a system is badly designed if it is not well suited for its intended purpose, i.e. it is not fit for service. The phrase Fit-For-Service is also used in fracture mechanics literature in relation to the size of tolerable cracks. In the paper, this phrase is used to mean for whatever reason is not suitable for service. If a component is added to make the operation safer, but it does nothing, then it is not Fit-For-Purpose. Thus, quality can be defined in terms of Fitness-For-Purpose. This means that the quality cannot be assessed as a measure of the production system itself; quality can only be assessed when considering the production system in the context of what it must do. In other words, hardware on its own cannot be said to be of 'high quality' or of 'low quality', because the quality is an attribute of the relationship between hardware and the purpose for which it is used. The purpose of a system, and hence the key quality measures, appear to be self-evident. For example, it is hard to imagine a purpose for a subsea control system that does not allow shut down the system in an emergency as safely as practicable. Most systems have multiple purposes, and those purposes change over time. Thus, conditions under which a system must work, and the intended purpose, must be properly understood.

With a notion of "Fitness-For-Purpose", one can consider and challenge the comprehensiveness and relevance of purposes to ensure improvements. FFP equates quality with the fulfilment of a specification or stated goal. It attempts to validate a product for its intended use. The purpose may be that as determined by the safety, reliability and quality requirements, which are in turn based on the needs of customers. Thus, FFP is fulfilling customers' requirements, which is one of the possible criteria for establishing whether a unit meets quality, measured against what is seen to be the goal of the unit. This definition

subsumes value for money under fitness for purpose. However, affordability or cost-effectiveness criteria are not a necessary element of Fitness-For-Purpose.

Fitness-For-Purpose has emerged as the fashionable way to harness the drive for perfection, i.e. zero defects. The ultimate measure of perfection, 'zero defects', may be excellent as a definition of quality but runs the fatal risk of being perfectly impractical. If the product does not fit its purpose, then its perfection is irrelevant.

A major weakness of the FFP concept is that it may seem to imply that "anything goes" so long as a purpose can be formulated for it. This weakness is more likely to be exacerbated in a large organisation with a range of "purposes" to minimise CAPEX or/and OPEX, which are controlled by different business units. Such separation of decision makers will lead to complications in building installations in various jurisdictions with different regulations. Although straightforward in conception, "Fitness for Purpose" is deceptive, for it raises the issue of whose purpose and how fitness is assessed? Thus, this paper replaces "Fitness-For-Purpose", with "Fitness-For-Service", since while FFP is unclear FFS is obvious. FFS is assessed for the entire lifecycle (ISO/IEC 15288, 2008 [23]). In the literature on the acceptability of flaws in welded component FFS is used to mean the largest size of a crack a component can contain while can be used in service. The usage of FFS in this paper is much wide and include every type of flaw.

Proving a system's Fitness-For-Service requires gathering evidence. This involves the development of evidence in parallel with the system design throughout the Development Phase of the life cycle. Such evidence includes: requirements and design reviews, results from the predictive analysis, simulation results and test results to provide justified confidence in the built system. This approach documents claims about the system, assumptions made in the process, and evidence required to satisfy these claims.

3. The State of Practice

Several codes of practice, as well guidance notes from the classification society have been published in recent years; e.g. API, 17N [3] & 17Q [4], DNV-RP-A203 [8], Bureau VERITAS [7], ABS [2], and Lloyds Register [25]. Figure 1 shows DNV-RP-A203 [8] procedure.

Although, these standards and guidance notes primarily address "New Technology", the definition of the new technology includes almost everything in a new site, and even includes some sites with a previous history. The term 'Technology' refers to equipment that uses a physical law to perform a function. Both equipment and its physics must be qualified. Where subsea equipment is the marinized version of topside equipment, hardly any new physics is involved, then it is the equipment only that requires qualification.

The primary method for proving the 'claim' that a piece of equipment is qualified, is by gathering valid evidence (Yasseri [40]) which proves the equipment will function within specific limits and with an acceptable level of confidence (Woody, et al [35]). This is obtained by a combination of modelling, simulation, physics-based analytical & numerical methods, reliability methods (FMECA, RAM, Reliability Block Diagrams, etc. see e.g. IAEA [14]), risk assessments and tests. API codes (API RP 17N [3], and 17Q [4]) follow a similar line with some deviation (Figure 2).

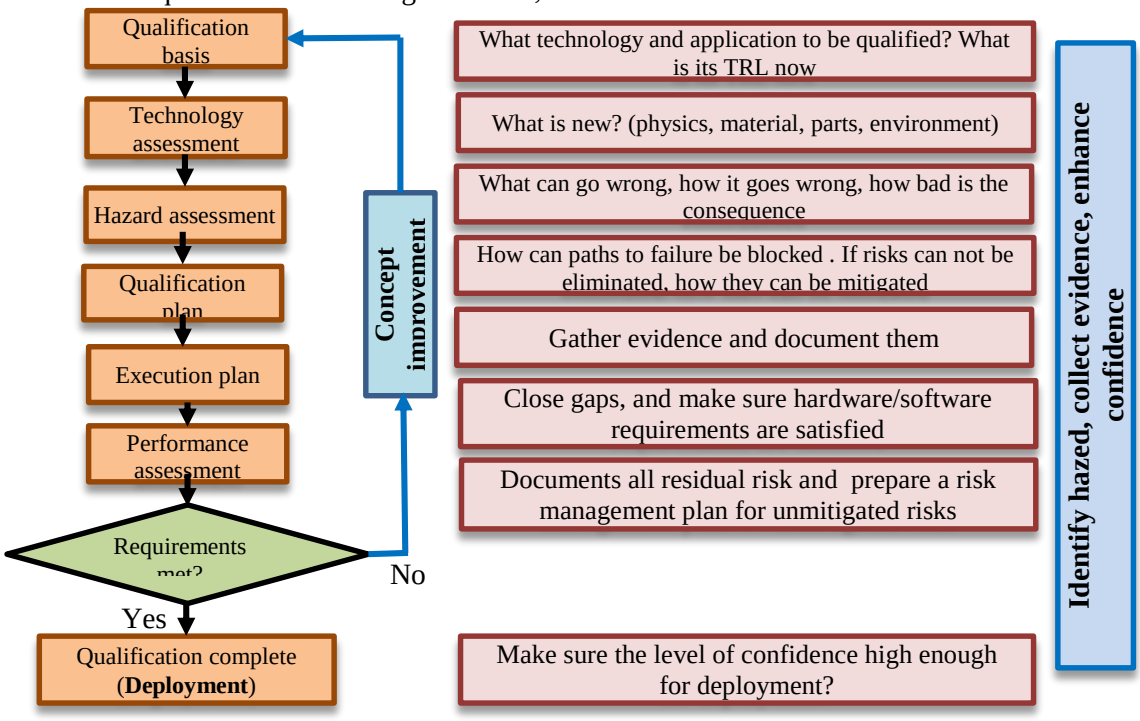

Figure 1: DNV-RP-A203 [8] Technology Qualification Process (TQP).

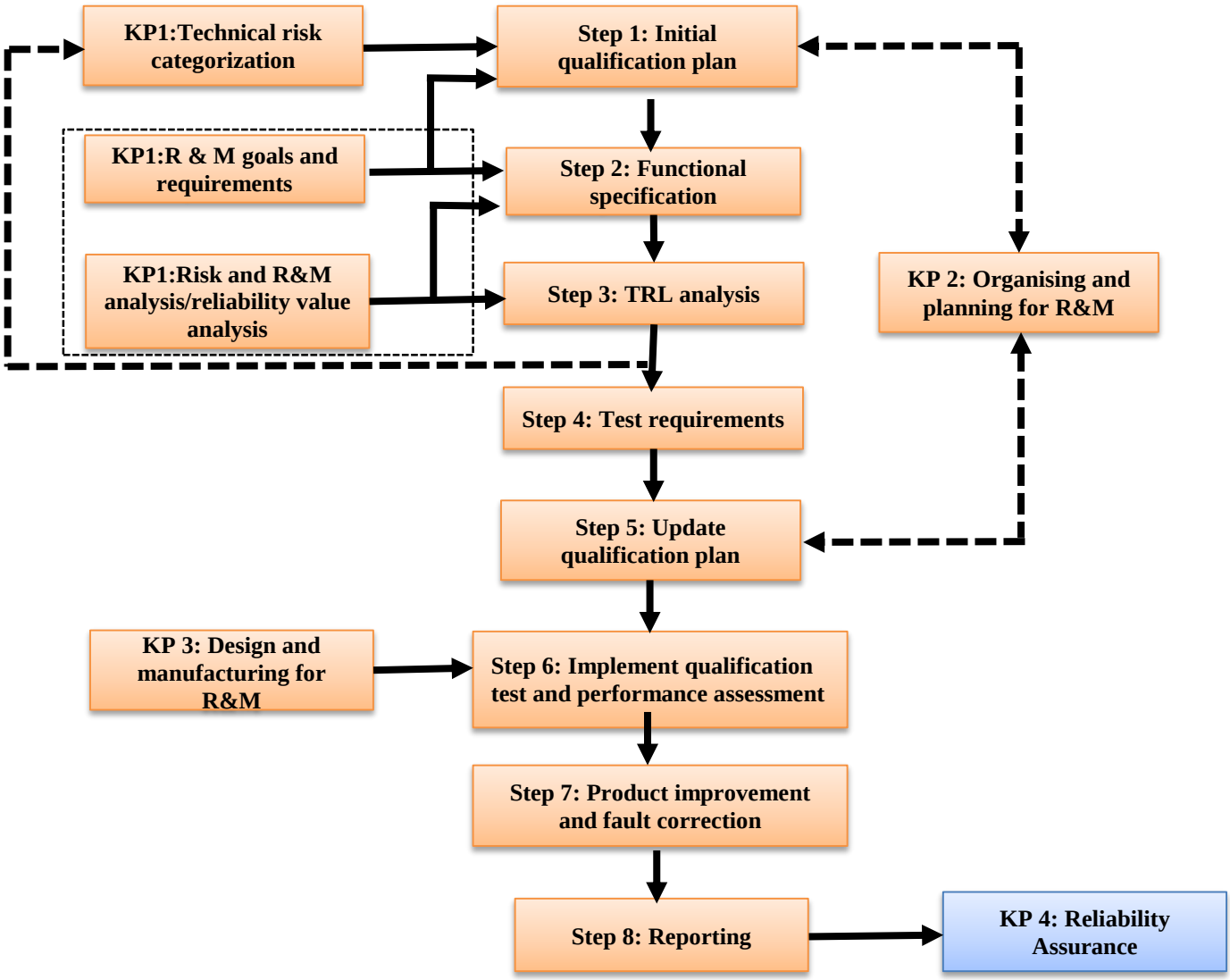

Figure 2: API 17N [3] Technology qualification process

API 17N [3] lists 12 Key Process (KPs) to provide a supportive environment for achieving reliability by managing an appropriate level of reliability throughout the lifecycle of a subsea field (Figure 3).

The philosophy behind codified recommendations is technology may undergo a step change or gradually evolve to meet efficiency, reliability and safety needs. Materials or parts may be different in two pieces of equipment designed by the same manufactures even using the same physical laws. For example, even existing, proven technology may be required to operate in more challenging environments; beyond existing industry experience. When this happens, additional technical risks and performances may be uncertain. One way to manage these risks is through analysis, qualification and testing.

The intent is to provide traceable evidence that systems are qualified through a detailed understanding of service demands, performance requirements and potential failure mechanisms.

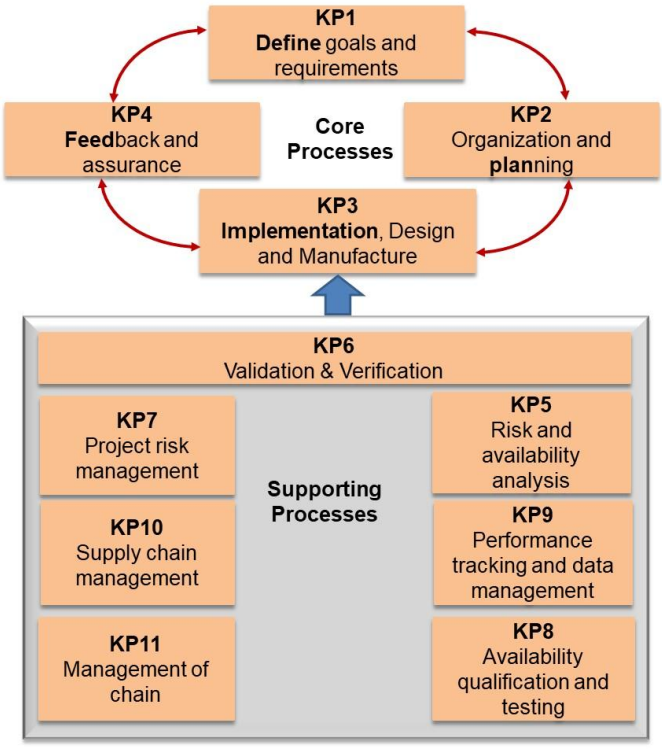

Figure 3: 12 Key Process (KPs) of API 17N and their relationship

According to API RP 17N [3], Reliability Qualification and Testing is a systematic technical risk assessment and risk management approach which includes:

- Definition of technology requirements (includes risk and reliability requirements);
- Identification of technology failure modes and mechanisms;
- Assessment of failure criticality (risk consequences), to determine relevant actions taken to reduce risk and uncertainties;
- Testing to demonstrate functional performance;
- Technology Readiness Level (TRL) to indicate the extent to which an item is "ready for use", given specified qualification factors/requirements;
- Use of test data to estimate reliability.

API RP 17N [3] is a high-level philosophy, while DNV RP A203 [8] is a detailed guidance. The primary focuses of these codes API RP 17N are:

- Focusing on reliability activities such as Reliability Qualification and Testing (KP8);
- Considering operational reliability failures.

Note: Reliability engineering doesn't consider reputation/commercial, safety, and environmental risks.

DNV-RP-A203 [8] defines qualification as "confirmation by examination and provision of evidence that the new technology meets the specified requirements for the intended use." The primary focuses of DNV-RP- A203 [8] are:

- Reliability - this is one of the targets along with performance, safety, environment and other project specific requirements included in the Qualification Basis document;
- Consideration of all types of failures;
- Flexibility to include project specific requirements such as high pressure and high-temperature readiness.

The embed intention of all codes (Hother and Hebert, [16]) are:

- Risk reduction to increase the probability of success;
- Ensuring that the product is "Fit-For-Purpose" before insertion into the system;
- The early part of qualification (FAT and EFAT) are performed by the producer and witnessed by the Client or a third party. SAT and SIT are performed by specialist Contractors appointed by the Client;
- System tests and acceptance tests are performed by the Primary Design Contractor in collaboration with the Client's Operations Team.
- A vendor, who offers a new equipment, is required to provide a proof of fitness for purpose.

According to this definition, qualification means verification& validation.

Systems engineering qualifications (known as verifications and validation (V&V)) are performed by a combination of analytical and numerical methods and testing. At the design stage, mostly analytical methods (FE and CFD) are used, after manufacturing a plethora of tests are used.

The list of methodologies to collect evidence for the reliability assurance is long, and there is some overlap between them. Any procedure is chosen, as well the extent of details is on the 'need' basis and they are situation dependent. The list includes activities which are part of the design and are naturally indispensable. The hypothesis is that the design methods, however exhaustive they are, cannot tease out all probable causes of failure beyond a reasonable probability. Rational choices are required to avoid activities yielding little value. However, at least two different approaches are needed to trap a fault. Any single procedure may be necessary but not sufficient on its own. Analyses and simulation may be used to reduce the number of tests that would be needed to assure the desired system dependability. They can also replace testing when testing would be impossible or expensive.

4. Systems Engineering V-Model

Systems Engineering (SE) is the art and science of developing an operable system capable of meeting the Client's requirements within opposing constraints. SE is a holistic, integrative discipline, wherein the contributions of the Subsea Engineers, Structural Engineers, Electrical Engineers, Mechanical Designers, Power Engineers, Control Engineers, and many more disciplines are evaluated and balanced, to produce a coherent design that is not dominated by the perspective of a single discipline. (see e.g. NASA Systems engineering Handbook [28],). An alternative definition is: Systems Engineering is an iterative process of top-down synthesis, development, and operation of a real-world system that satisfies, in a near optimal manner, the full range of requirements for a system. (INCOSE Systems Engineering Handbook [20])

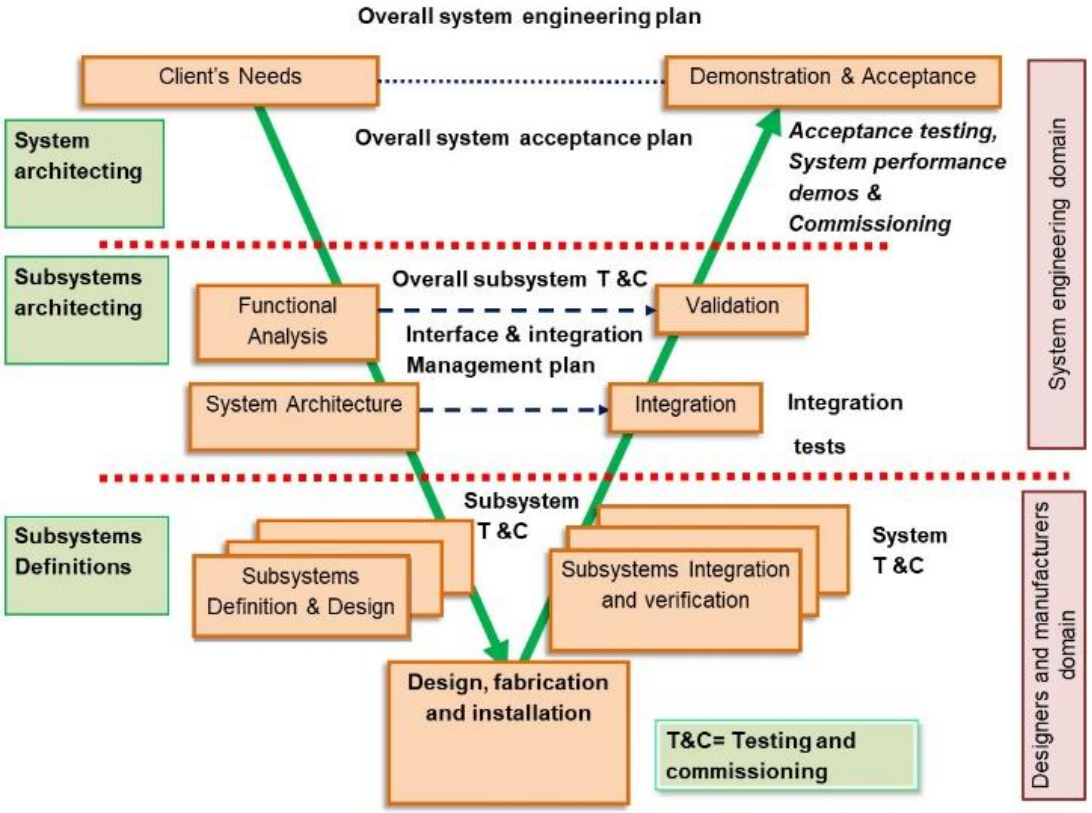

Figure 4: SE V-model for product development

The V-model is one of several models used in SE to visualise the process of a project development. The V-model describes the activities and results that must be produced during development (Figure 4). The left tail of the V represents the *system specification stream*, where the system requirements and the system and subsystem or component designs are specified. The designed components are then fabricated and installed at the bottom of V. Component fabrication is followed by the *testing stream* in the right tail of the V, where the gradually evolving and growing system is verified against the specifications defined in the right tail of the V.

Certain subsystems of the SPS are outsourced to suppliers. These suppliers conduct the complete design, development and testing of the subsystem, and deliver the finished product to the site. Thus, in these cases, the development of the subsystem can be considered as an independent project.

The V-model separates the disciplines of systems and component engineering. This way, *top-down* and *bottom-up* development approaches are integrated into the V-model. That is, the system is specified top-down and then the subsystems are integrated bottom up. Additionally, the definition of distinct steps for the design, at different hierarchy levels, appears first in the V-model and enables breaking down of the system into independent subsystems. The Client's ConOps [20 and 28] are also reviewed, analysed, and transformed into verifiable requirements that define *what* the system will do, not *how* the system will do it, i.e. OpsCon [20 and 28]. Working closely with the Client Engineers, the requirements are elicited, analysed, validated, documented, and base-lined. The Client's specifications describe what, why and purpose. This ensures that the facility, or equipment, can be used for production as the Client required.

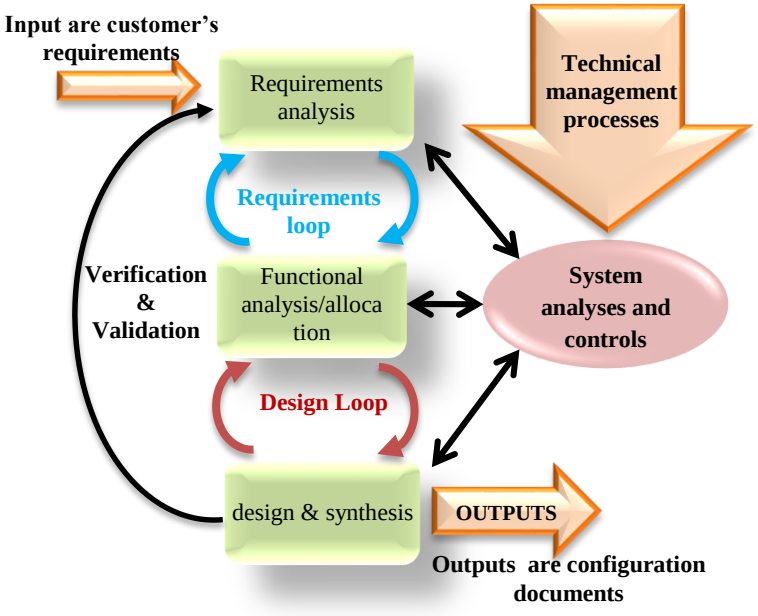

Figure 5: Loops of the development process. See also Figure 6 for details

The system is then decomposed (broken down) into functional subsystems, which are easier to handle. Subsystems can then be designed and fabricated *in parallel*, according to the system specifications defined in the previous phase. When it comes to the

development of highly complex systems, the independent, concurrent development of subsystems is a great way to accelerate the project pace and supports a better involvement of vendors.

Another benefit of the V-model is that it breaks down system definition and V&V into three separate stages (Figure 5). These three main stages, shown in the right tail of the V in Figure 4, form three iteration loops in the development of the system with increasing scope and complexity (Figure 5). The first design loop is at the component or subsystem level. In case of a modular design, the subsystem verification can be performed in parallel, independently of each other. That is the three phases of component design, fabrication, and verification in the bottom of the V consist of numerous parallel Vs, as many as subsystems that are built into the system.

The second loop of system design involves system-level design verification. In this loop, the integrated design is verified against the system specifications delivered in the second Lifecycle Phase in the left tail of the V. Unambiguous and robust subsystem and interface specifications, and a thorough subsystem-level verification facilitates the system-level verification. The third and last design iteration loop in the V-model is the system validation loop, also called system qualification. The outcome of this usually requires a very long, expensive, and comprehensive test procedures that have the objective to prove the developed system satisfies the customer's needs, as well as industry standards and government regulations.

5. Requirement Analysis

Quality only has a meaning in relation to the purpose of the product or service. If something does the job for which it is designed (FFS), then it is a quality product or service.

A subsea project starts when the business case is made during the Appraisal Phase (Yasseri [38]). Technical, economic, and political feasibility is assessed; benefits and costs are estimated, and key risks are identified. In the next phase, known as the Select Phase, alternative concepts which meet the project's purposes and needs are explored, and the best concept is selected and justified using trade-off studies. The project stakeholders reach a shared understanding of the system to be developed and how it will be operated and maintained. The Concept of Operation (ConOps) is documented to provide a foundation for the more detailed analyses that will follow. This will be the basis for the system requirements that are developed in the next step.

Figure 6 shows three loops of a product development with more details. The first loop is the requirements that express the purpose of a system. How well a system fulfils its purpose, or how well it suits its purpose, indicating how good a system is if it is designed in a specific way.

Requirements analysis provides a framework for understanding the purpose of a system and the contexts in which it will be used. It bridges the gap between, an initial vague recognition that there is a need to which subsea engineering can be applied, and the task of building a system to address such a need (Figure 7).

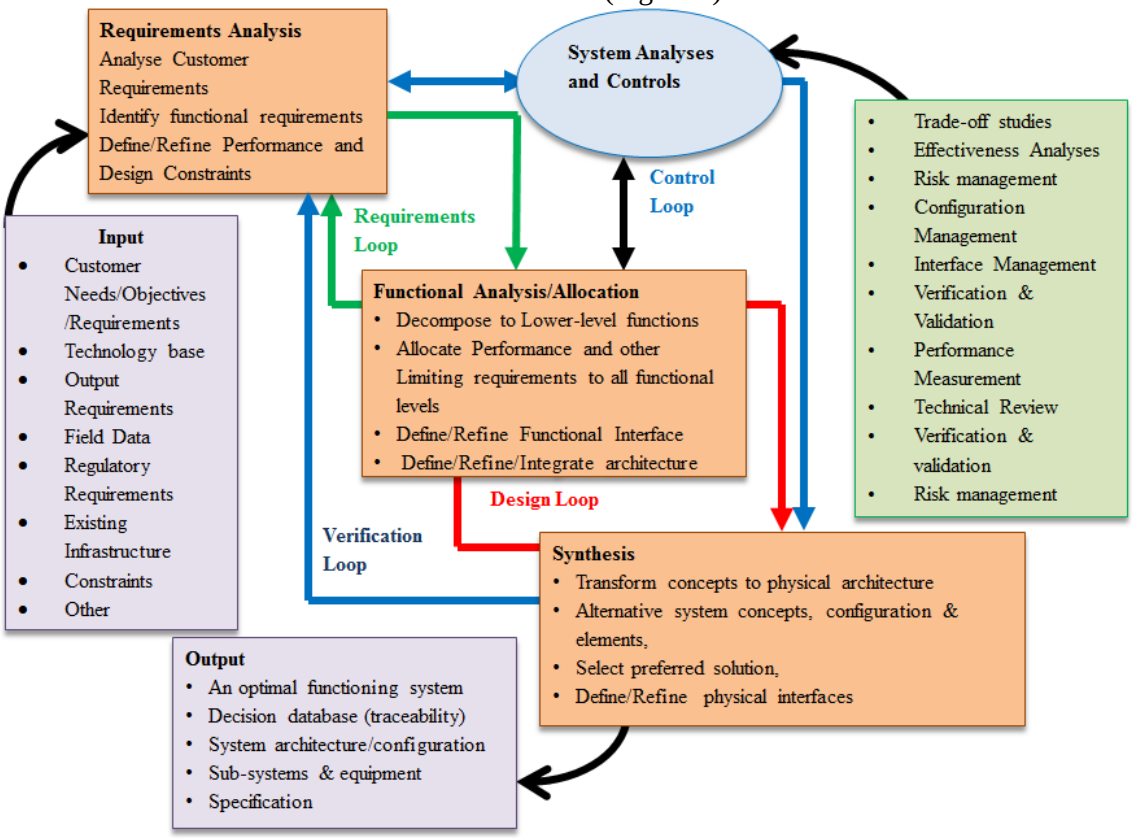

Figure 6: Three loops to reach the implementation stage (adapted from NASA's Handbook [28]). See also Figure 5.

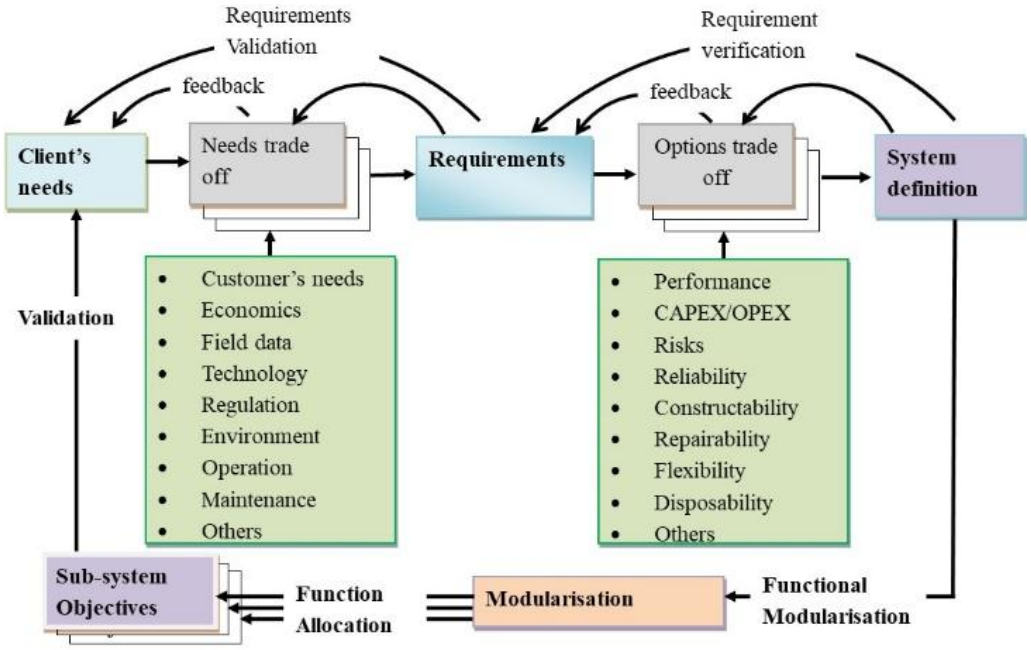

Figure 7: The expanded requirement loop (Figure 5) of Systems engineering process as applied to the subsea development

In seeking to describe the purpose of a system, one needs to look beyond the system itself, and into the activities that it will support. For example, the purpose of a banking system is not to be found in the technology used to build it, but in its day-to-day business activities in fulfilling the needs of its customers. Thus, requirements are a set of activities concerned with identifying and communicating the purpose of a system and the contexts in which it will be used. Requirements act as a bridge between the real-world needs of the Client, and the capabilities and opportunities afforded by technologies.

Requirements engineering is the disciplined and systematic approach to elicit, specify, analyse, commit, validate, and manage requirements while considering user, technical, economic, and business-oriented needs and objectives. It spans the entire lifecycle, often involving distributed teams and supply chains. Understanding the requirements and making sure they are complete and stable are two important aspects of the SE processes, as the rest of the activities are derived from these requirements.

Requirements engineering offers three general principles that are useful in dealing with the complex problems:

- Abstraction: i.e. ignoring the details so that one can see the big picture. The system logical architecture is an abstraction of the system functionality;
- Decomposition: i.e. breaking down a system into parts, so that one can study them independently from each other, and by the different Specialist Engineers. Decomposition in subsea engineering is performed along the line of vendors' specialisation. Such decompositions are never perfect, because of the coupling between the parts, but it offers insights into how things work as well as identifies competent design and manufacturing;
- Projection: i.e. adopting a view or perspective of how the system works, and describing only the aspects that are relevant to that perspective. Unlike decomposition, the perspectives are not intended to be independent in any way (Figure 8).

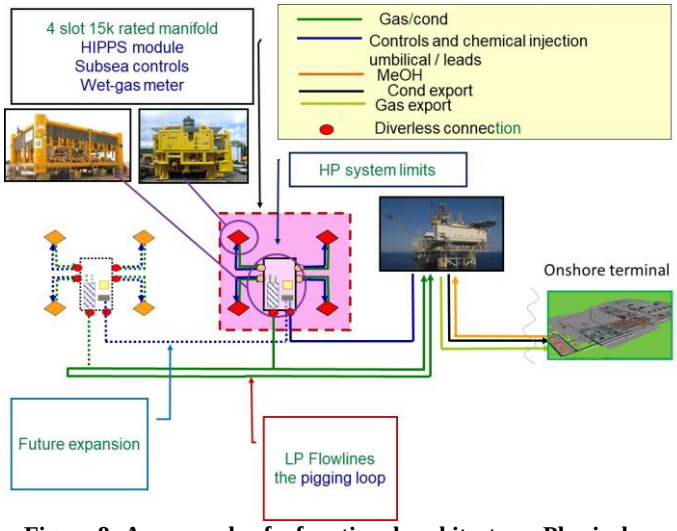

Figure 8: An example of a functional architecture. Physical elements are also sown on the diagram.

Requirement analysts use them to understand what is needed and to identify parts that satisfy the needs of a system. Use of decomposition, abstraction and projection make problems simpler, by mapping existing solutions to problems (or needs). For example, one may look for decompositions in which some of the parts are familiar. In the ideal case, this leads to sub-problems that are sufficiently well known that they have standard solutions. However, one may still have substantial work to do in adapting these known solutions to the new problem context.

A single requirement may have consequences in many parts of a design, program, and data, and may need

many test cases to verify (Federal Aviation Administration, [12]). How a system should interact with its users is also a requirement. There are two types of requirements:

- Functional requirements, which specify what the system should do, i.e., the services the system should provide, and the way it should be provided.
- Non-functional requirements, which specify constraints on how the system should operate and the standards for its operation. Non-functional requirements deal with the characteristics (attributes) of the system that cannot be expressed as functions - such as reliability maintainability, availability of the system, etc.

Non-functional requirements may include:

- Adaptability (expansion);
- Transportability, lift-ability, constructability etc;
- Control-ability such as fast shut down and startup;
- Human-computer interface issues;
- Constraints on the system implementation, etc.

Requirements for a subsystem or a part of the system, do not stem from the technical requirements alone but are only one aspect, of the overall requirement (Figure 9)

A graphical representation of the Requirements Analysis Process as contained in (ISO/IEC 26702 [24] and IEEE 1220-2005 [19]) is shown in Figure 10. The process is quite complex hence requires tailoring to the problem at hand.

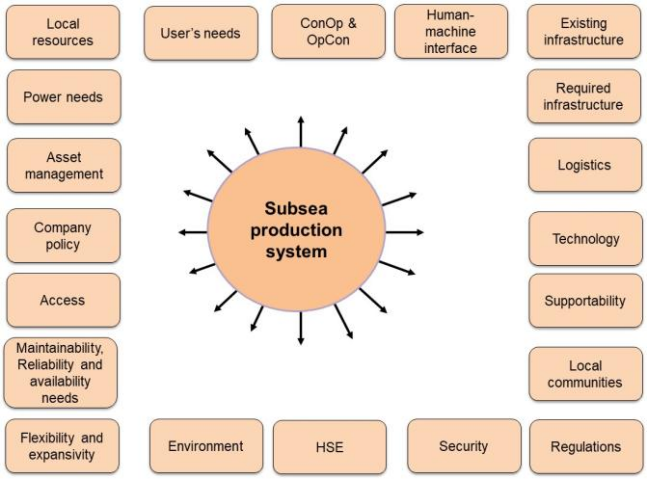

Figure 9: Systems context diagram

6. Requirements Traceability

Requirements traceability will ensure that all higher-level requirements are linked to the lower level requirements, and will be maintained throughout the system development. They are traceable from requirement specifications, through design documents, interface control documents (including operator interface documents) and down to acceptance test procedures. It is important to establish the link between requirements, supporting design data and information within the design documents, as by providing the original context in which a requirement was selected, any future reconsideration of the requirement can determine if the original constraints are still valid Königs, et al [26]).

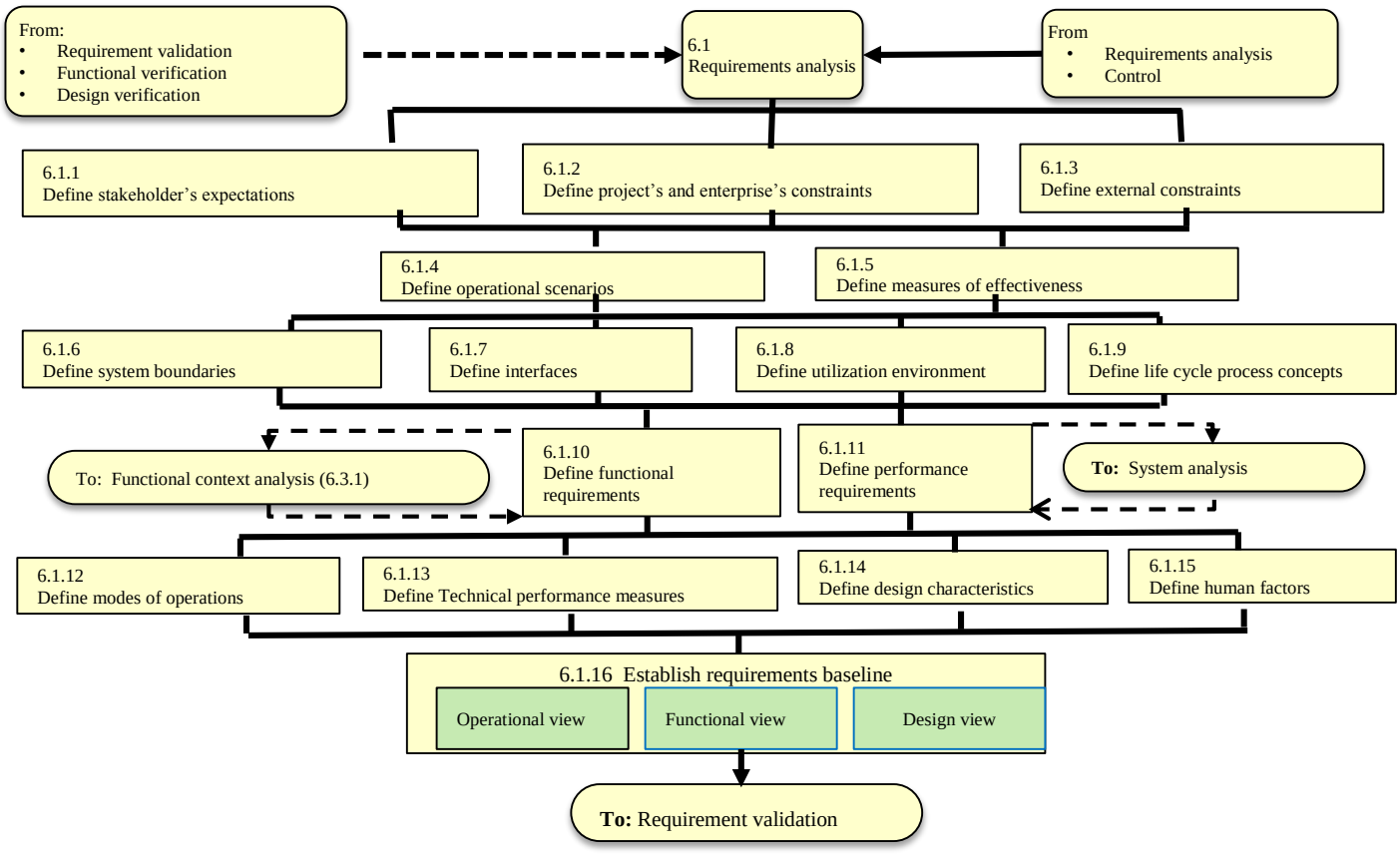

Figure 10: Requirements analysis process of ISO/IEC 26702

Ideally, each requirement from the highest to the lowest level of the project must link to a parent requirement. Requirements without parents will either represent a nice to have or a missing requirement at the higher level. If it is the former, the existence of the requirement must be carefully considered again. In the event of the latter, the requirement needs to be rolled back up to ensure completeness of the requirements at the higher level. A simple trace matrix can be used to simplify and provide a clearer arrangement of the comparison between the user requirements and the technical specifications.

The traceability characteristic means consistent referencing between user requirements, specifications and test cases. This makes it possible to trace cross-references between the specified elements (traceability). To this end, the Client's requirements should be identified with a unique designation, such that referencing is possible.

For each Client Requirement (CR), there must be at least one technical requirement. For each technical requirement (technical specification) there must be at least one specification. The project manager can use the trace matrix in the design qualification to show clearly that all user requirements have been considered. In addition, it can be used to check the completeness of the technical specifications and that the technical implementation corresponds to the requirements. Finally, the trace matrix can be used in the test plan compilation to prove that all user requirements have been tested.

7. Reliability Assessment

Figure 11 shows a subsea project lifecycle. Every Client may have its own lifecycle model, but, they are like what is shown at the top of Figure 11.

A few concepts are developed during the Select Phase and the Conceptual Design. Conceptual Design is an abstract view of the system that shows the only function of all components that make up the system, as well as their inter-relationships. Such diagrams are known as the Functional or the Logical Architecture. One of all the possible Logical Architectures is then selected to be taken forward for the Detail Design Phase. Such choice is based on several criteria, including the lifecycle costs, hence reliability is a major contributor. Modern equipment packages are quite reliable. However, how they are arranged and bundled together will affect the system reliability, as it can affect the Mean Time to Repair (MTTR). Thus, a choice of the architecture based on reliability at the architectural level is the most sensible one.

The Logical Architecture can be improved by performing Reliability and Availability and Maintainability (RAM) analyses, such are MTBF, MTTR and the Reliability Block Diagram (RBD), etc. These methods help to choose the most promising architecture. Generic data (e.g. OREDA [29]) is used to determine the level of availability and how the target availability can be achieved. In the later phase, the generic data is supplemented with the vendor data, and possibly Client database of failures. The Failure Modes, Effects, and Criticality Analysis (FMECA) is

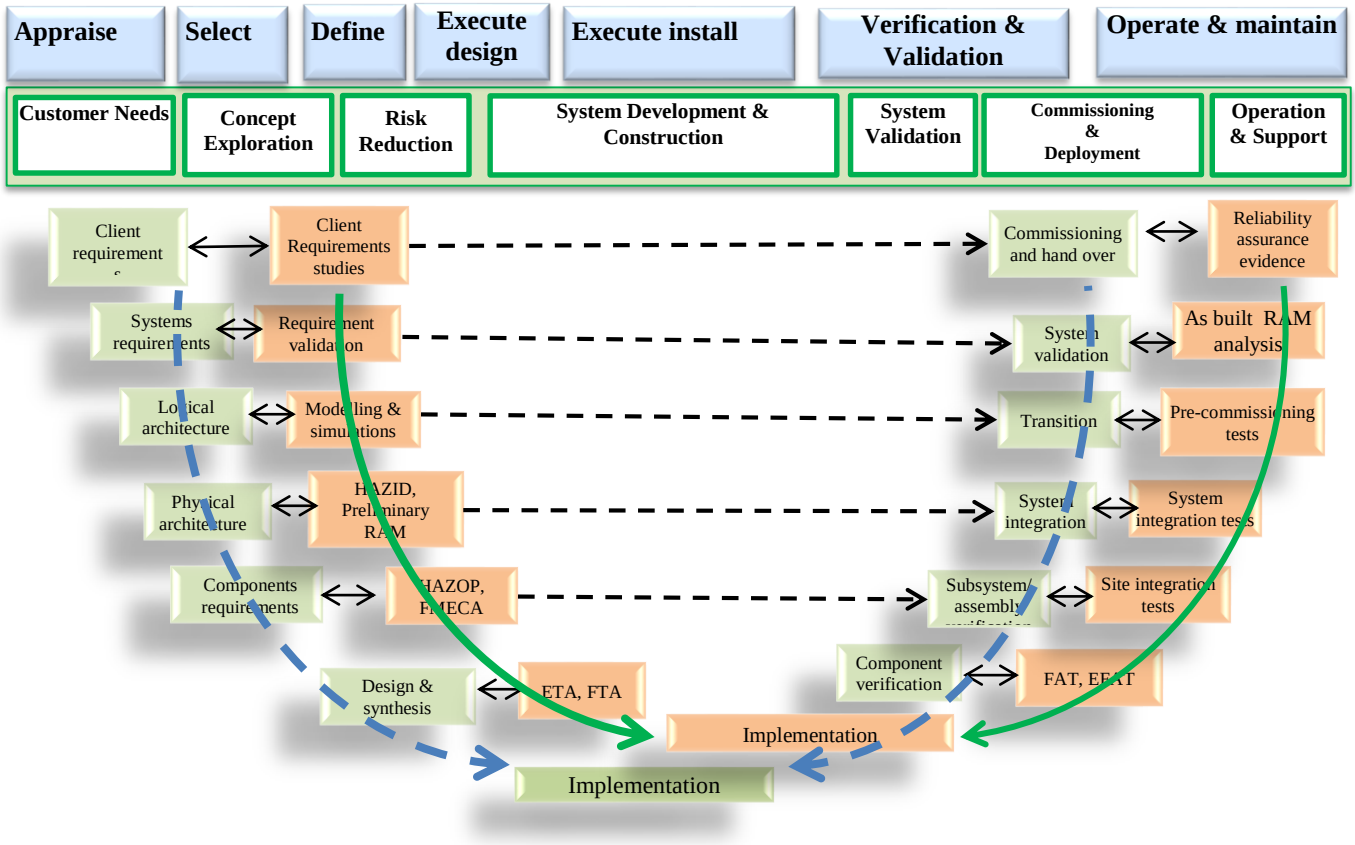

Figure 11: A life cycle model superimposed on the V-model

criticality, rank and suggest corrective and mitigative commonly used to capture all conceivable failure modes and their effects. Usually, FMECA is carried out in the Define Phase and revisited in the Execution Phase (detailed design) of a system, when the physical architecture of the system has taken shape. The objective of an FMECA is to reveal weaknesses and potential failures at an early stage, and based on their modifications to the design. The level of detail and the focus of analysis depends on when the FMECA is carried out. RAM analysis of a system at the early stage of a development can be challenging, especially when system components are not clearly defined. Nonetheless, at early stages of system development, RAM analysis can be used to verify system adherence to target availability requirements. One important step prior to performing a RAM analysis is the need to create a Systems Description Document, which identifies the functions of all the sub-entities of the system and highlights the interfaces between them. In addition, this document also captures the anticipated performance metrics of the system's entities, which are critical inputs for RAM analysis at the conceptual stage of development.

A core activity of reliability assurance is identifying all ways in which the system can fail to perform. This is the case when one or more required functions are disabled (e.g. exceeding the acceptable limits). When this happens, it is called a failure; the resulting state is termed a fault. A fault can be termed as a failure mode. Each function may have several failure modes, and each failure mode may have several different causes, mechanisms and effects (Rausand and Høyland [32]) The failure mode of a component will act as a failure cause of the subsystem, whose resulting failure mode then causes failure of the next level and so on.

In the Define Phase, when no or very few hardware solutions are known, a functional FMECA is done by identifying potential failures for each function according to the hierarchy established in the function tree. In the physical design phase, an FMECA for interfaces is used to verify compliance with the requirements across the interfaces between components and subsystems. In the Define Phase, by selecting vendors, the logical architecture is gradually converted into the physical architecture of the system. At this phase, the specification for hardware and even the candidate vendors are identified and possibly invited to tender. Towards the end of this phase, vendors are selected, and contracts are awarded. The Define Phase is the best time to start reliability analysis of packages.

When hardware and software solutions are decided for the various functions in the Detailed Design (execution) Phase, a System Breakdown Structure showing the hierarchy of components and subsystems is constructed, this is like the Function Trees as shown in Figure 12. With the breakdown structure as input, a detailed FMECA identifies system failures by starting with the failure modes at the lowest level and then proceeding upwards in the hierarchy until the system level is reached.

The FMECA is done by answering a set of questions (Rausand and Høyland [32]):

1. How can each part conceivably fail?
2. What mechanisms might produce these modes of failure?
3. What could the effects be if the failures did occur?
4. Is the failure in the safe or unsafe direction?
5. How is the failure detected?
6. What provisions are provided in the design to compensate for the failure?

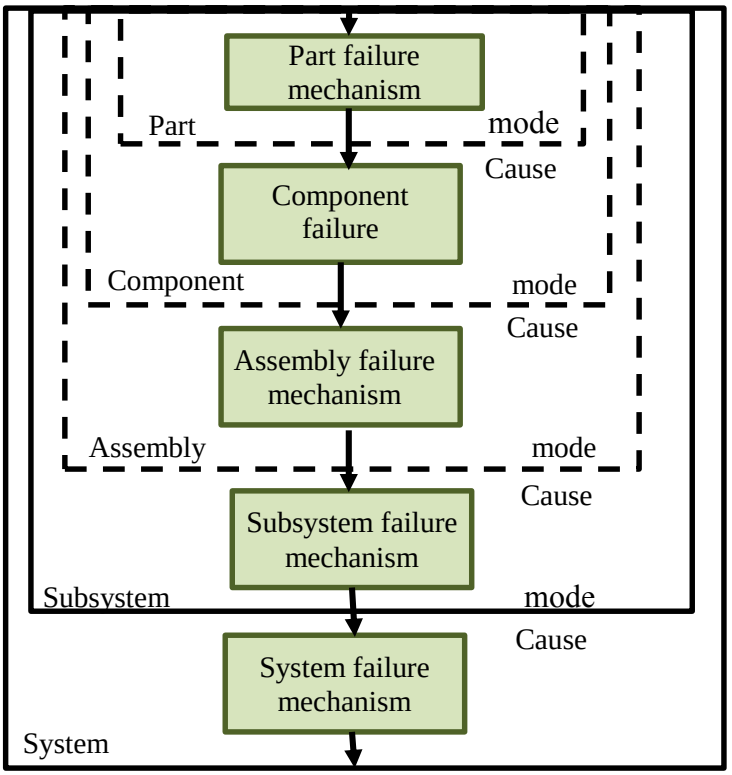

Figure 12: Failure process flow (adapted from IEEE [19])

Another metric used is Technology Readiness Level (TRL) analysis. This is used to track the progress of the system towards the Operational Phase as the system matures (Yasseri [37] and API 17N [3]). TRL (Figure 14) is not an indication of the quality of technology implementation in the design. The TRL analysis, as it stands today, allows any equipment that has been used before to enter the system at TRL 4 or perhaps arguably at TRL 5 (Yasseri [39]). The argument is that a new field is not the same as the existing one, which is true. The consequence of this ranking is everything must be qualified for the environment. This attitude can be explained by considering that in reliability analysis of component/part failure data, the databases used are averaged and generic. Thus, testing only can remove some of the uncertainties.

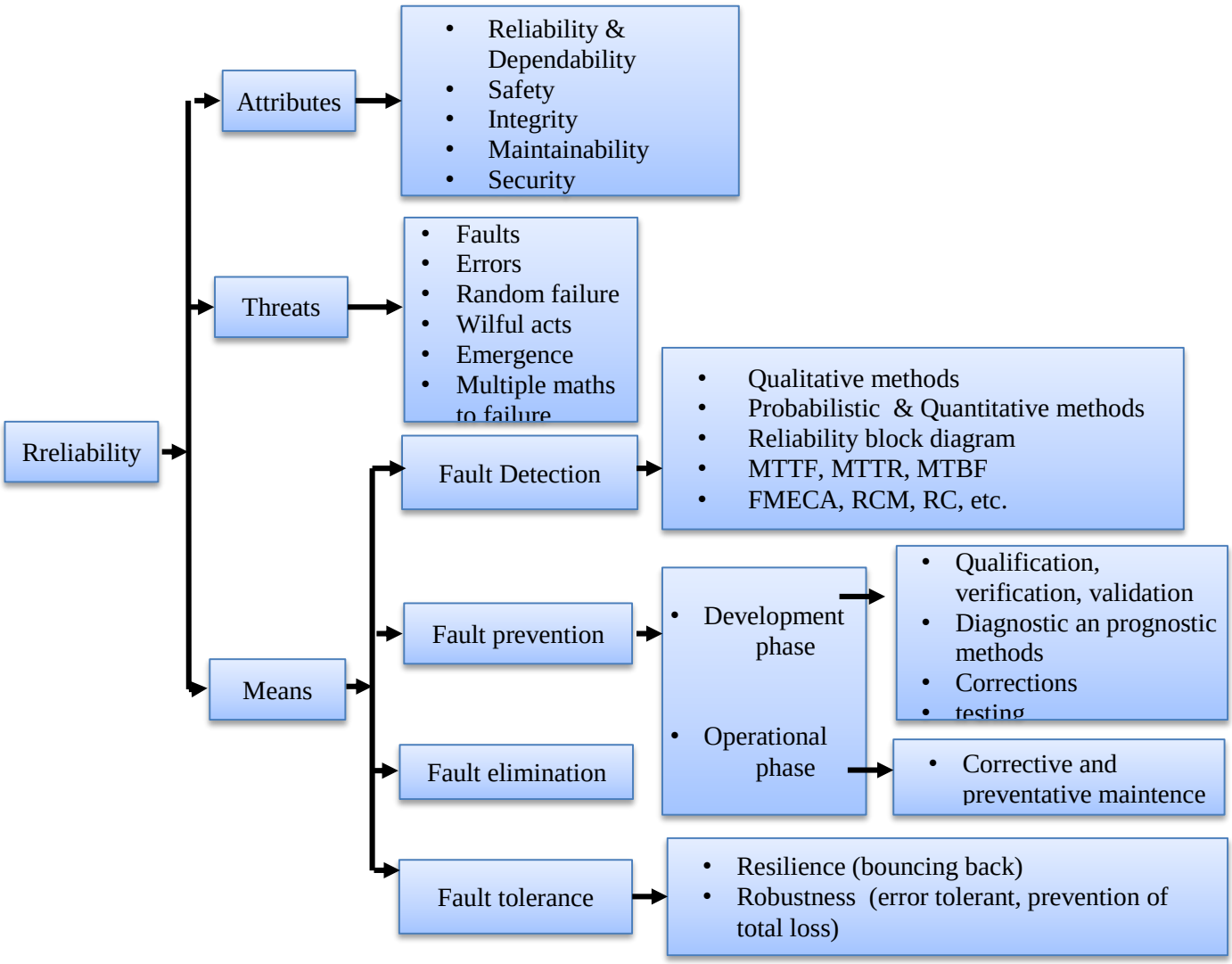

Figure 13: Components of reliability analysis.

Phase	TRL	Development stage completed	Uncertainty reduction
System validation	7	**Field proven** Production system field proven	Maintain qualification of aging system
	6	**System installed** Production system Installed and tested	Commissioning tests
Technology validation	5	**System tested** Production system interface tested	Validation testing , RAM for as the built system
	4	**Environment tested** Preproduction system environment tested	Verification testing
	3	**Prototype tested** System function, performance, and reliability tested	RAM analysis using vendor data
Concept validation	2	**Validated concept** Experimental proof of concept using physical model tests	HAZOP, FMECA, Fault Tree Analysis (FTA), Event Tree Analysis (ETA).
	1	**Demonstrated concept** Proof of concept as desk study or R&D experimentation	What if analysis, Scenario building , Architectural level reliability, availability and maintainability (RAM) analysis using generic data
	0	**Unproven concept** Basic research and development (R&D) in papers	HAZID, Change analysis

Figure 14: API TRL level and reliability assurance activities

RAM analysis provides a way to verify and validate the current system at each TRL level against established operational requirements of the customer. Because simulations represent the ideal future state of the system, it must be understood that the complexities of manufacturing and subsystem integration reduce the availability of the system when deployed. Therefore, to accommodate for the impact of manufacturing on system availability, RAM analysis is used to improve system design beyond the operational availability requirement of the Client, while ensuring that manufacturing, transportation and installation limitations are addressed during the early stages of system development.

The critical part of a technology is a part (or element) which is new, novel, and the system being developed or acquired depends on it to meet its performance requirements within defined cost and schedule. Given that a TRL determination is, in most cases, based on demonstrated performance, the critical technology must be defined at a level that is testable as well. Some authors also state that technologies may be critical from a manufacturing process or material, measurement, or infrastructure perspective, including whether an organization has a workforce with the necessary skills, knowledge, and experience. For example, some organizations will not consider a technology critical if it is having been determined to be mature, has already been used in the field, or does not currently pose a risk to the development. However, when these technology elements are being reapplied to a different program or operational environment, particularly when being used in a novel way, then the definition of criticality applies to them.

All critical technologies must be identified to achieve a comprehensive evaluation of technological risk. While the process to collect evidence for identifying critical technologies can be straightforward, the determination of what constitutes a critical technology is highly subjective, requiring knowledge, experience, and due professional care. Judgements are needed to decide what technology (e.g., hardware, software) is critical, what makes a technology critical, and at what level (e.g., component, subsystem, assembly and system) it is appropriate to test, demonstrate, and validate key functions of that technology or the system.

Although reliability and safety are different issues, tools used in risk reduction are also used to identify the reliability enhancement. HAZOP and HAZID were originally developed for analysing safety; however, they can also be applied to reliability analysis. HAZOP and HAZID studies are systematic methods for examining complex facilities or processes to find actual, or potentially, hazardous procedures and operations so that they may be eliminated or mitigated.

8. Verification, Validation and Qualification

Components are tested at the factory and delivered ready for integration to produce higher-level assemblies or subsystems. These assemblies are also individually verified before being integrated with others to produce yet larger assemblies (for ease of installation) until the complete system has been integrated and verified. The system is installed in the operational environment and transferred from the project development team to the Client team. The transfer also includes supporting equipment, sparing policy, documentation, operator training, and other enabling products that support on-going system operation and maintenance. Acceptance tests are conducted to confirm that the system performs as the Client required in the operational environment. A transition period and warranty see the transition to a full system operation. The above processes are known as “Verification” and “Validation”, which is primarily performed through testing at various stages.

Verification and validation (V&V) are the methods that are used for confirming that a product, service, or system meets its respective specifications and is Fit-For-Service in general terms, verification is a *quality control* process that is used to evaluate whether a product, service, or system complies with regulations, specifications or conditions imposed at the start of the Development Phase (Babuska and Oden [5]). Validation, on the other hand, is a *quality assurance* process of establishing evidence that provides a high degree of assurance that a product, service, or system fulfils the Client’s requirements (Plant and Gamble, [31]). Verification and validation have been defined in various ways that do not necessarily comply with standard definitions. For instance, journal articles and textbooks use the terms ‘‘verification’’ and ‘‘validation’’ interchangeably (e.g. Jagdev et al [14], or Dzida, Freitag [10]), or in some cases there is reference to ‘‘Verification, Validation, and Testing (VV&T)’’ as if it were a single concept (Engel [11]) with no discernible distinction among the three terms (Allen et al [1]). The definitions which are given by ISO 9000 [21] originate from the general field of quality and focus on the provision of ‘‘objective evidence’’ that specified requirements have been fulfilled. The verification process according to ISO is broadly defined, and validation is focused on demonstrating an intended use or application of a system.

A possible structure for V&V program is shown in Figure 15, which starts with reliability analyses and ends in verification and validation by testing, numerical analyses and simulation; or prototyping. The agreed Client’s needs are used to define the requirements, which must be validated to assure if they are achievable, relevant and complete.

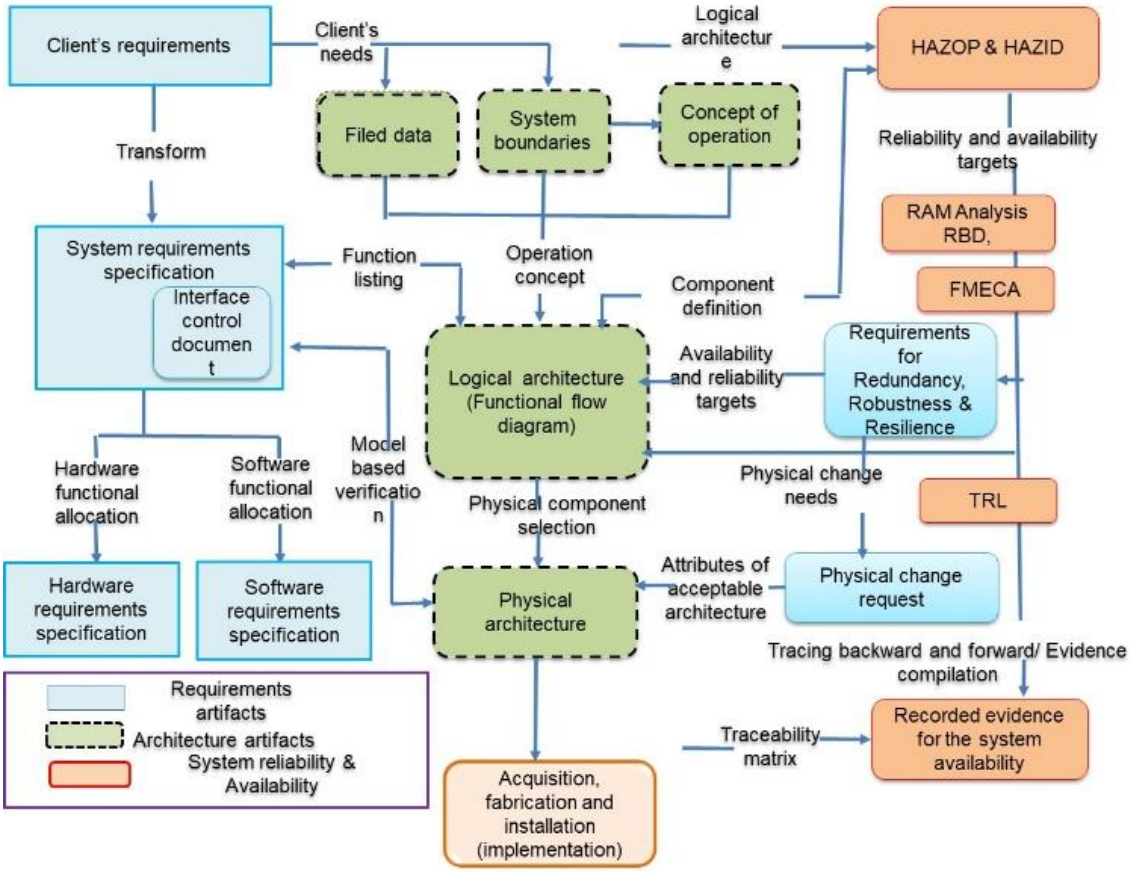

Figure 15: A possible verification and validation flow chart

Tools are qualified whereas processes that use the tools are validated. In this definition qualification is a subset of validation. Fasteners (nuts & bolts) and welding are used to join parts of a system; thus, they are just tools to connect pieces together, but one must also answer if they are Fit-For-Service. In this case:

- One should qualify nuts & bolts or welding material and procedures as a tool for building a system. Perform basic verifications to ensure they are Fit-For-Service;
- One should validate nuts & bolts or welding in assembled equipment for their ability to reliably enable an equipment to deliver the functionality expected of them, presenting evidence from the fasteners qualification tests...

Fasteners are used as an example of a building block. The entire equipment may also be considered as a building block. Such equipment is then qualified using appropriate tests and/or analysis, but a system that uses this equipment needs validation. Thus, qualification tends to be smaller in scope than validation and less dynamic (i.e. qualified for a purpose at a point in time). Thus, according to this definition, qualification is a subset of much greater validation initiative.

Another term often used by some industries is certification. Sometimes certification is used to mean that the performance of the finished product is witnessed by a third party during a specific test, and that party has awarded a certificate of performance; generally, in compliance with a standard. This usage of the term generally refers to mass-produced items, or items produced based on a specification, when required. The current certification practice is "standards-based", which requires that the prescribed certification process of a standard is followed, depending on the application. For example, IEC 61508[15] is used in industrial applications, ISO 26262 [22] is for the automotive area, whereas DO-178B/C [9] refers to software for airborne systems.

In the pharmaceutical industry, *Validation* is used to mean a systematic approach to collecting and analysing sufficient data to give reasonable assurance and documented evidence that a process or an analytical method will, when operated within specified parameters, produce consistent results (mostly drugs) within predetermined specifications (WHO [36]). When this approach is related to a machine or a piece of equipment, rather than the entire system, then it is referred to as *Qualification*. Qualification is part of, but not limited to, a validation process, which in turn is divided into Installation Qualification (IQ), Operation Qualification (OQ), and Performance Qualification (PQ). In performing these activities, many documents describing plans and approaches to analysis are generated. These include Validation Master Plan, Qualification Master Plan, Risk Analysis, Validation Protocol, Test Protocol (including specification), Validation Report, and

finally a Summary of Deviations/Issues (Melero et al [27], and Todde et al. [33]).

Both the pharmaceutical and subsea industries use the term *commissioning* to mean a methodical and documented process to ensure that as built facilities, systems, and equipment meet design codes and the Client's requirements. It applies to all aspects of a facility, equipment, and services. The commissioning process verifies that what was specified, has been installed; that it functions properly; and that it was successfully witnessed by the Client's Operations Team. It is the last system testing before hand over. Commissioning is a managed and planned process of bringing a facility or equipment from its installed or constructed state into service. The key activities are similar regardless of whether commissioning is applied to the entire facility or a simple piece of equipment. The pharmaceutical industry makes a distinction between commissioning and qualification, where the former is concerned with good engineering practice, and the latter primarily verifies the facility and systems aspects that can affect product quality. In the subsea industry, the systems do not affect the quality of the product.

Adding to the confusion caused by these terms, with similar and overlapping meanings, different organizations mix these terms and definitions further.

9. Verification and Validation Strategy

The V&V strategy consists of a set of actions, each one of which is a kind of trial, test or inspection. There may be several actions defined against each requirement.

Each action should consider the following aspects:

• The kind of action that would be appropriate for the requirement;

• The stage at which each action could take place – the earlier the better;

• Any special equipment that would be needed for the action;

• What would constitute a successful outcome.

Qualification and V & V are sometimes used to mean the same thing in the literature, for example, IEC 60300-3-15 (2009) consider the qualification process to embrace both verification and validation. In his paper qualification and verification are used interchangeably.

Figure 11 shows the V&V strategy along with a time-line above the V-model. The early V&V process relates to the left-hand side of the V-model and later ones to the test stages on the right-hand side. A single requirement will typically give rise to a multitude of verification activities at various stages of the development. Where a requirement is satisfied through useful emergent properties, qualification of components alone is insufficient; tests must be carried out at the level where emergent properties manifest themselves.

The V&V actions should be commensurate with the level of requirements in the hierarchy. For example, Client requirements give rise to commissioning trials, whereas system requirements give rise to system tests, that is, prior to hand over to the Client. It is not necessary to define system tests against Client requirements since systems requirements are derived from the Client's requirement.

This paper sees the test as a tool (while V&V are Processes) to provide evidence alongside other tools such as simulation and analyses using suitable models, codes compliance checks, inspection and reviews. These tools must be qualified to ensure they deliver what is demanded of them.

Purely test-based V&V or purely analytical-based V&V can lead to some faults remaining undetected. A balanced use of both has the greatest chance of reducing the cost and enhancing the confidence. From a V&V perspective, the assurance evidence is collected throughout the development lifecycle in the form of formal analysis of the architecture and design. Testing is used to fill the gaps as analytical models cannot detect fabrication errors, or visual inspections cannot be used to accept defects.

Typical steps in the verification and validation process are as follows:

Step 1. Identify Test Needs. Requirements and specifications are used to determine what tests must be carried out. This step also serves to establish how the requirements will be validated. For manufacturers of electro-mechanical products, given their multiple functional domains, this step will serve to identify testing required for mechanical, electrical, and embedded software, as well as for the combined system.

Step 2. Secure Test Facilities and Resources. This entails securing the facilities for building physical prototypes, and then executing tests and/or assigning resources to develop models and run simulations

Step 3. Prepare Test Cases and Test Configuration. Design requirements are translated into a set of test cases with procedures and constraints that can be digitally and/or physically measured. Additionally, new test configurations (which may be mechanical, electrical, and/or software-based) are developed considering the current design (e.g. modifications to geometry, materials, and substituted components). Then, the fixtures and rigs are designed to support testing.

*Step 4. Setup and Execute Test***.** This step calls for the setup and execution of the digital simulation models or the physical tests across all functional domains.

Step 5. Document and Deliver Results. Lastly, results of the physical and/or digital tests are documented in reports, demonstrating that requirements and specifications have been met. The correlation between

simulation and physical tests is documented. Results are then delivered to the submitter to identify passed/failed requirements and recommendations for failures that were encountered.

10. Evidence Gathering

Two sub-processes are used to derive the V&V strategy, i.e. acceptance criteria and quality strategy.

The answer to the question 'what will convince the Client that all requirements have been satisfied?', can often lead to a clearer and more focused formulation of requirements. This question can be answered in two ways:

• The Client may define an operational situation in which the requirement can be demonstrated, and/or,

• The Client may define a numerical value for a level of achievement that must be demonstrated.

The first type of answer feeds directly into the process of creating a set of tests, trials or demonstrations that must be part of the V&V strategy. The second type of answer indicates the 'pass mark' for a trial test or demonstration, i.e. it indicates the acceptance criterion for the requirement. Acceptance criteria define, for each requirement, what would be a successful outcome from the qualification approach adopted.

For one-off systems such as SPS, it is necessary to make sure that all the functionality has been properly provided and that the production personnel are happy that the system can be used easily and quickly on demand. This will require a mixture of tests and trials. First, the capability of the system under test loading must be demonstrated. If this capability is not acceptable, then there is no point in progressing to tests that involve much more investment such as live trials at full capacity.

The Client's needs are used to set the initial requirements and are frequently referred to as part of the validation activity. Initial model validation is done to ensure that the models, analysis and simulations can be used safely to support requirements validation. In addition to performance analysis, modelling and simulation, requirements validation can include risk analysis, such as Fault Tree Analyses and Probabilistic Risk Analyses, to ensure the design will be robust against failures or system upsets (IAEA-TECDOC-1264 [15]).

Flow assurance analyses are performed to study the limits of operation as well as for production planning. This helps with studying the sensitivity of the operational needs to changes in key reservoir parameters. Monte Carlo simulation is another useful tool for assessing the robustness of a system in terms of its overall performance; especially during a system upset.

11. Discussion

The key concepts to establish linkages between requirements and testing for Validation & Verification are shown in Figure 16. At each level of the system decomposition, requirements are flowed-down and suitable test plans are devised for verifying that the system will satisfy requirements. To make sure all requirements are properly implemented, it must be possible to trace each requirement to a component and vice versa. Requirements traceability is the ability to link every requirement to three related items:

- The Client's needs (the starting point) that it fulfils;
- The system elements implemented to satisfy it;
- The test case that verifies it.

The end-to-end traceability links enable us to evaluate exactly what is impacted by the latest requirement change, or an alternative design choice before the change is implemented.

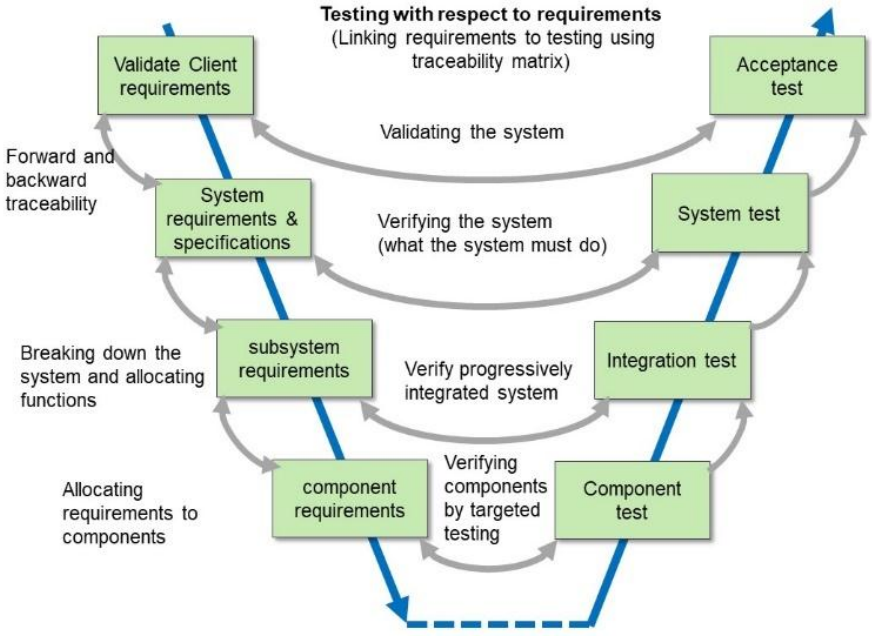

Figure 16: Linking V&V to the Client's requirements

FAT (Factory Acceptance Tests) and EFAT (Extended Factory Acceptance Tests) performed on components are documented to use in a traceability matrix. This ties the tests back to the specific requirements they verify and ensures that no requirement is left untested. Hardware and software components, which are already verified by tests, are then integrated into modules or subsystems and tested. The goal at this stage of testing is to ensure that all the interfaces between components and assemblies are satisfactory and that all subsystem requirements and constraints have been considered. An integration plan is devised that defines the order in which lower-level components and subassemblies are integrated. At each integration step, the functionality of the sub-assemblies against the appropriate set of requirements is verified using the Subsystem Verification Plan devised during the Design Phase. Tests performed to verify requirements at the component level are important since many requirements are cascaded through multiple levels of system decomposition.

The goal of system acceptance testing is to validate that the system fulfils its intended purpose. During the Conceptual Phase, key Client needs, overall system capabilities, usage scenarios (CONOPS and use cases) and performance measures for system validations are identified. A *System Validation Plan* is devised and monitored using change control, which ensures that the verification plan, or test procedure, is not wrong or out-dated. When verification testing indicates a problem, the requirements and design must be reviewed to see what, if any, adjustments are necessary (Bahill and Henderson [6]).

Pieces developed independently don't always work when integrated together, which is arguably the largest single factor that causes schedule and cost overruns. Thus, the Systems Engineers have devised the following policy to minimize this risk:

- Verify interfaces and interactions between key subsystems and components early by use of models and simulations;
- Integrate parts progressively.

12. Concluding Remark

Qualification is used, in this paper, to mean 'a state of readiness to operate', which must be maintained as the equipment ages. The term qualification is also used to mean that materials, design, fabrication and performance under intended use, are verified by a combination of analyses, simulations and testing, throughout the project life. Traditional *quality control* assures that the product will work after assembly and as designed. Whereas *reliability* provides a probabilistic assurance that an item will perform its intended function for a defined period without failure under specified conditions. In other words, reliability looks at *how long* the product will work as designed, which is a very different objective than that of traditional quality control. Therefore, different tools and models apply to reliability, do not necessarily apply to quality and vice versa.

The focus is on the continued function and resilience of critical assets to prevent interruption of functions. Reliability assurance is a common integrative framework, not a single policy, to design in robustness and resilience and to reduce breakdown due to mechanical failure, accidental event and willful actions. Reliability assurance also relies on existing protection and mitigative policies, including material selection, corrosion protection, accident prevention external hazards, geotechnical hazards etc. The effectiveness of reliability assurance should be measured in relation to availability and continued operation. The present framework merges with the wider issue of risk management framework and the strategic objective of the owner.

The verification strategy is defined as combining efficiently the different verification stages, verification levels and verification methods, to reach the following objectives:

• Satisfy the Client's requirements;
• Maintain cost targets;
• Respect schedule constraints.

The initial step of the verification process is the identification of the requirements to be verified. The general requirements are analysed to originate system and lower level specifications containing a consistent tree of performance addressing; design, interface, environmental, operational and support requirements, which form the basis of the verification activities at the different levels. To facilitate the verification implementation in terms of planning, execution, control and reporting, the requirement generation and allocation activity will ensure specific requirement characteristics; each requirement shall be:

• *Traceable* with respect to one or higher-level requirement;
• *Unique* and associated with a proper identifier (document and paragraph number);
• *Single* and not containing more than one requirement;
• *Verifiable* with one or more approved verification method;
• *Unambiguous* and containing a precise statement;
• *Properly referenced* to other requirements, with the applicable document and paragraph identification.

In addition to performance analysis, modelling and simulation, validation include reliability analysis to ensure that the design will be robust for all specified operating and environmental conditions, which should also consider all possible deviations from the normal operating condition.

One of the fundamental principles of the subsea industry is that quality must be designed into equipment and processes from the beginning. Facilities and systems must support the quality

requirements of their associated processes to be deemed "Fit-For-Service". Reliability analysis methods help to identify critical aspects of the design to focus on, thus moderating the amount of testing. The term 'critical aspect' is used to mean mitigation control implemented by design, not by procedural controls. Critical aspects can be identified during a risk assessment. Industry uses a plethora of methods for risk identification. HAZOP, HAZID and FMECA are three examples of hazard assessment methods which perform well in the identification of risks.

It was also emphasised the importance of tracing the requirements to their solutions (design), the Requirements Traceability Matrix (RTM) documents show how the analysis of requirements translates into the project-specific design, from which technical specifications can be developed and used to design testing and acceptance criteria.

The subsea industry never intentionally creates requirements and designs that result in operation at the "limit". While a system may be designed to meet performance specifications within a generous set of tolerances, it should be rare to fail rapidly in the event of relatively minor excursions from normal operation. The concept of graceful degradation, without failure, is the key to successfully implementing subsea systems in deeper environments at a reasonable cost and within a reasonable timescale. A properly executed validation program will enable slow degradation by using performance sensitivity analyses and design risk analyses, thus providing the project insight to guide risk versus cost (mitigating action) trades.

13. REFERENCES

1. Allen N.A., Shaffer C.A., Watson L.T. (2005). "Building Modelling Tools That Support Verification Validation, and Testing for the Domain Expert," Proceedings of the 2005 Winter Simulation Conference, Orlando, FL, pp 419–426.
2. ABS, (2017). Guidance notes on Qualifying New Technologies, American Bureau of Shipping, PP 45
3. API 17N, (2014). *Recommended Practise for Subsea Production System Reliability, Technical Risk & Integrity Management*
4. API 17Q, (2010). *Subsea equipment qualification – standardized process for documentation*
5. Babuska I, and Oden JT (2004). "Verification and Validation," Computational Engineering and Science: Basic Concepts. Computer Methods in Applied Mechanics and Engineering 193(36–38):4057–4066.
6. Bahill, A.T., and Henderson, S.J. (2005) Requirements Development, Verification, and Validation Exhibited in Famous Failures Systems Engineering, Vol. 8, No. 1.
7. Bureau Veritas, (2010). *Risk bases Qualification of New Technology Methodological Guidance, Guidance Note NI 5252 R00E*, pp 20.
8. DNV-RP-A203 (2011). *Qualification of new technology*. Det Norske Veritas, Høvik, Norway.
9. DO-178C, (2011), Software Considerations in Airborne Systems and Equipment Certification, FAA
10. Dzida W, Freitag R (1998) Making Use of Scenarios for Validating Analysis and Design. IEEE Transactions on Software Engineering 24(12):1182–1196.
11. Engel, A. (2010). Verification, Validation, and Testing of Engineered Systems. Wiley.
12. Federal Aviation Administration. *Requirements Engineering Management Handbook DOT/FAA/AR-08/32*, 2008, last accessed 23/12/2017, available on. http://www.faa.gov/aircraft/air_cert/design_approvals/air_software/media/AR-08-32.pdf
13. Feiler, P.H., Goodenough, J.B, Gurfinkel, A., Weinstock, Ch. B., and Wrage, L. (2012), SPECIAL REPORT CMU/SEI-2012-SR-013, Reliability Validation and Improvement Framework Carnegie Mellon University
14. Jagdev H.S, Browne, J, Jordan, P. (1995), Verification and Validation Issues in Manufacturing Models. Computers in Industry 25(3):331–353
15. IAEA-TECDOC-1264, (2001), Reliability assurance programme guidebook for advanced light water reactors.
16. Hother, J.A., and Brian J. Hebert, B.J., (2005), Risk Minimization using Failure Mode Analysis in the Qualification of New Technology - Recent Project, SPE-96335-MS, SPE Annual Technical Conference and Exhibition, 9-12 October, Dallas, Texas Experience
17. Hull, E., Jackson, K., and Dick, J. (2002). *Requirements Engineering*, Springer-Verlag, London.
18. IEC 61508, SC 65A, (2010), Functional safety of electrical/electronic/programmable electronic safety-related systems in seven parts.
19. IEEE 1220-2005, 2005, reaffirmed in 2011, Standard for Application and Management of the Systems Engineering Process
20. INCOSE 2015. Systems Engineering Handbook – A Guide for System Life Cycle Processes and Activities, version 4.0. Hoboken, NJ, USA: John Wiley and Sons, Inc., ISBN: 978-1-118-99940-0.
21. ISO 9000 (2005) *Quality Management Systems: Fundamentals and Vocabulary*, ISO organisation
22. ISO 26262 (2014), Functional Safety Standard.
23. ISO/IEC 15288, 2008, Systems Engineering-System Life Cycle Processes
24. ISO/IEC 26702 IEEE Std 1220-2005 First edition 2007-07-15 - ISO/IEC Standard for Systems Engineering - Application and Management of the Systems Engineering Process
25. Lloyds Register, (2017). *Guidance Notes for Technology Qualification*, Published by Lloyd's Register group ltd, London, pp43.
26. Königs, S.F., Beier, G., Figge, A., and Stark, R. (2012). "Traceability in Systems Engineering –

Review of industrial practices, state-of-the-art technologies and new research solutions," Elsevier Advanced Engineering Informatics, 26(4), pp 924-940.
27. Melero, L.T.U.H, da S. Silva K.S., Zanette, C., de Araújo E.B., and Mengatti, J., (2011), Calibration and Qualification of equipment in the Pharmaceutical industry, International Nuclear Atlantic Conference, INAC 2011 Belo Horizonte, MG, Brazil, pp 8, https://www.ipen.br/biblioteca/2011/inac/17018
28. NASA, (2007). *Systems Engineering Handbook*. NASA Technical Report NASA/SP-2007-6105 Rev1, ISBN 978-0-16-079747-7, Washington, DC, USA.
29. OREDA (2009). Offshore Reliability Data. Det Norske Veritas, Høvik, Norway, 5th edition.
30. Pecht, M. (1993). "Design for qualification," Annual Reliability and Maintainability Symposium
31. Plant R, Gamble R (2003) Methodologies for the Development of Knowledge-based Systems. Knowledge Engineering Review 18(1):47–81.
32. Rausand, M. and Høyland, A. (2004). *System Reliability Theory: Models, Statistical Methods, and Applications*, PP 664.
33. Todde,S., Peitl, P.K., Elsinga, P., Koziorowski, J., Ferrari, V., Ocak, E.M., O. Hjelstuen, O., Patt,M., Mindt,T.L. and Behe, M., (2017) Guidance on validation and qualification of processes and operations involving radiopharmaceuticals, EJNMMI Radiopharmacy and Chemistry, 2:8 https://ejnmmipharmchem.springeropen.com/track/pdf/10.1186/s41181-017-0025-9?site=ejnmmipharmchem.springeropen.com
34. Viola, N., Corpino, S., Fioriti, M. and Stesina, F., (2012). Functional Analysis in Systems Engineering: Methodology and Applications, Systems Engineering - Practice and Theory, Boris Cogan (Ed.), ISBN: 978-953-51-0322-6, In Tech, last accessed 23/12/2017, Available from http://www.intechopen.com/books/systemsengineering-practice-and-theory/functional-analysis-in-systems-engineering-methodology-and-application
35. Woody, C., Ellison, R. and Nichols, W., (2014), Quality and Reliability Measures, CMU/SEI-2014-TN-026, Carnegie Mellon University, http://www.sei.cmu.edu
36. WHO- (2016) World Health Organization, Annex 4, "Supplementary guidelines on good manufacturing practice: validation". HTTP://www.who.int/medicines/areas/quality_safety/quality_assurance/validation-without_appendices_2016_05_17. pdf?ua=1. Accessed 23/12/ 2017.
37. Yasseri S. (2013). "Subsea system readiness level assessment" Int. Journal of Underwater Technology 31: 77–92
38. Yasseri S., (2014). "Application of system engineering to subsea development," Int. Journal of Underwater Technology,32:93–109
39. Yasseri S., 2014, "A measure of subsea readiness level development," Int. Journal of Underwater Technology 32:93–109
40. Yasseri S. (2015). "Evidence-based subsea engineering," Int. Journal of Underwater Technology Vol. 32, No. 2, pp. 93–109,
41. Yasseri S. Bahai, H and Yasseri, R., (2018). "A Systems Engineering Framework for Delivering Reliable Subsea Equipment, 2018-TPC-035, ISOPE 2018, Japan. Accepted for publication
42. Youngblood, S. M., and Pace, D. K., (1995), "An Overview of Model and Simulation Verification, Validation, and Accreditation," *Johns Hopkins APL Tech. Dig.* **16**(2), 197–206.

Abbreviations

Abbreviation	Description
CAPEX	Capital expenditure
CAD	Computer-Aided Design
CFD	Computational Fluid Dynamics
ConOps	Concept of Operations
CR	Client Requirement
EFAT	Extended Factory Acceptance Test
FE	Finite Element
FAT	Factory Acceptance Test
FFP	Fit-For-Purpose
FFS	FitFor-Service
FMECA	Failure Mode Effect Critically Analysis
HAZID	Hazard Identification
HAZOP	Hazard of Operation
KP	Key Process
MTTF	Mean Time To Failure
MTTR	Mean Time To Repair
MTBF	Mean Time Between Failures
OPsCon	Operations Concept (OpsCon).
OPEX	Operating expenditure
RAM	Reliability, Availability and Maintainability
RTM	Requirements Traceability Matrix
SAT	Site Acceptance Test
ROV	Remotely Operated Vehicle
SPS	Subsea Production System
TRL	Technology Readiness Level
V&V	Verification & validation
VV&T	Validation, Verification & Testing

INTERNATIONAL JOURNAL OF
COASTAL & OFFSHORE ENGINEERING
IJCOE Vol.3/No. 1/Spring 2018 (21-34)

Available online at: http://ijcoe.org/browse.php?a_code=A-10-180-1&sid=1&slc_lang=en

A Comprehensive Study of an Identical Submarine Subjected to Explosion

Rouhollah Amirabadi[1*], Reza Ghazangian[2]

[1*] *Assistant Professor of Civil Engineering, University of Qom; r.amirabadi@qom.ac.ir*
[2] *PhD of Civil Engineering, University of Qom; gharangian@gmail.com*

ARTICLE INFO

Article History:
Received: 18 Apr. 2018
Accepted: 9 Jun. 2018

Keywords:
Finite Element Method
Doubly asymptotic approximation
Submarine
Explosion

ABSTRACT

Despite the enormous military threats against the country's military facilities, especially the naval industry, correct understanding of the behavior of these structures in efficacy of explosion, analysis and design of this industry has been much importance than ever before. An important class of these threats, is underwater explosion and its effect on various structures, Floating or submerged. In this paper, the researcher first introduces the underwater explosion phenomena and theories that govern the propagation of fluid hydrodynamics, shock waves from the explosion and its interaction with floating and also submerged structures have been investigated. Finally, numerical studies (FEM) of the behavior of a super submarine subject to underwater explosion have been provided by ABAQUS software and some results have been obtained such as: response with different frequencies, the place of radiation boundary in interaction of water and construction, the effect of added mass and hydrodynamic pressure.

1. Introduction

Naval structures have many applications, especially in the oil and gas industries of every nation. The design of these structures has been influenced by various factors such as wind, wave, current, earthquake, and dead and live loads. On the other hand, with the spread of military threats against the country, the analysis and design of these structures under the explosive loads become apparent. One of the crucial issues in the study of water-structure interaction is underwater explosions and their impact on submerged structures, as they are strategically critical in terms of engineering application and passive defense. Since World War II, this subject has been studied and underwater explosions have been used in many industrial projects such as the shaping of metal planes and military operations and recently for the removal of obsolete marine structures such as platforms. The waves caused by underwater explosions have a remarkable impact on submerged structures like submarines, pipelines, oil platforms and facilities etc. Therefore, the detailed analysis of underwater explosions has been considered a necessity in reducing the damage of these structures.

In engineering sciences, it is sometimes essential to dismantle all the devices into single components and parts with understandable behavior and then restore the device based on such components, in order to clearly understand the environmental behavior and its natural processes. Numerical methods are one of these processes, capable of modeling the behavior of complex phenomena by discretization. Moreover, two cases are often posed with regard to the dispersal of waves in any space. In the first case, we deal with waves of small amplitude and then in the second case, these are shockwaves and therefore we deal with the waves of finite amplitude. The waves which are created in the vicinity of the explosions, are of the second type.

In this article, we first express the theories of interaction analysis for water and submerged structures being subject to explosions and then we use ABAQUS software to provide a numerical modeling for a submarine.

2. Research history

Cole is the first scholar to explain the equations regarding underwater explosions in his research [1]. By describing various processes of explosions, he has developed a new way in this field. The complete analysis of the problem of underwater explosion involves solving the equation of structural vibration and the concurrent diffusion of waves from the explosion source through the fluid. The methods used to analyze this phenomenon are either the expansion of series or the use of variable changes. In 1999, Maire collected the reference problems which propose an analytical and precise solution to the water-structure interaction [2]. Since the introduction of all

these instances is beyond the scope of this article, it would sufficient to report a few cases in this regard.
Shock chamber: This model proposes a one-dimensional solution to the problem of shock and wave diffusion due to the interaction of two fluids in a stationary state in the Cartesian-Riemann system.
Rayleigh Model: A one-dimensional solution is proposed in the spherical structure for the dynamic incompressible fluids.
Primakoff Solution: A one-dimensional solution is provided in the spherical structure for the dispersal of shockwaves in the water caused by movable boundaries.
Table 1 summarizes these cases.

Table 1. General issues for continuous flow field

	Analytical\Empirical	Water	Bubbly\ Cavitating Water	Idealized Sediment	In-Suit Sediment	Air	Explosive
Shock Tube	A	●	○	○	○	○	○
Rayleigh-Plesset Solution	A	●	○	○	○	○	○
Primakoff Solution	A	●	○	○	○	○	○
Caviated Water Impact	A	○	●	○	○	○	○
P.alpha Shock Tube	A	○	○	●	○	○	○
Wardlaw/Mair Bubble	A	●	○	○	○	○	○
UNDEX Similitude	E	●	○	○	○	○	○
Spark-Generated Bubbles	E	●	○	○	○	○	○
SRI Spherical Sand Shock	E	○	○	●	○	○	○
Snay Goertner Bubble	E	●	○	○	○	○	○

The black and white circles indicate existence and absence respectively.
In 1984, Felippa and Deruntz developed a finite element method for cavitation based on the works that Newton had done between 1978 and 1981 on the impact of cavitation on the underwater explosion. In this method, the wave field inside the fluid was modeled based on a potential function of scalar displacement. CAFE elements were first used by its originators in CFA computer program. The fluid boundaries were considered based on the method used by Geers in 1978. These boundaries which are called doubly asymptotic approximation are actually a boundary element method that provides accurate answers at the initial and final intervals of the analysis. USA computer program developed by Deruntz in 1989 has been based on this method [3,4]. Then, in 1990, another program called USA/LS_DYNA was developed by Hallquist based on CAFE method in which semi-discrete equations of fluid and structure had been integrated implicitly while the fluid boundaries had been modeled by DAA methods and plane wave approximation[5]. In 2008, the ABAQUS software appeared in the markets based on the same method, but it is distinct, as the fluid field was modeled based on the method of the boundaries of curved wave approximation [6]. When an explosion occurs in the vicinity of a structure, the assumption of the small motions of the fluid cannot be logical anymore and it is possible to use hydrocodes as referred to in [7]. These hydrocodes have been mentioned along with the method applied for the problem analysis. Recently, in 2002, Sprague and Geers enumerated the disadvantages of CAFE model and proposed a new method based on spectral elements[8]. In spectral elements, the three-line functions used in the finite element CAFE model are removed and replaced with Legendre functions. In fact, it can be said that the accuracy of spectral elements has been integrated with the flexibility of finite elements in CAFE. Moreover, they used the idea of separating the fluid environment into the total field and intervention and diffraction field, in order to express the equations related to the fluid [9,10].
More studies were done by Dyaka, Shin and Li on the non-linear transient response of the submerged circular plates subject to explosion loads [11-13]. In their studies, they used the Kirchhoff theory of thin plates and hypothesized that this plate can show non-linear geometrical and material behavior [11-13]. To analyze the problems of water-structure interaction with the help of numerical methods like finite elements, there are various numerical models such as Lagrangian model, free Lagrangian model (FLM), smoothed particle hydrodynamic model (SPH), total Lagrangian model, Eulerian model, coupled Eulerian-Lagrangian model (CEL) and arbitrary Eulerian-Lagrangian model.

2-1. Theories of water-structure interaction analysis

Normally, in dealing with the issues related to underwater explosions, there are two cases that must be encountered: first explosions close to the free surface, second the areas far from the free surface (ocean depths). The importance of this topic has been increased due to a critical phenomenon called cavitation. This phenomenon which has a completely non-linear nature plays a major role in the analysis of the issues concerned with water-structure interaction.

2-2. the fluid field away from the free surface without cavitation

Thus far, advanced computational methods have originated to deal with underwater shockwaves at the depths of oceans where there is no cavitation. In these models, the fluid is assumed as an infinite and

homogenous acoustic field, while the structure and probably the fluid which is close to the structure are modeled by the finite element method, the impact of fluid field through one of the boundary element, or finite element methods which are engaged in the finite element model of the structure as a system.

2-3. Doubly asymptotic approximation (DAA)

One of the effective methods for the fluid field modeling is the doubly asymptotic approximation. It is used in cases where the presence of cavitation is rare and only the diffracted hydrodynamic sound pressure caused by the fluid-structure interaction is important while the total pressure inside the fluid is of no importance. A formulation of this method from the first rank or DAA is expressed in the below equation [14]:

$$M_f \dot{p}(t) + \rho_f c_f A_f p_s(t) = \rho_f c_f M_f \dot{u}_s^f(t) \quad (1)$$

Where M_f is the fluid mass matrix for the surface of the fluid subject to the structure and A_f is matrix diametrical cross-section which changes the knot pressures into knot force. $\dot{u}_s^f(t)$ is the diffraction rate of fluid particles which is perpendicular to the interface of structures and ρ_f is the diffracted term from the total pressure.

The DAA relation is otherwise called the doubly asymptotic approximation as it shows the limited behavior in high frequencies (initial intervals) and low frequencies (final intervals) of the analysis. For high frequency response, the term $\left|\dot{p}_s(t)\right|$ is considerably greater than term $\left|p_s(t)\right|$ in the above equation. Therefore, the second term in equation 1 is omitted which in turn leads to the plane wave approximation in which $p_s(t) = \rho_f c_f u_s^f(t)$ and is accurate for the short sound wavelengths. However, for low frequency responses, term $\left|p_s(t)\right|$ is considerably greater than term $\left|\dot{p}_s(t)\right|$ and equation 1 is $A_f p_s(t) = M_f \dot{u}_s^f(t)$ which indicates the mass added to the structure that is accurate for the long sound wavelength. The equation of compatibility between the interfaces of the fluid and structure is expressed by the below equation [9]:

$$G^T \dot{u}^m = u_i^f + u_s^f \quad (2)$$

Where i and s indicate the speed of the incident wave and the speed of diffracted fluid particles and $\dot{u}^m$ is the vector of structure particles in the interface of the fluid. G^T is the transpose of the matrix on the interface of the structure and fluid. Equation 2 indicates that the speed of the particles inside the fluid and on the surface of the structure is equal on their overlapping surface. Now, by inserting equation 2 into equation 1, the dynamic equation of the fluid behavior with DAA method from the second rank has also been developed by Geers in which higher terms of scattering pressure have been considered. In total, it can be said that DAA is a very effective and useful approximation method for the modeling of the fluid field with the removal of the finite element modeling for the fluid fields with deep structures and its application in the form of a layer of elements on the structure, so that the impact of cavitation can be ignored. In this state, only the term of hydrodynamic pressure caused by the scattered sound waves can be calculated. In figure 1, the schematic DAA model has been illustrated [14].

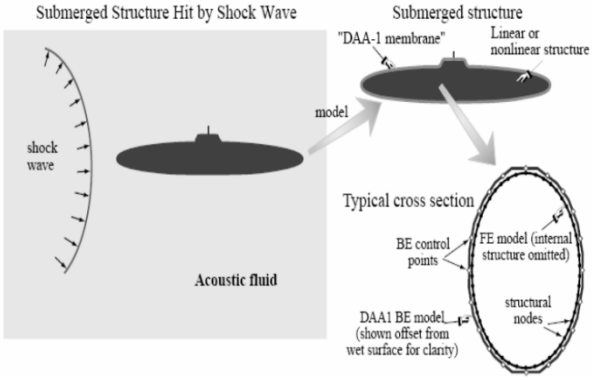

Figure 1. A schematic illustration of the fluid field modeling with DAA boundary element method

2-4. Retarded potential method

This method is indeed an analytical solution for the wave equation (Helmholtz equation). The integrated pressure equation is a function of time, indeed space is discretized by the boundary element method and then the equation has been analyzed with the motion equation of the structure as a system [15].

Suppose a submerged surface is subjected to an incident wave in the water. The fluid field is assumed to be incompressible and non-adhesive. The pressure of the incident wave is expressed as P_{inc} that hits the structure and produces intervention and scattered waves or P_{sca}. Moreover, the responses of the structure also produce a radiation pressure P_{rad} within the fluid field. Therefore, the total pressure consists of three parts as described below [15]:

$$P = P_{inc} + P_{sca} + P_{rad} \quad (3)$$

The boundary terms of the wetted surface of the structure is described as follows equation 4 where n is the normal vector towards the outside from the fluid to the structure, p is fluid density and a_n is the normal velocity of the structure [15]:

$$\frac{\partial P}{\partial \eta} = -\rho a_n \quad (4)$$

In fact, equation 4 shows the active fluid field. The integral of retarded potential is the solution of the linear wave equation exposed to the boundary conditions of the wetted surface of the structure [15]. Then:

$$\nabla^2 P = \frac{1}{c^2}\frac{\partial^2 P}{\partial t^2} \tag{5}$$

The integrated form of equation 5 causes P_{inc} on the wetted surface of the structure subject to the incident pressure wave. This pressure is formulated as follows:

$$R = |x - x'|$$
$$t' = t - \frac{R}{c} \tag{6}$$

Where c indicates the velocity of sound in the water and t' is the delay duration and x is the location of the point where the observations are being performed, and x' is the location of the integrated point.
Equation 6 is the pressure equation in relation to the equation of the structure, the convergence of responses can be achieved by the step-time implicit solutions.

2-5. The field of fluid close to the free surface exposed to cavitation

2-5-1. Acoustic fluid field

The acoustic fluid suggests the behavior of liquid and gas subject to a rapid dispersal such as shockwaves and sound vibrations that spread with the intervals within the range of sound frequencies. The equation of momentum, continuity, and the equation of motion are used to obtain the equations for the expression of acoustic fluid. The classic wave equation for the acoustic fluid in volume V is expressed as below [16].

$$c^2\nabla^2\psi - \ddot{\psi} = 0 \quad in\ V \tag{7}$$

The displacement function ψ is introduced as the quantity of the dependent variable and is defined for the discretization of finite elements as:

$$\psi(x,t) = N(x)\,\psi(t) \tag{8}$$

Where $N(x)$ is the function of the form and $\psi(t)$ is the group value of ψ
This function should satisfy the terms of continuity. Galerkin method is used to obtain the semi-discrete equation of the finite elements. By integrating the wave equation in volume V and based on the function of weight N, we have [16]:

$$\int_V \left[NN^T\ddot{\psi} + c^2(\nabla N)(\nabla N)^T\psi \right] dV = c^2\int_S N\frac{\partial\psi}{\partial n}dS \tag{9}$$

Where T indicates the stimulation that the structure applies on the fluid.
The matrix form of the previous integral is transformed as follows:

$$Q\ddot{\psi} + c^2 H\psi = c^2 b \tag{10}$$

The nature of interaction between the three parts of the engaged system has been shown below in a schematic figure [16]:

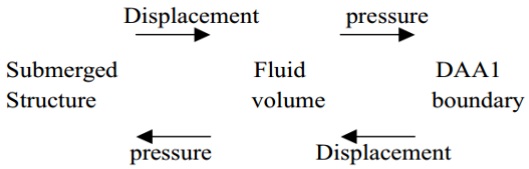

In fact, with the pressure being applied by the fluid volume on the structure, a response in the form of displacement is elicited on the fluid volume and then the fluid receives the pressure from the transfer boundaries and receives it as a displacement quantity again. It is noteworthy that in case there is no cavitation, it is possible to ignore the model of fluid volume and achieve a method called surface approximation methods, in which the structure engages the DAA boundaries or other approximation methods.

2-5-2. Wet surface approximation for problems close to the free surface

In these methods, the fluid-structure interaction has been merely considered based on wet structure surface approximation methods. The motion equation of the structure and DAA equation will be used with the compatible relationship between the particles and the structure for solving the interaction system and the dynamic response of the structure [17].
The equation of asymptotic approximation that is of the first rank is derived as follows [17].

$$M_f\,\dot{p}_s(t) + \rho c A_f\,p_s(t) = \rho c M_f\,\dot{u}_s(t) \tag{11}$$

Where M_f is the matrix of the fluid mass for the wetted surface of the fluid mesh (attached to the structure) and $u_s(t)$ is the velocity vector of fluid particles and vertical particles of the wetted structure surface [17].
Equation 11 is referred to as the doubly asymptotic approximation as it incorporates the system behavior in both of high and low frequencies (or the initial and final intervals) of the responses. The compatibility equation between the fluid and structure is as follows:

$$G^T\dot{x} = u_i + u_s \tag{12}$$

This equation states that the speed of fluid particles and that of the structure elements on the wetted surface of the structure are the same. This means that the particles move together. By insertions in equation 11, one can writes:

$$M_s\ddot{x} + C_s\dot{x} + K_s x = -GA_f\left[p_i(t) - p_s(t)\right]$$
$$M_f\,\dot{p}_s(t) + \rho c A_f\,p_s(t) = \rho c M_f\left[G^T\ddot{x}(t) - \dot{u}_i\right] \tag{13}$$

The above equations are solved for x and p_s values in temporal steps. The promoted DAA method of the second rank is also available. However, the surface approximation methods cannot show the cavitation impacts at the time of shockwave incident on the hull and their reflections and the resulting cavitation beneath the ship [17].

3-validation studies of scalar method principals for structure exposing to under-water explosion waves

3-1. Parametric discussion of tension wave propagation in finite element with explicit dynamic solution

In this section, parametric discussion of principals expressed about explicit dynamic solution and the manner of tension wave propagation in a block under explosive loading are presented considering principals. Parameters such as stability time and the effect of small or large mesh of finite elements and material selection on choosing stable time increment are addressed. As tension waves pass a block with the highest frequency, a very small time increment should be selected for achieving reactions with acceptable accuracy.

3-1-1. Model description

Intended block is made of steel, and its dimensions and load direction is shown in figure 2. In order to study a one-dimensional situation, boundary conditions are selected in such a way that all sides have free movement (roller support). In addition, free end of the block is exposed to an explosive loading with magnitude of 0.1 MPa and continuity time of $3.88 * 10^{-5}$.

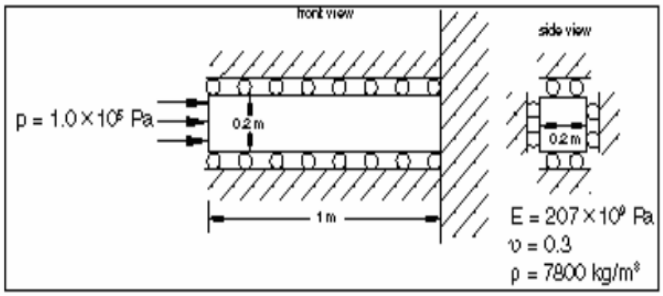

Figure 2. Side view of the model, material characteristics, and load applying method

Wave velocity within the steel can be calculated using material characteristics (ignoring Poisson effect).

$$C_d = \sqrt{\frac{E}{\rho}} = \sqrt{\frac{207\times10^9}{7800}} = 5.15\times10^3\ m/s$$

A wave having this velocity can reach the end of the related block which is 1 meter long after $1.94*10^{-4}$ s. Mesh should be chosen in such a way that it can show the tension passing the block adequately. Bathe proposed that the idea used in finite difference method can be used for cases in which we face wave propagation in an environment to select elements' dimensions and time increment [12]. Mesh dimensions are obtained by selecting 10 elements in each wave length and performing the following simple calculations:

$$L_{10el} = (3.88\times10^{-5})c_d = 0.2$$

The length of 10 elements is 0.2 m and as the length of one element is 1 m, 50 elements are obtained along the block. In addition, 10 elements are also selected in two directions perpendicular on wave propagation. Applied elements are of C3D8R (Eight-node brick element with reduced integration) type (figure 3).

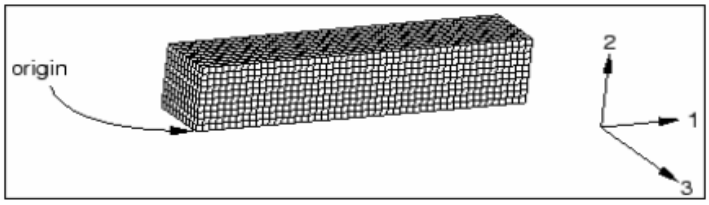

Figure 3. Meshing the block along wave propagation direction and perpendicular on it

3-2. Reaction of submerged shell structure to under-water explosive waves and bed reflection effect

Modeling the reaction of submerged structures with simple geometry to different kinds of under-water explosions is one of the most important parts of validating water and structure interaction codes. In this example, the ability of ABAQUS/Explicit software for modeling the interaction between spherical and cylindrical shell exposed to different shapes of shock waves resulted from under-water explosion, has been investigated. In addition, a parametric study is performed on the shape and type of explosion wave and the structure distance from the bed (reflection boundary). Obtained results are compared with DAA method discussed previously.

Interaction between a spherical and cylindrical elastic hollow shell and shock wave is investigated in planar shapes with time step function, in planar wave with exponential decay and in spherical wave with exponential decay. The magnitude of shock wave in all models is 1 MPa (except cylindrical shell model with step planar wave which is 1 Pa). Explosion resource distance from the reference point on the structure depends on the loading (planar or spherical). Exponential constant time for cylindrical and spherical shell loading is 0.0137^{ms} and 0.685^{ms}, respectively. Figure 4 shows the different types of loading used in this analysis. Symmetry properties are used in these models and suitable boundary condition is used in edges. Cylindrical shell are modeled with S4R elements and its surrounding fluid elements with AC3D8R elements while spherical shell is modeled with SAX1 elements and fluid environment with

ACAX4R for reducing calculation expenses. Spherical and circular non-reflective boundary (radiative) on outer surface of the fluid are considered as infinite boundary for circular and cylindrical shell, respectively. Figure 5(up and down) shows the structure and fluid model. Water and structure interaction will be performed based on the method explained in chapter 4 which is through surface interaction and explicit method during 27^{ms} for the sphere and 6.56^{ms} for the cylinder with time increments of $1*10^{-7}$. Explosion is along positive axis 2 for the sphere. The closest point to the explosion area is called the leading node and the farthest at the back of the sphere is called the trailing node in figure 5. The leading point is a place where shock wave reaches it at the first moment and it is also called the standoff point. As it can be observed, the radiative boundaries are also placed at the outer surface of the fluid. Properties of material used for the fluid and the structure based on Huang sphere [13, 14] are as follows:

Steel properties:

$$Radius\ of\ \ sphere = 1^{m}\ ,\ \rho_s = 7766\,{kg}/{m^3}$$

$$Radius\ of\ \ cylinder = 1^{m}$$

$$\nu = 0.3\ ,\ t_{sphere} = 2^{cm}\ ,\ t_{cylinder} = 2.9^{cm}$$

Fluid properties:

$$\rho_f = 997\,{kg}/{m^3}\ ,\ c = 1416\,{m}/{s}\ ,\ K_f = 2.128\times10^{9}\,Pa$$

Outer boundary radius for spherical shell=3 m

Outer boundary radius for cylindrical shell=2.03m

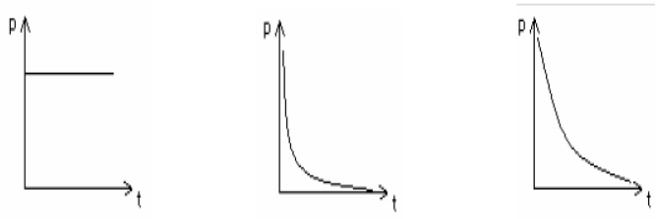

(I) (II) (III)

Figure 4. . different loading type used in this analysis: I) step incident load; II) shock wave with time constant of 0.0137 ms; III) shock wave with time constant of 0.685 ms

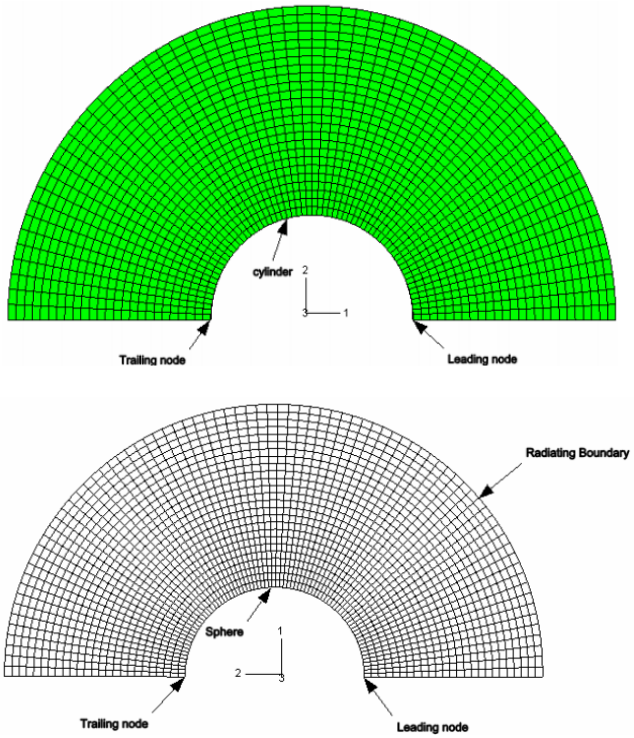

Figure 5. a view of symmetrical model with its surrounding fluid; Up) spherical shell in which explosion occurs along axis 2; Down) cylindrical shell in which explosion occurs along axis1

3-2-1. Studying pressure variations inside the fluid

In order to study this model and pressure variation in the fluid during the analysis more carefully, total pressure variations is shown in figure 6 for 0.006^{s} time increment. As it is observed, reflected wave reaches the structure after 0.003^{s}. Total pressure variations inside the fluid are plotted using total wave option. Pipe transformation is plotted in figure 7 from the analysis start until the end of it for 0.001^{s} time increment. As it can be seen in the following figures 8, when shock wave reaches the first point, i.e. standoff point, this point of the cylinder starts to transform. Reflected wave strikes the structure after 0.003^{s} and the cylinder starts moving perpendicularly.

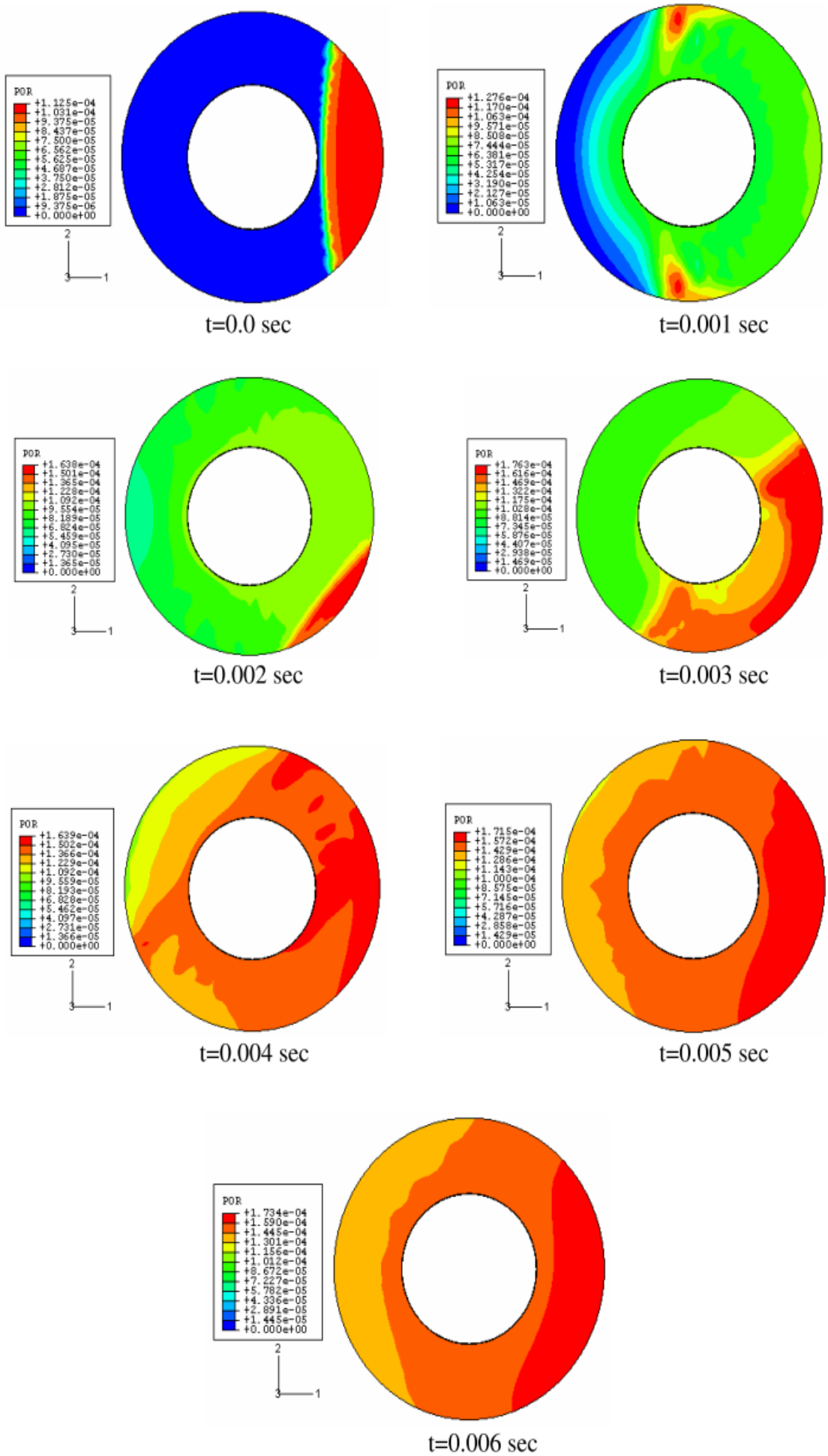

Figure 6. Total pressure variations in fluid field in Pas and based on 0.001-s time increment in scale 1*10-9

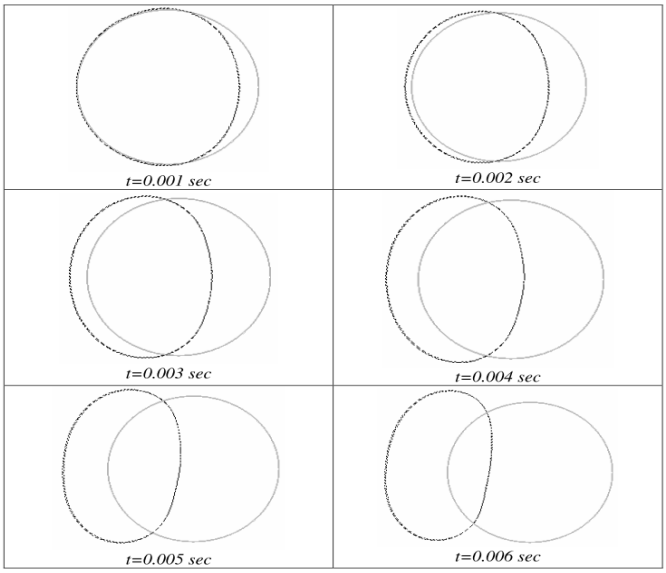

Figure 7. cylinder movement due to direct and bed-reflected waves from the beginning till the end of analysis with 0.001-s time increment

It can be generally said that bed reflection leads to reaction increase. This is because incident wave and reflected wave have the same sign. In order to better understand the results, cylinder transformation in the last time increment is plotted in figure 10 for different magnitudes of incident wave.

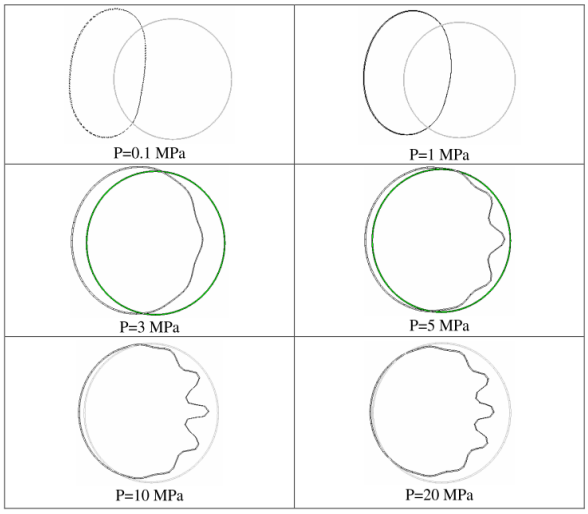

Figure 8. Cylinder transformation regarding the magnitude variations of incident wave at moment 0.006 s in scale 1000

It is better to study total pressure variations in fluid field in order to understand the procedure happened in this study. These variations are shown in figure 9. As it can be observed, when analysis and forward movement of the cylinder progress, points near the explosion resource face intense hydrodynamic pressure variation. In so far as some points one the cylinder receive very high pressure while the adjacent point on the structure and the surface opposite the explosion experience very low pressure. This pressure difference is due to the effect of the wave reflected from the bed which leads to transformation shown in figure 8.

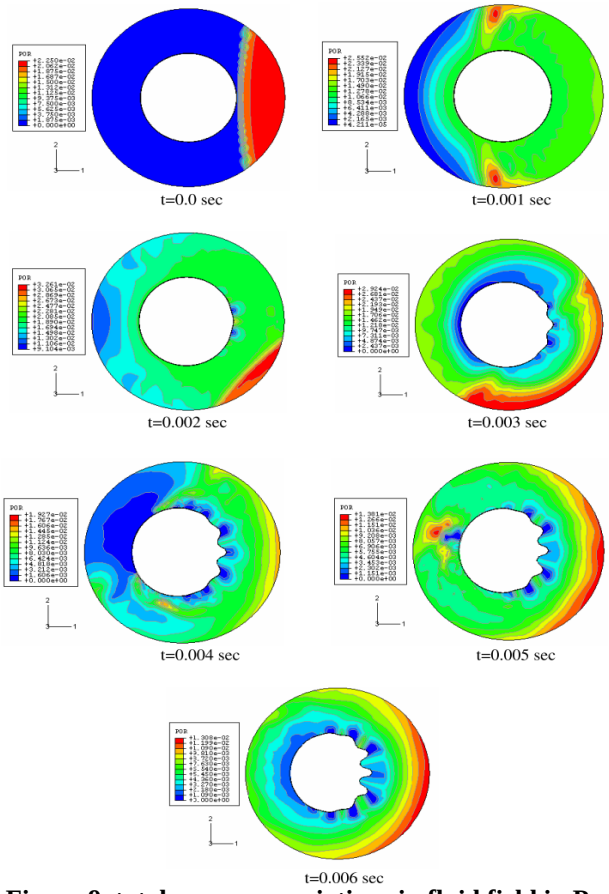

Figure 9. total pressure variations in fluid field in Pa and based on 0.001-s time increment and in scale $1*10^{-9}$

4- Problem statement and explaining its geometry

In this example, the shock wave created by 60 lb explosives HBX-1 (equivalent to 20.17 Kg TNT) is generated. The material of the cylinder was aluminum T6061-6. The characteristics of the materials used for water and the structure are as follows:

Aluminum characteristic:

$$\rho = 2784.5\,{kg}/{m^3}\ ,\ E = 7.56\times10^{10}\,Pa\ ,\ \nu = 0.33$$

$$Plasticity\ data\begin{cases} Yield\ Stress = & 3.0E+8Pa & 3.3E+8Pa \\ Plastic\ Strain = & 0.0 & 1 \end{cases}$$

Water characteristics:

$$\rho = 1000\,{kg}/{m^3}\ ,\ K_f = 2.1404\times10^{10}\,Pa\ ,\ c_f = 1463\,{m}/{s}$$

Geometry characteristics of the pipe and the shock wave are mentioned in the table 2.

Table 2. the cylinder's geometry characteristics and the magnificence of the shock wave

Length (m)	External diameter (m)	The thickness of the pipe wall (mm)	Distance to the free area (m)	The thickness of the end lid (mm)	The distance of the explosion source to the structure (m)	Shock wave magnificence MPa
1.067	0.303	6.35	3.66	25.4	7.62	15.7

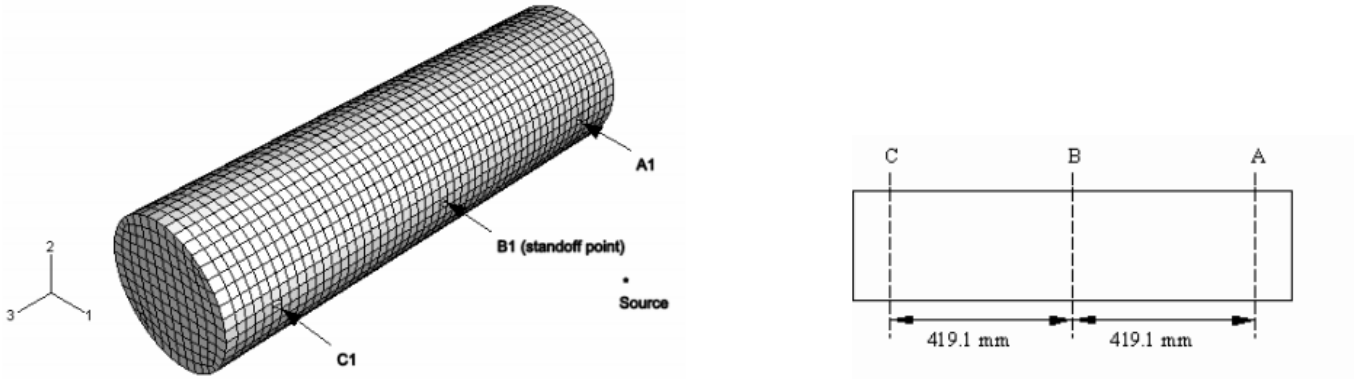

Figure 10. The site of displacement of the strain gauges, explosion source, and the reference point on the immersed pipe

The cylinder is placed horizontally at a depth of 3.66 m from a pool with a depth of 40 m. The explosive is also located at an identical depth perpendicular to the cylinder axis on its' center at a distance of 7.62 m of the external area of the cylinder. The depth of the location of the cylinder, the place of explosion and the time of experiment is in such a way that the cavitation effect, the gas bulb, the reflection from the walls, and the free area can be ignored (the assumption of lack of cavitation will be investigated). Strain gauges are placed at different positions from the external area of the cylinder (Figure 10) .The shock wave exerted is spherical which is shown in figure11. The magnificence of the shock wave is 15.7 MPa.

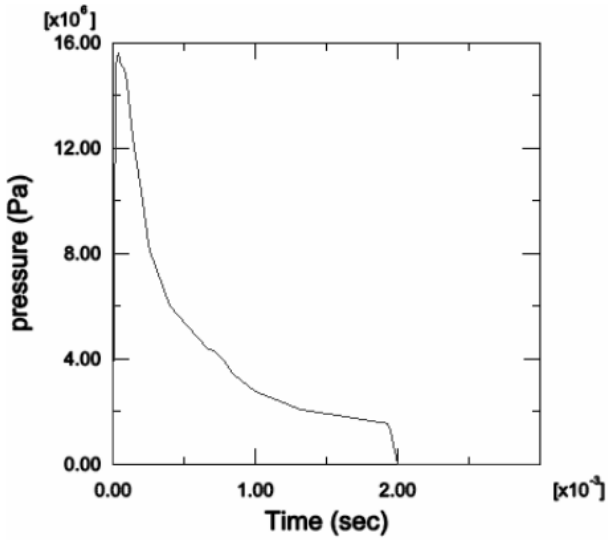

Figure 11. The graph of the wave induced by the explosion under the water at a distance of 7.62 meters from the explosion source

To model the cylinder, shell elements S4R of limited components have been used. This meshing includes 2402 nodes and 2400 elements with 40 contextual divisions and 53 axial divisions, in such a way that the dimension of each element is almost 2 centimeters. The normal vector of the elements is towards the fluid. Nodes are places on the external area of the shell. End lids are dummy elements which are used with decreased mass and stiffness, and only indicate the thickness of the lids.

The external fluid is modeled by elements of the AC3D8R four dimensional model. External boundaries of the Radiating boundary condition (Nonreflecting) of the fluid has been modeled by two cylindrical and spherical parts. On the basis of the equations given in chapter four for the calculation of the distance of reflective boundaries, this value is obtained equal to 0.457 m, but according to the conducted studies, here to reduce the effects of the added mass on the first bending mood of the structure for lower frequencies, twice its value brings upon a better result [15]. Therefore, a study was conducted on the basis of the varying distances of the two infinite cylinders between which is filled with water, to determine the ratio of the added mass at the lowest bending mood of the structure. The results are presented in table3. As it can be seen, in a radius, 6 times as the internal radius of the cylinder, the percent of error induced by added mass to the first bending structure is 5.7% relative to the infinite boundaries. On the other hand, Belvin conducted a parametric analysis on the basis of the ratio of the external infinite cylinder radius to the internal infinite cylinder radius whose context was filled with water, to determine the error induced by the effect of the added mass of the fluid on the structure. His results showed that for the external cylinder radius in the limit of 6 times as the internal cylinder radius, the error of the ratio of the added mass to the first bending mood of the structure is almost 6 percent relative to the infinite boundaries [16]. This result is consistent with the result obtained here. Therefore, for the distance of reflective boundaries to the model center, the value of 0.915 meter is used. To mesh the fluid in contact with the structure, the seeding of 0.04 m with the division of 24.4 elements in each sound wavelength with a frequency of 1500 Hz, and in the boundary part, the thicker seeding whose seeding is 0.1 m, i.e. 9.7 element in each sound wavelength with a frequency of 1500 Hz is used. This characteristic leads to reduced calculation costs

The system involved between the fluid and the structure in this example is between the hydrodynamic pressures induced by the sound waves which is

present in the fluid, and displacements of the cylinder in their contact. Here, the surface intra-action solution method has been used. Because the fluid mesh is thicker, the fluid area is considered as the Master and the structure area is considered as the slave.

Table 3. the ratio of the mass added to the structure in the effect of variations of external boundary radius

Cylinder Radius Ratio (R_0/R_i)	Added Mass Ratio (External boundary/Infinite Domain)
1.5	2.500
2.0	1.665
4.0	1.141
6.0	1.059
8.0	1.031
16.0	1.007
24.0	1.002

5-Results

The analysis occurs at 0.008 seconds (similar to laboratory conditions) by explicit method. The stable time step is calculated 1.69×10^{-6} for critical elements in pre-processing point. In the first part of results, the general condition of the case such as reasonable amount of kinetic energy and strain energy and the amount of plastic energy and the total amount of energy will be discussed using the internal energy of structures charts. Fig. 12 indicates that as soon as the shock wave loading finishes and the pipe begins vibrate while the kinetic energy ALLKE increases, at the same time the strain energy ALLSE is beginning to decrease. When the pipe is at its maximum deformation, the maximum amount of strain energy occurs, while in other times when the pipe is vibrating, the strain energy is at its minimum. Considering that ALLPD plastic strain energy is reaching to a stable situation, then it increases after a while. It is shown from the kinetic energy plot that the second bulge in the amount of plastic strain energy occurs when the pipe is returning from its maximum deformation. Therefore, the plastic deformation after shock wave loading can be observed. In ABAQUS, the element's hour-glassing deformations are controlled by the ALLAE quantity, virtual strain energy. It is shown that as the internal energy dissipates and plastic deformations of the pipe form according to structure's deformations, the amount of total internal energy itself is much higher than the amount of elastic strain energy. Therefore it is concluded that the virtual strain energy in this analysis is an energy quantum including the dissipated energy with elastic strain energy. ALLIE is the total internal strain energy including all internal energy quantities (ALLSE+ALPD+ALLAE). It is shown in Fig. 12 that the virtual strain energy is approximately 1% of the total energy. It shows that in this analysis, the hour-glassing deformations are negligible [17].

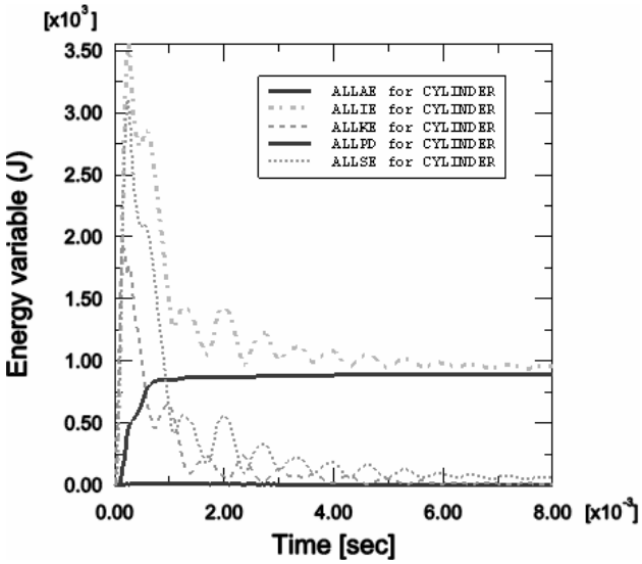

Figure 12. Comparison of the structure's internal energy and kinetic energy

As it is shown in the free vibration mode, the upper and lower points moving in opposite directions. In Fig. 13 this mode plotted on the scale of 40.

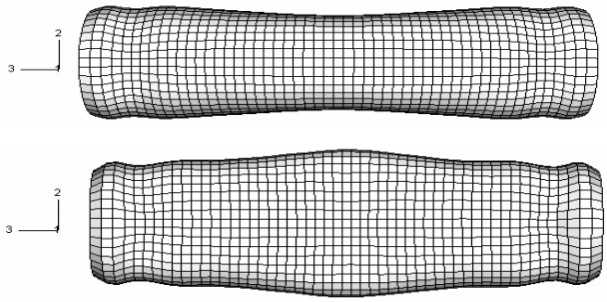

Figure 13. Breathing mode of plunged pipe in two different moment of analysis on the scale of 40

Another movement of the pipe is in 1 axial, actually two surfaces in front of and behind the explosion move towards the shock wave propagation. In Fig. 14 the deformation of this mode is plotted in two different times on the scale of 20.

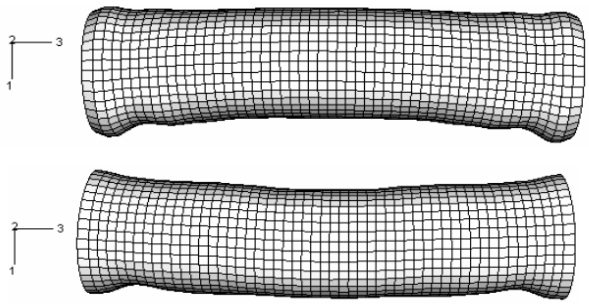

Figure 14. The whipping mode of plunged pipe in two different times on the scale of 20.

The tension obtained from ABAQUS analysis for two surfaces behind and in front of the explosion after 0.008 seconds and plotted in figures 15 and 16. As it has been represented, after a while the tension near the end crust of the pipe increases. As mentioned before, this happens because of the pipe's two ends thickness.

This can be observed in strain charts. The strain value is higher in A1, B1 and C1 strain gauges. The tension at the last moment of analysis for B1 obtained 145 MPa. Although the tension in this point is 272 Mpa, the accumulated equal plastic strain counter OEEQ is plotted in figures 17 and 18. It is shown that the accumulation of strain at the end of the pipe causes plastic deformation in this region.

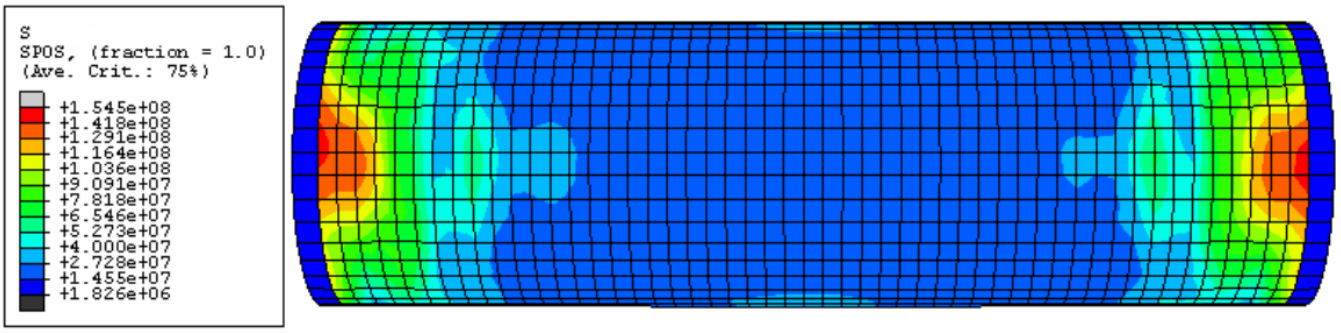

Figure 15. Tension counter on the front surface of explosion at 0.008 seconds.

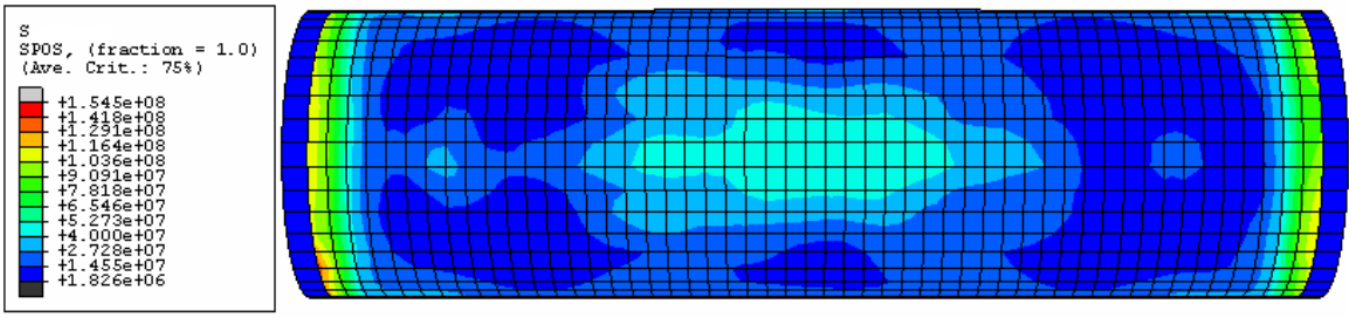

Figure 16. Tension counter on the back surface of explosion at 0.008 seconds.

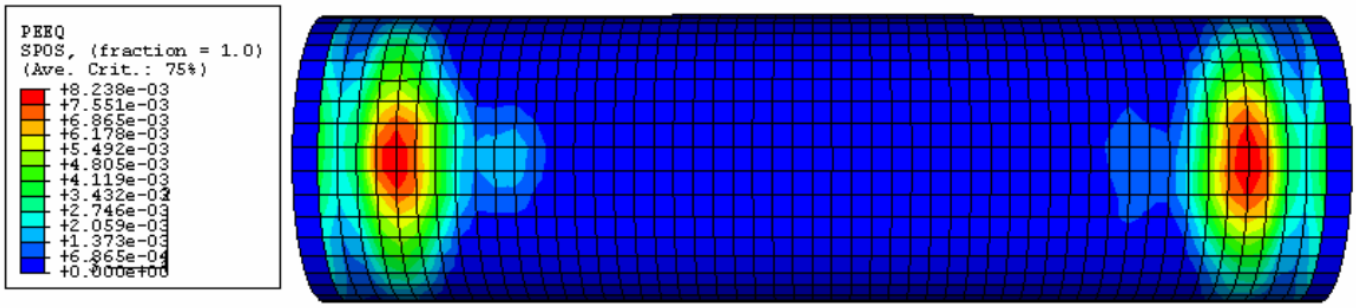

Figure 17. accumulated equal plastic strain counter on the front surface of explosion at 0.008 seconds

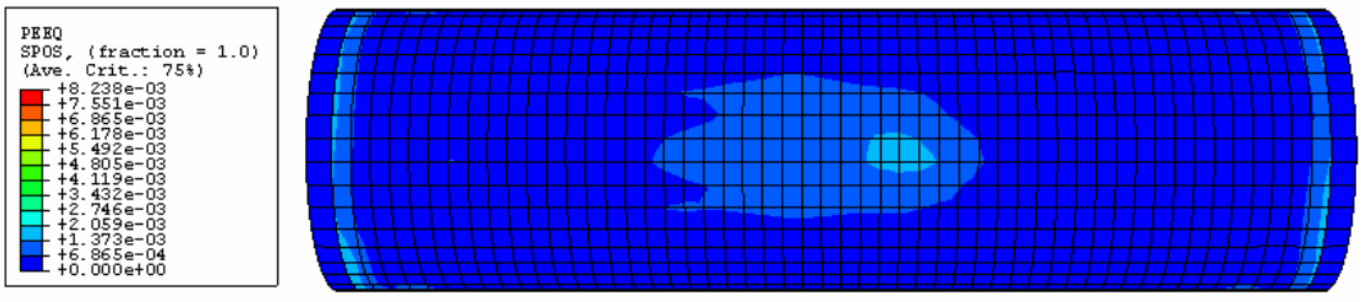

Figure 18. Accumulated equal plastic strain counter on the back surface of explosion at 0.008 seconds

As said before the cavitation created in this region is like a protection layer against shock wave harsh effects. Therefore, it can be pointed that cavitation is the cause of decreasing the strain in this point. Fig. 19 indicates the deformation at 0.008 seconds. It is shown that deformation at the end is lower than the middle parts of the pipe. Fig. 20 and Fig 21 indicate total hydrostatic pressure caused by shock wave interaction with plunged pipe from the beginning to the end of the analysis.

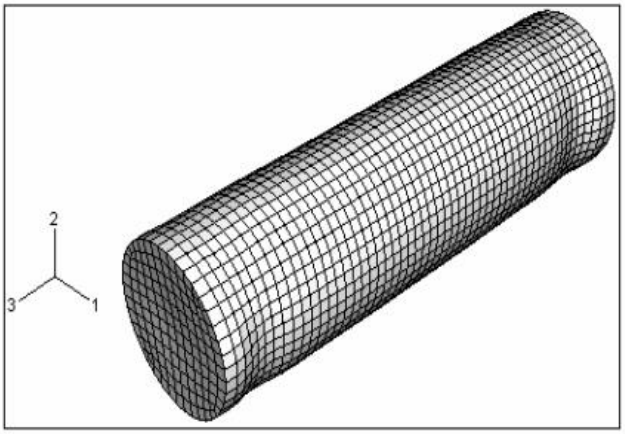

Figure 19. . Deformation of the pipe at 0.008 seconds on the scale of 20.

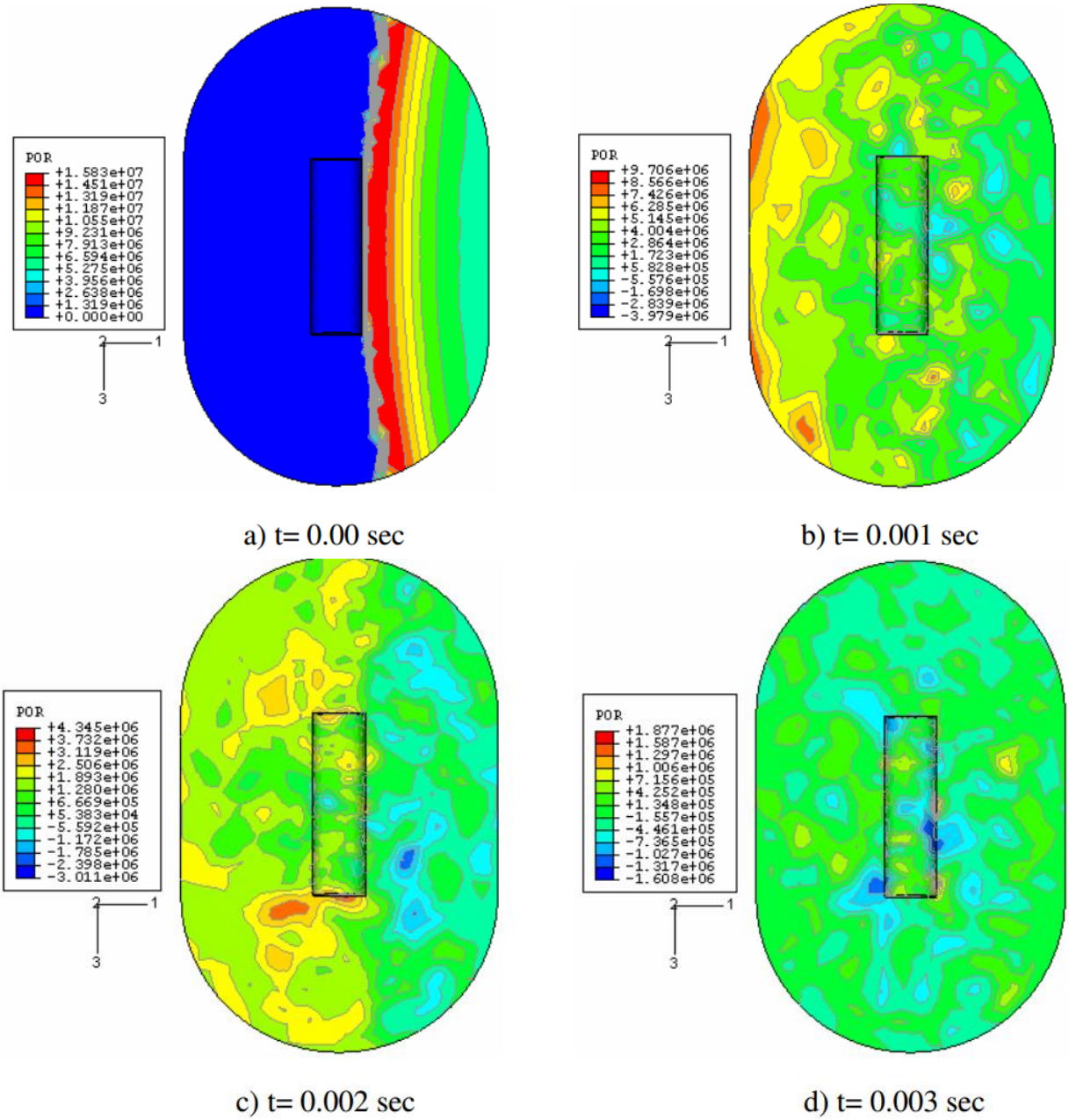

Figure 20. Total hydrostatic pressure caused by shock wave interaction with plunged pipe from the beginning to the end of the analysis.

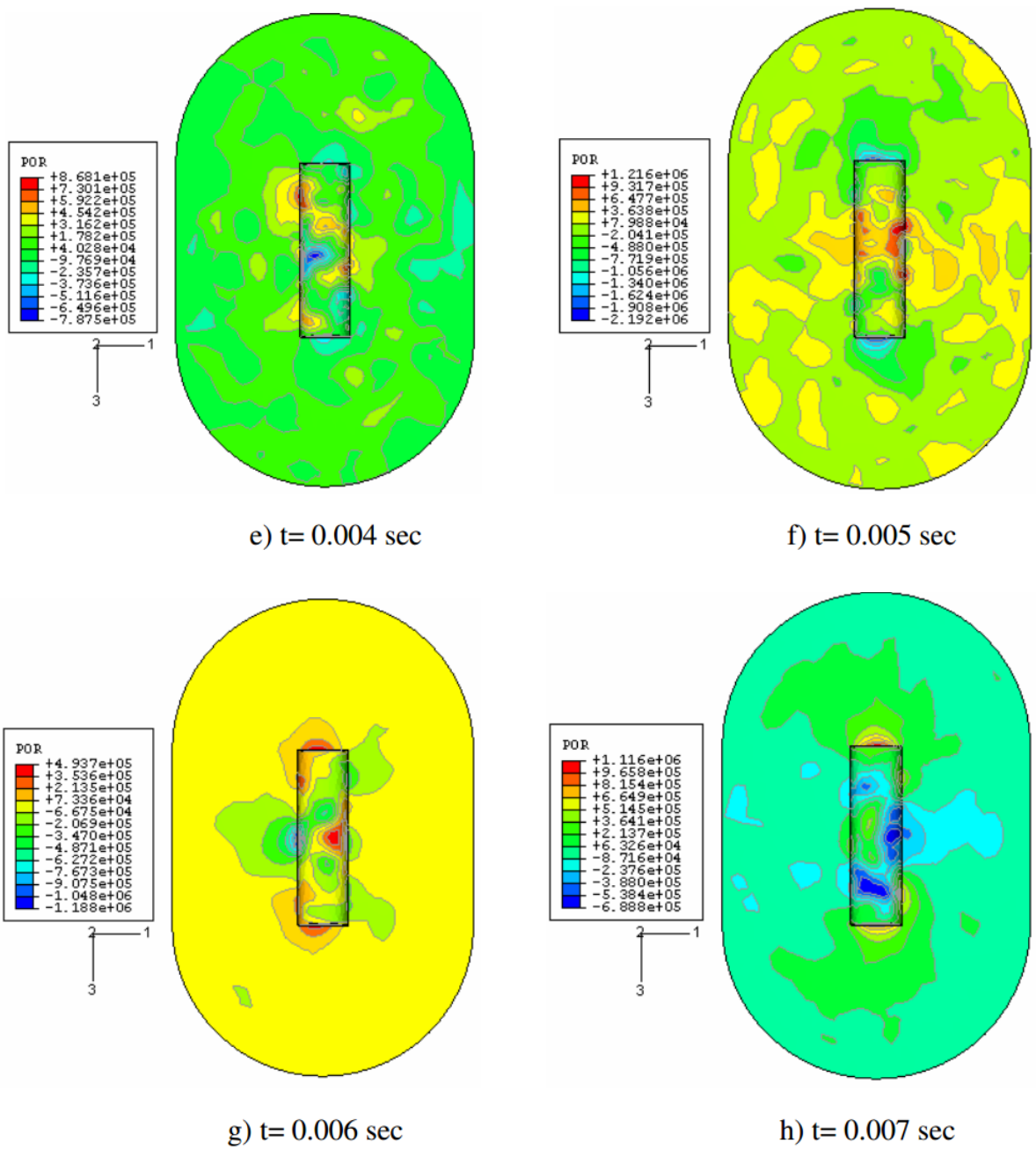

e) t= 0.004 sec

f) t= 0.005 sec

g) t= 0.006 sec

h) t= 0.007 sec

Figure 21. Total hydrostatic pressure caused by shock wave interaction with plunged pipe from the beginning to the end of the analysis.

6-Conclusion

As it is noted in the topic of underwater explosion, water and construction interaction derived from, explosive waves which we are dealing with different issues such as a dynamic equation selection method governed fluid particles movement, reasonable hypothesizes about them and the function field of these equations, different boundary conditions such as radiation boundaries, reflective boundaries and interaction boundaries, selecting a proper solution method for the system involved with water and construction after explosion and selecting a proper solution method for time step and dimension of usable elements, the pulses derived from gas bubbles model and so on. The following results are obtained for some of the above factors in this research, after the related modeling. As the result of analyze, it could be mentioned that in this level of issues where the system totally is involved between the construction movements and the sound pressure, the construction responses are according to the following:

The response with low frequencies is recognized by construction wavelengths which basically are significantly smaller than the sound wavelengths. In this situation, the effect of the external fluid is as an added mass upon the wet surface of the construction. The high frequency response is recognized by the construction wavelengths which basically are significantly bigger than the sound wavelengths. In this situation, the effect of the external fluid is as a simple damping mechanism, so that the energy from the construction to radiative bound (zone) is transferred by sound hydrodynamic waves. The medium frequency response is recognized by the

construction wavelengths which are equal with the sound wavelengths. During this frequency diet the external fluid is acting under two effects, the added mass and the damping effect upon the construction.
Determining the place of radiation boundary in interaction of water and construction derived from underwater explosion is very important, because it should be able to show the highest created wavelength adapted to the lowest frequency governed on fluid field. As it mentioned in these frequency values, the fluid is acting as the added mass on the construction. So the radiation boundaries must be in a position where it shows the minimum error from fluid added mass on first flexural mode. A parametric study upon a pipe float showed that at distance about 7 times of internal cylinder's radius, radiation boundaries had the minimum effect of added mass on first flexural mode. Also the research showed that in reflective boundary conditions, reflected waves from the seabed causes the increasing of responses, however the waves which are reflected from the surface of sea causes the reduction of responses. This effect with a time difference in construction responses is due to more distance which the reflected wave moves to arrive to the construction surface from fluid field external surfaces. Moreover, a parametric study on shock wave amplitude changes represented that some parts of construction around the explosive supply are affected by hydrodynamic pressure extreme changes. This factor creates irregular deformations in this surface of pipe. According to parametric studies, it is represented that plane waves is creating a stronger effect with the time step function. Also in this kind of loading, construction response in final seconds of analyze does not fluctuate between zero amount, against loading by reduction exponential time function. As it was noted in Kwon and Fox cylinder modeling when the shock waves arrive to the float construction, the area of pipe near the explosive supply in primary seconds is involved cavitation. It is the effect which was not paid attention in previous researches. So the hypothesis, the cavitation area can act as a protective layer for the construction against shock waves. The obtained results for near and far strain gauges from explosive area upon the construction, represents the accuracy of the claim. Moreover, this result suggests that DAA method is not applicable enough for areas with high probability of cavitation.

7- References

1- Cole, R. H. (1965). *Underwater explosions. Dover Publications.*

2- Mair, H. U. (1999). *Benchmarks for submerged structure response to underwater explosions. Shock and Vibration*, 6(4), 169-181.

3- Felippa, C. A., & DeRuntz, J. A. (1984). *Finite element analysis of shock-induced hull cavitation*. Computer Methods in Applied Mechanics and Engineering, 44(3), 297-337.

4- Geers, T. L., & Hunter, K. S. (2002). *An integrated wave-effects model for an underwater explosion bubble.* The Journal of the Acoustical Society of America, 111(4), 1584-1601.

5- Zhang, Z., Wang, L., & Silberschmidt, V. V. (2017). *Damage response of steel plate to underwater explosion: Effect of shaped charge liner*. International Journal of Impact Engineering, 103, 38-49..

6- ABAQUS, Users' *Manual, and Theoretical Manual*. "version 6.7, ABAQUS." (2008).

7- Felippa, C. A., & DeRuntz, J. A. (1991). *Acoustic fluid volume modeling by the displacement potential formulation, with emphasis* on the wedge element. Computers & structures, 41(4), 669-686.

8- Sprague, M. A. (2002). *Advanced computational techniques for the analysis of 3-D fluid-structure interaction with cavitation*(Doctoral dissertation, University of Colorado).

9- Jiang, J., & Olson, M. D. (1996). *Non-linear transient analysis of submerged circular plates subjected to underwater explosions.* Computer methods in applied mechanics and engineering, 134(1-2), 163-179.

10- Geers, T. L. (1978). *Doubly asymptotic approximations for transient motions of submerged structures.* The Journal of the Acoustical Society of America, 64(5), 1500-1508.

11- Dyka, C. T., & Ingel, R. P. (1998). *Transient fluid-structure interaction in naval applications using the retarded potential method*. Engineering analysis with boundary elements, 21(3), 245-251.

12- Shin, Y. S. (2004). *Ship shock modeling and simulation for far-field underwater explosion.* Computers & Structures, 82(23-26), 2211-2219.

13- Li, S., Li, X., Wang, Z., Wu, G., Lu, G., & Zhao, L. (2016). *Finite element analysis of sandwich panels with stepwise graded aluminum honeycomb cores under blast loading. Composites* Part A: Applied Science and Manufacturing, 80, 1-12.

14- Huang, H. (1969). *Transient interaction of plane acoustic waves with a spherical elastic shell.* The Journal of the Acoustical Society of America, 45(3), 661-670.

15- Zhang, W., & Jiang, W. (2017). *Research on the shock resistance optimal design of small-sized submerged vehicle subjected to non-contact underwater explosion.* Proceedings of the Institution of Mechanical Engineers, Part M: Journal of Engineering for the Maritime Environment,

16- Blevins, R. D. (1979). *Formulas for Natural Frequencies and Mode Shapes*, Robert E.

17- Reismann, H., & Pawlik, P. S. (1991). E*lasticity, theory and applications*. Krieger Publishing Company.

INTERNATIONAL JOURNAL OF
COASTAL & OFFSHORE ENGINEERING IJCOE Vol.3/No. 1/Spring 2018 (35-43)

Available online at: http://ijcoe.org/browse.php?a_code=A-10-195-1&sid=1&slc_lang=en

Prediction of Structural Response for HSSCC Deep Beams Implementing a Machine Learning Approach

Mohammad Mohammadhassani[1*], Mahdi Zarrini[2], Ehsan Noroozinejad Farsangi[3], Neda Khadem Gerayli[4]

[1] **Corresponding Author: Academic Staff of Seismology Engineering & Risk Department, Road, Housing & Urban Development Research Center (BHRC), Tehran, Iran; m.mohammadhasani@bhrc.ac.ir*
[2] *Academic Staff, Islamic Azad University, Astanee-Ashrafiye Branch, Iran*
[3] *Academic Staff, Department of Earthquake Engineering, Graduate University of Advanced Technology, Kerman, Iran*
[4] *Technology management, technology transfer, master of science, transportation research institute, road, housing and urban development research (BHRC), Tehran, Iran*

ARTICLE INFO

Article History:
Received: 19 Apr. 2018
Accepted: 20 Jun 2018

Keywords:
Deep Beam
Artificial Intelligence
Deflection
HSSCC

ABSTRACT

High Strength Concrete (HSC) is a complex type of concrete, that meets the combination of performance and uniformity at the same time. This paper demonstrates the use of artificial neural networks (ANN) to predict the deflection of high strength reinforced concrete deep beams, which are one of the main elements in offshore structures. More than one thousand test data were collected from the experimental investigation of 6 deep beams for the case of study. The data was arranged in a format of 10 input parameters, 2 hidden layers, and 1 output as network architecture to cover the geometrical and material properties of the high strength self-compacting concrete (HSSCC) deep beam. The corresponding output value is the deflection prediction. It is found that the feed forward back-propagation neural network, 15 & 5 neurons in first and second, TRAINBR training function, could predict the load-deflection diagram with minimum error of less than 1% and maximum correlation coefficient close to 1.

1. Introduction

There is no direct method for deflection prediction of deep beams. In general, the varieties of effective parameters on deep beam design are issues for applying of new method in design and prediction of deflection in these special structural elements. It is interesting and important to predict the shear behavior and loads transferring to reinforced concrete members with regards to the different load transferring system. Notwithstanding, lots of research has been done in the several last decades and the outcomes are implemented in structural design codes (e.g. ACI 318-02 Code [1], NZS [2]), it is not yet fully understood the exact mechanism of the load transferring in elements that shear deformation is dominated. Nevertheless, the code provisions do not fulfill design of elements such as deep beam and corbels. Although, in the last 50 years, extensive research has been conducted on the design and behavior of deep beams and some progress has been made [3-13], there is no exact method for designing and behavior prediction of these special structural elements. It should be noted that even in the structural design guidelines like British code BS8110 [14], ACI Codes, Euro code EC/2 [15], the Canadian code and the CIRIA guide No.2b [16], the design procedure of deep beams is not covered appropriately and the given information are mainly based on the empirical analysis.

In design and serviceability prediction of structural elements, the material properties and action, laws of mechanics, feeling and engineering judgement, past experience and analysis techniques should be considered. With regards to excessive parameters that affect on the design and behaviour of deep beams such as the concrete strength, the effect of web reinforcement, the effect of tensile reinforcement ratio, the shear span-depth ratio, the length of deep beams and the effective depth and the lack of exact design process, there is a need to search the modern and exact method for prediction of deflection and other serviceability purpose emphasizing the economical and technical justification.

In the last two decades, attempts have been made to computerize the design process, behaviour of concrete

elements and their serviceability using machine learning techniques such as artificial neural networks (ANN). The advantage of using the ANN is that it could learn from available designs during training process. ANN is a powerful knowledge surfaced from simulation of human brain and has been successfully applied in many fields of civil and structural engineering that demonstrate powerful problem solving ability [17], [18], [19], & [20]. Although, this technique is based on simple principles, its mathematical nature includes non-linear iteration that are useful in deep beam behaviour prediction. When the experimental samples consist of high dimension of elements, the data gathering to formulate the problem for other size of the structures would be difficult. Therefore, ANN could help to generate output for other dimension and parameters of structures by implementing a simulation procedure based on practical results.

In the literature, Artificial neural networks have been used to predict the ultimate shear strength of reinforced concrete deep beams (Sanad&Saka 2001)[21], design of fibre reinforced concrete beams (Hadi 2002)[22], shear design of reinforced concrete beams (Cladera & Mari 2004)[23,24], design for cable stayed bridges (Namhee Kim et al 2002)[25]. Moreover, some researchers (Rajasekharan & Vijayalakshmi Pai 2003[26], and Davis 1991[27]) have been investigating the main principals of neural networks in their studies.

In current research, the experimental results of load-deflection analysis of several High Strength Concrete (HSC) deep beams with different parameters have been applied to generate ANN for deflection prediction. The number of hidden layer, neurons in each hidden layer [28], and the type of selected function in data processing are the main parameters to simulate a network with minimum error and maximum correlation coefficient that have been discussed in this study. The outcome indicates that the ANN are capable of predicting the structural response in HSC deep beams much better compared to conventional statistical techniques, adapting its complex formulation and simulation procedure.

Materials and Method:

Experimental study

Six high strength self-compacted concrete (HSSCC) beams have been designed and casted. It was decided that the tensile reinforcement percentage to be variable, whilst beam's length, depth and thickness to be considered as constant parameters.

The reason for choosing HSSCC is that, it is a highly flowable, non-segregating concrete that can fill the formwork and encapsulate the reinforcement without any need for consolidation. Because of the high volume of reinforcement in a deep beam, to resolve the vibration problem use of SCC would be a reasonable choice. The HSSCC mix design is given in Table 1 (Further details can be found in [29]). In the mix design a local aggregate with maximum 20 mm diameter. Ordinary Portland cement, natural river sand and micro silica and Super plasticizer were used. The concrete mix has the W/C ratio of 0.27, which kept constant for all beams.

Table 1: The HSSCC mix design used in this study

Parameter	Value
Characteristic cube strength	*75 MPa*
Aggregate type	*Crushed granite and natural sand*
Cement type	*Ordinary Portland cement*
Slump of concrete	*More than 600 mm*
Coarse aggregate content	*553 kg/m^3*
Fine aggregate content	*887 kg/m^3*
Water/binder	*0.25*
Silica fume/cement	*0.1*

The main characteristics of self-compacting concrete is its workability; as shown in Figure 1, it can be controlled for all casting in the accepted range. Further information on the HSSCC mixing process and the results of the material tests can be found in [29].

Figure 1: The flow ability of self-compacting concrete (slump=600 mm) in B1 and B2 mix design.

To reduce the risk of segregation in the used mix design, it was decided to keep the flow ability in the range of 550 to 740 mm. For each beam, nine cubes (100 mm × 100 mm × 100 mm) and three cylinders (150 mm diameter, 300 mm high) were casted as control specimens. Cubes were tested for measuring strength at 7 days, 28 days, and the age of loading and cylinders were tested for splitting tensile strength at 28 days. All cylinder and cube samples used for strength control were demoulded after 24 hours and cured for age of tested beams in humidity conditions.

The beams were casted in a steel mould and demoulded after 3 days. During this period, the test samples were covered with canvas and plastic. The

canvas was watered twice a day for 11 days, after which the framework was removed.

Figure 2: The casting arrangement and deep beam fabrication

The specifications of fabricated specimens including compressive strength (f'_c), tensile reinforcement ratio (ρ) and tensile reinforcement area (As) are given in Table 2. It should be noted, that the compressive strength given for each specimen (f'_c) is based on the average value of 3 cubic samples.

Table 2: The specification of tested beams

Specimen's Number	f_c' (MPa)	ρ (%)	As (cm^2)
B1	*91.5*	*0.219*	*1.91*
B2	*91.5*	*0.269*	*2.36*
B3	*91.1*	*0.410*	*3.83*
B4	*93.72*	*0.604*	*5.58*
B5	*79.1*	*0.809*	*7.60*
B6	*87.5*	*0.938*	*8.54*

The specifications of the reinforcing bars used in this study including yield (f_y) and ultimate stress(f_u) are given in Table 3. These values are extracted based on a number of samples taken from each batch supplied. As can be seen, all the used reinforcing bars were high tensile deformed bars except the smallest size which is non-deformed (Φ9).

Table 3: Bars specifications used in this study

Diameters of used bars (mm)	f_y (MPa)	f_u (MPa)
Φ9	353.0	446.0
Φ10	614.4	666.0
Φ12	621.6	678.4
Φ16	566.3	656.0

Beam Details

All deep beams had a section of 500 mm depth and 200 mm width and 1500 mm length. The beam details and geometrical parameters are presented in Table 4 and Figure 3 respectively.

Table 4: The bars specification in fabricated specimens

Beam's number	Tensile bar	d(cm)	a/d
B1	3 **Φ** 9	43.55	0.92
B2	3 **Φ** 10	43.85	0.91
B3	2 **Φ** 10+2 **Φ** 12	46.90	0.85
B4	2 **Φ** 10+2 **Φ** 16	46.20	0.86
B5	2 **Φ** 10+3 **Φ** 16	47.00	0.85
B6	1 **Φ** 8+4 **Φ** 16	45.50	0.88

As shown in Figure 3, the anchorage of the main tensile reinforcements was enhanced by providing 90-degree hooks at the bar ends to prevent bonding failure.

Test Setup and Loading Process

All tested specimens were simply supported and a 2 points monotonic static loading protocol was applied on with a hydraulic jack. The arrangement of test setup is illustrated in Figure 4.

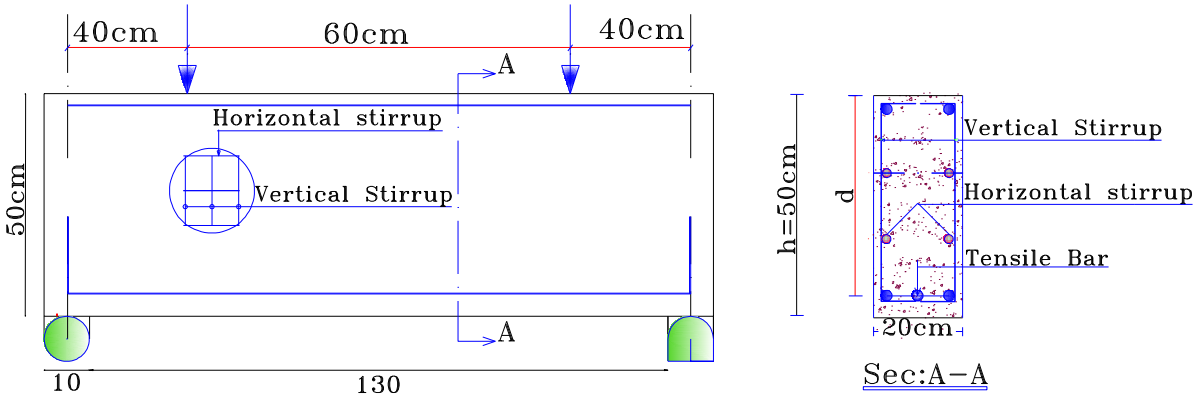

Figure 3: schematic representation of one of the tested specimen

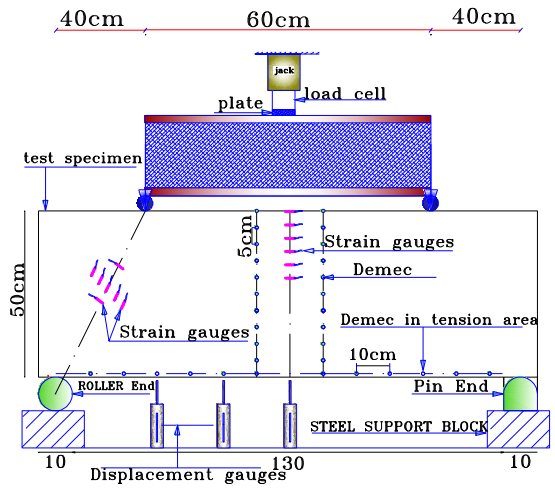

Figure 4: Test Setup arrangement

The beams were positioned on two steel cylinders with 5" diameters to simulate the simply supported boundary conditions. After the beam was centred and levelled, the steel beam was placed on the test specimen, and the loading was applied at midpoint at 20 KN intervals until the first crack occurred.
During the loading process, care has been taken into account to make sure that the supports will remain regular and other types of failure would not happen. At each increment, the deflection values and strain gauge readings were taken. After each reading and observation, the next loading stage increment was repeated, until the failure or an important observation was made.

Numerical Study

Artificial Neural Network (ANN) is a machine learning technique that works like human brain. The main units of the network are neurons that are connected together in a complex manner. They act parallelly and work as numerical processors. All machine learning algorithms including ANN learns to solve the problems based on relationship between experimental data. The effect of connections between neurons indicates the weight of each connection. The schematic structure of an ANN is shown in Figure 5.

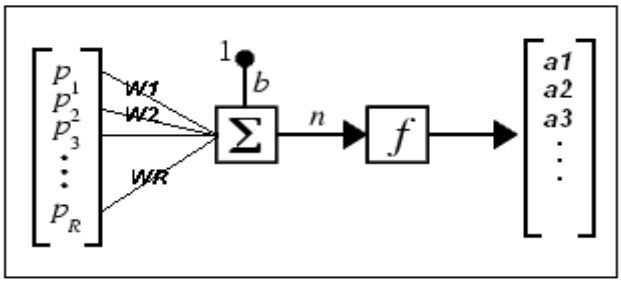

Figure 5: Neuron model with R-element in input model

The effect of (P) on (a) is defined by the weight (W). The other input is 1 (the constant amount) that was multiplied in bios (b) and then added with WP.
Based on the complexity of the problem, the architecture of the proposed ANN model can be a single or multi-layer network. The structure of the single and multilayer ANNs are shown in Figure 6. A typical multi-layer artificial neural network (MNN) includes an input layer, output layer and hidden layers of neurons. MNNs are sometimes known as layered networks.

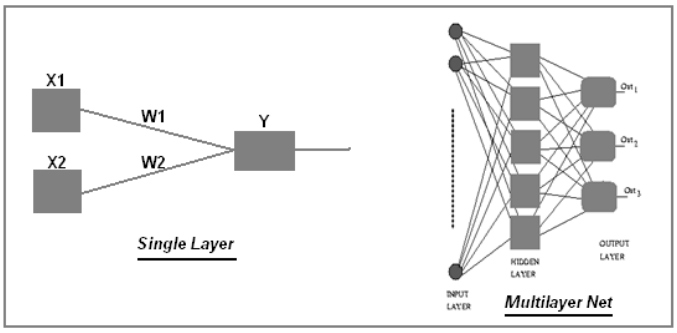

Figure 6: Single and multilayer network

In case of using MNNs, the computational ability will be significantly improved compared to a single layer ANN. In current study, the load-deflection analysis of six HSSCC deep beams with different parameter indicated in Table 5 has been discussed and the produced ANN model has been applied for deflection prediction of the deep beam.
model has been applied for deflection prediction of the deep beam.

Table 5: Different parameters of tested specimens in this study

Item	Parameters								
	f_{cu}	a/d	L_0/d	f_{yv}	f_{yh}	A_v/bs_v	A_h/bs_h	ρ	f_y
DB1	91.5	0.804	2.985	353.0	353.0	0.00640	0.00424	0.002191	353.00
DB2	91.5	0.798	2.965	353.0	353.0	0.00640	0.00424	0.002690	614.40
DB3	91.1	0.746	2.772	353.0	353.0	0.00640	0.00424	0.004090	618.00
DB4	93.7	0.757	2.810	353.0	353.0	0.00636	0.00669	0.006040	590.35
DB5	79.1	0.851	2.979	614.4	614.4	0.00785	0.00982	0.008088	585.54
DB6	87.5	0.769	2.857	614.4	614.4	0.00785	0.00982	0.009380	523.64

Table 6: Properties of the selected network (five best architectures)

Net. Market.	Neurons in Hidden Layer			Training Function	Adaption Learning Function	Training Transfer Function In hidden layer			Transfer Function in output layer
	H1	H2	H3			H1	H2	H3	
Net.1	10	1	-	TRAINBR	LEARNGDM	Tansig	Logsig	-	Purelin
Net.2	10	10	-	TRAINBR	LEARNGDM	Tansig	Logsig	-	Tansig
Net.3	10	5	-	TRAINBR	LEARNGDM	Tansig	Logsig	-	Purelin
Net.4	15	5	-	TRAINBR	LEARNGDM	Tansig	Logsig	-	Purelin
Net.5	15	5	-	TRAINBR	LEARNGD	Tansig	Logsig	-	Purelin

The parameters given in Table 5 are as follows:
f_{cu} = 28 days cylindrical strength of concrete
a = shear span
d = effective depth
L_0 = overall length of tested beams
b = the beam width
f_{vy} = the yield strength of vertical web reinforcement
f_{hy} = the yield strength of horizontal web reinforcement
A_v = the area of vertical web reinforcement
s_v = the distance of vertical web reinforcement
A_h = the area of horizontal web reinforcement
s_h = the distance of horizontal web reinforcement
ρ = the tensile bar percentage
f_y = the tensile bar yield strength and
The output load-deflection of B2 specimen was applied for network testing and the other deep beam outputs were used for verification and training stages. A total of 1084 data have been utilized to simulate the proposed network, 954 data for training process, 99 data for verification, and 31 data for testing stage. The architecture of the proposed ANN model includes ten neurons in input layer (f_{cu}, a/d, L_0/d, f_{vy}, f_{hy}, A_v/bs_v, A_h/bs_h, ρ, f_y, & *loading*) and one neuron in output layer (*deflection*). Feed-forward back propagation (FFBP) was constructed at the end of ANN. Twenty network architectures with different hidden layers and network functions have been selected from the five best networks ~~as~~ indicated in Table 6.

Training Algorithms
Bayesian Regularization (TRAINBR) & Levenberg-Marguardt Backpropagation (TRAINLM) algorithms were used for network training at the final stage. TRAINBR algorithm indicated the best compatibility with the given problem.

The Best Training and Transfer Function
Various type of functions with different architectures were investigated. The tray consisted of TONSIG for the first hidden layer, LOGSIG for the second hidden layer, and PURLIN for the output were indicated as the best training and transfer functions.

The Best Network Architecture
The best architecture was calculated by testing of different number of neurons in hidden layers. To this end, SSE and MSE method were used to determine the minimum error. The (10-15-5-1) architecture indicating 10 inputs, 15 neurons in the first hidden layer, 5 neurons in second hidden layer, and 1 output was selected as the optimum architecture.

Training
954 of 1084 normalized data in [0,1] have been utilized for training procedure.

Verification
In the proposed model, the stopping time of calculation has been applied to 99 data to determine the network structure that has not been used in training. data verification has been checked frequently in training stage. The operation function will run till an increment in error percentage occurred in the verification process.

Testing
Final step will be the testing process. To this, 31 data were used for testing procedure after training and verification stages.

Results and Discussion:
Serviceability of a structure/infrastructure is normally determined by its deflection and cracking. In general, the deflections of deep beams are small compared to those of normal beams and it was also indicated that the stiffness of the beam elements will be enhanced with increase in the section height leading to brittle failure. In this study, the experimental deflection's amount versus the load graphs are presented in Figure 7.

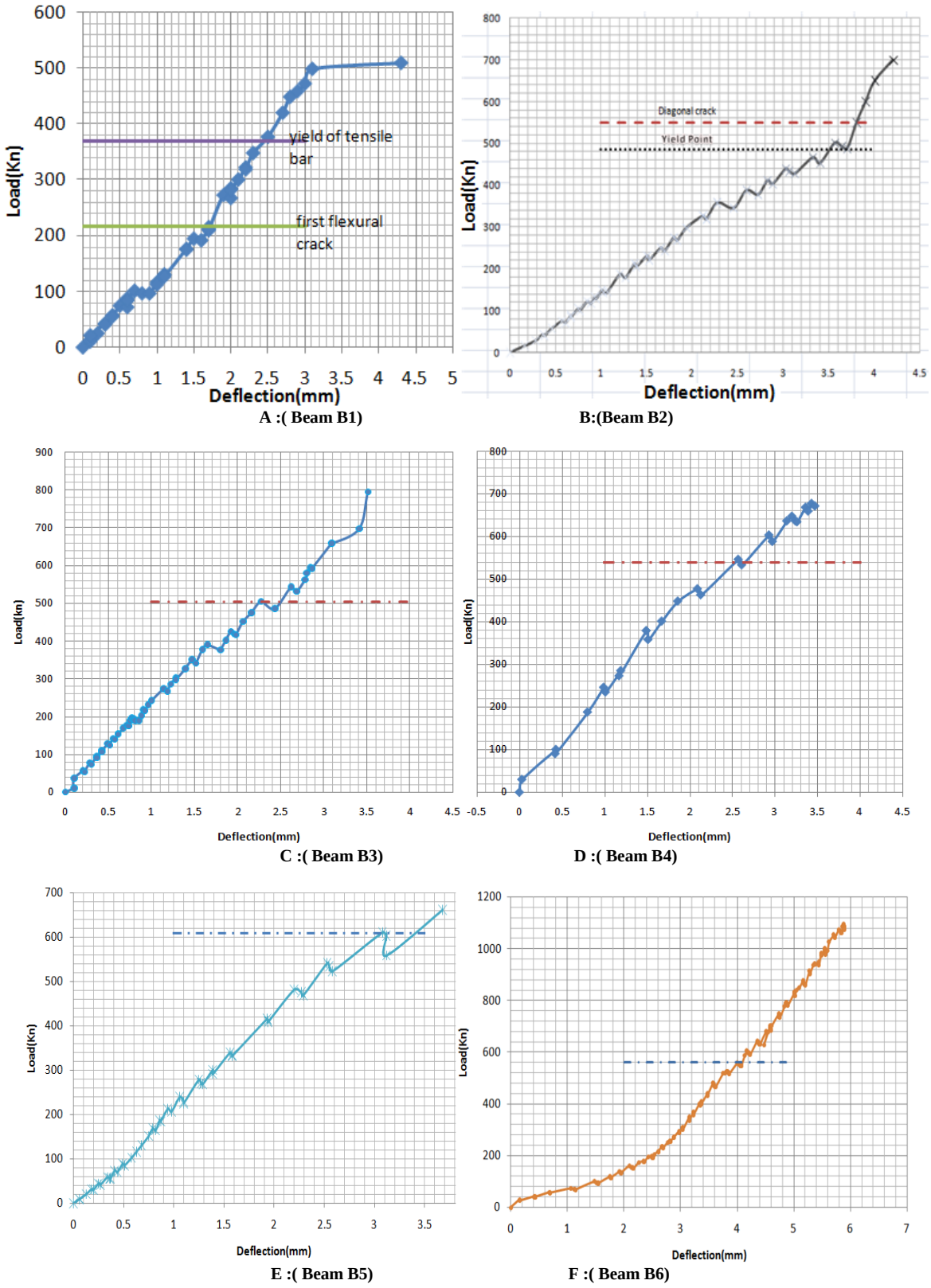

Figure7: The deflection of tested beams at the mid span

As depicted in Figure 7, a linear trend existed up to the yielding point of longitudinal bars and the ultimate strength at failure in the beams. As illustrated, failures mainly occurred at the points where peak loadings are applied Such the phenomenon is the result of shear deformation and brittle failures in deep beam structural elements. The area under the entire load-deflection diagram represents the absorbed energy during failure. The amount of this energy is a critical parameter for determining the structure's ductility. In general, ductility of a structure is characterized by the deformation at which the structure fails under a given type of loading. As can be seen in Figure 7, the absorbed energy increased with increment in tensile bar percentage.

As stated in the literature, high economical expenses and the different behavior of deep beams led to behavior prediction of these elements; however, the use of ANN based models as an innovative approach is not yet investigated by others. Deep beam design and failure prediction are impressed by two main assumptions in design. Firstly, these structural elements do not follow the Bernoulli assumptions that suppose section of bending plate remains plain after loading. Due to this property, these structural elements exhibit more than one neutral axis depth (Mohammadhassani [29], Raya [8]). Thus, the prediction of deflection is not possible by the equation used for normal beams.

Secondly, the shear deformation is dominated by failure in these structural element that lead failure in compression strut trajectories when the minimum tensile bar by codes are satisfied.

To this, the use of ANN based model can be a rational approach to predict the structural response of these complex structural elements. Table 7 gives the specification of simulated ANNs.

Table 7: The specification of input and procedure of networks

The deep beams used to generate ANNs	6 (B1, B2, B3, B4, B5, & B6)
The deep beams used for training & verification	5 (B1, B3, B4, B5, & B6)
The deep beams used for testing	1 (B2)
Number of data used for training, verification & testing	954, 99, & 31
The selected network architecture	10-15-5-1 (output-hidden1-hidden2-output)
Training & learning function	TRAINBR & LEARNGDM
Training transfer function in 1st & 2nd hidden layers	TONSIG & LOGSIG
Training transfer function in output	PURLIN

The training error for the five best networks, as shown in Table 6, was calculated and two important parameters [30]; the Mean Squared Error (MSE) and Root Mean Squared Error (RMSE) are presented in Figure 8. All network errors are in acceptable range and the Net.4 has the minimum error based on MSE & RMSE calculated values. The correlation coefficients for the 5 networks, are as well presented in Table 8, and were acceptable and closed to 1.

Table 8: Network Correlation Coefficient

Network	Net.1	Net.2	Net.3	Net.4	Net.5
Correlation Coefficient	0.986	0.990	0.985	0.992	0.990

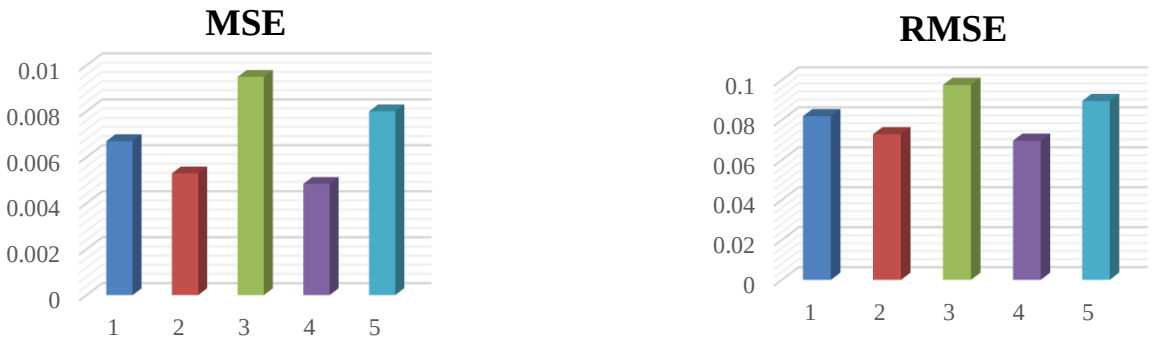

Figure 8: Calculated MSE & RMSE for the five best networks

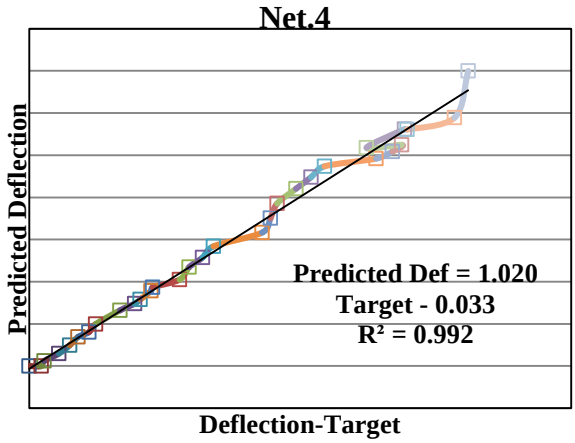

Figure 9: ANN response in deflection prediction

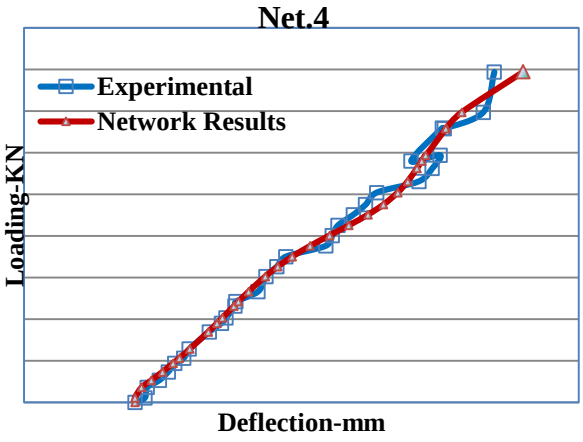

Figure 10: Evaluation of target and deflection prediction by ANN

As can be seen in figures 9 and 10, the feed forward back-propagation neural network, 10-15-5-1 (10 inputs, 15 neurons in first hidden layer, 5 in second hidden layer and 1 output) was set as optimum network architecture. TRAINBR training function, LEARNGDM learning function, TANSIG and LOGSIS were set as training functions in the first and second hidden layer. PURLIN transfer function in output layer can predict the load-deflection diagram with minimum error of less than 1% and maximum correlation coefficient closed to 1.

Conclusion

In regard to the different survived ANNs in current study, the (Net. 4) architecture has been selected for deflection prediction in HSSCC deep beams. The below results indicated that the proposed simulated network is very efficient for load-deflection prediction of these complex structural elements.

Training

The training RMSE for the generated network calculated as 0.979%

Verification

The verification RMSE for the generated network calculated as 0.962%

Testing

The testing RMSE and correlation coefficient for the generated network calculated as 0.696% and 0.992 respectively.

Finally, the results of this study reinforce the notation that machine learning techniques including artificial intelligence based models are practicable for establishing relations between loads and structural responses for the HSSCC deep beams.

References

1- ACI Committee 318. Building code requirements for structural concrete (ACI 318-02) and commentary (ACI 318R-02). Farmington Hills (MI): American Concrete Institute; 2002.

2- NZS 3101:1995. Concrete structures standard, NZS 3101: Part 1, Commentary, NZS 3101: part 2. Wellington: Standards Association of New Zealand; 1995.

3- Chemrouk M.(2006): Ultimate behaviour of Concrete Deep Beams with Particular Reference to Slender Deep Beams; proceeding of the 9th international conference on concrete Engineering & Technology 2006 (CONCET 2006)-'Structural concrete for the Millennium', 9-11 may, Kuala Lumpur.

4- Yang K.-H., Chung H.-S. and Ashour A. F. Influence of section depth on the structural behaviour of reinforced concrete continuous deep beams. Magazine of Concrete Research, 2007:59: 8575–586

5- Chemrouk M. and Kong F. K. High strength concrete continuous deep beams–with web reinforcement and shear-span variations. Advances in Structural Engineering, 2004;7: 3229–243.

6- Maco Rigoti, Diagonal cracking in reinforced concrete deep beam-An experimental investigation, PhD Thesis., Concordia University, Montreal, Quebec, Canada. 2002.

7- Schlaich, J. and Schäfer, K., "Design and Detailing of Structural Concrete Using Strut-and-Tie Models", *The Structural Engineer*, 69, 6, 1991, pp. 113-125.

8- Ray, S.P. (1980) Behaviour and Ultimate Shear Strength of Reinforced Concrete Deep Beams With and Without Opening in Web. Ph. D. thesis, Indian Institute of Technology, Kharagpur, India.

9- Perera R, Vique J. Strut-and-tie modelling of reinforced concrete beams using genetic algorithms optimization . *Construction and Building Materials*, 2009;*23:82914-2925*

10- Ashour A, Yang K.-H . Application of plasticity theory to reinforced Concrete deep beams: a review. Magazine of Concrete Research, 2008; 60: 9657–664.

11- Yang, K.-H., Chung, H.-S. and Ashour, A. F. Influence of section depth on the structural behaviour of reinforced concrete continuous deep beams. Magazine of Concrete Research, 2007; 59: 8 575–586

12- Kang-Hai Tan, Susanto Teng, Fung-Kew Kong, and Hai-Yun Lu. Main Tension Steel in High Strength Concrete Deep and Short Beams. Structural Journal, 1997;94:6 752-768.

13- Perera R, Vique J. Strut-and-tie modelling of reinforced concrete beams using genetic algorithms optimization . Construction and Building Materials, 2009;23:82914-2925

14- British Standard Institution, "Structural Use of Concrete" (BS 8110: Part 1. Code of Practice for Design and Construction), BSI, London, 1985.

15- Eurocode 2 1992. *Design of concrete structure, Part 1, general rules and regulations for building.* London: British standards institution.

16- CIRIA Guide 2. The design of deep beams in reinforced concrete. London: Over Arup and Partners, and Construction Industry Research and Information Association; 1977. p. 131. Reprinted 1984.

17- I.C. Yeh, "Modeling of strength of HPC using ANN", Cem Concr Res 28 (1998) (12), pp. 1797–1808.

18- J. Kasperkiewics, J. Racz and A. Dubrawski, "HPC strength prediction using ANN", ASCE J Comput Civil Eng 9 (1995) (4), pp. 279–284

19- S. Lai and M. Sera, "Concrete strength prediction by means of neural network", Constr Build Mater 11 (1997) (2), pp. 93–98

20- S.C. Lee, "Prediction of concrete strength using artificial neural Networks", Eng Struct 25 (2003), pp. 849–857

21- Sanad A, Saka M P 2001 Prediction of ultimate strength of reinforced concrete deep beams by neural networks. *ASCE J. Struct. Eng.* 127(7): 818–828

22- Hadi N 2002 Neural networks applications in concrete structures. *Compute & Struct.* 81: 373–381

23- Cladera A, Mari A R 2004 Shear design procedure for reinforced normal and high strength concrete beams using artificial neural networks. Part I: Beams without stirrups. *Eng. Struct.* 26: 927–936

24- Cladera A, Mari A R 2004 Shear design procedure for reinforced normal and high strength concrete beams using artificial neural networks. Part II: Beams with stirrups. *Eng. Struct.* 26: 917–926

25- Namhee Kim Hong, Sung-Pil Chang, Seung-Chul Lee 2002 Development of Ann-based preliminary structural design systems for cable-stayed bridges. *Adv. Eng. software* 33: 85–96

26- Rajasekharan S, Vijayalakshmi Pai G A 2003 Neural networks, Fuzzy logic and genetic algorithms, (New Delhi: Prentice Hall)

27- Davis L 1991 *Hand book of genetic algorithms*, (New York: Van Nostrand Reinhold)

28- Daniel A, Simon L, and Girma T. B., "Application of an Artificial Neural Network Model for Boundary Layer Wind Tunnel Profile Development", 11th American Conference in Wind Engineering, 2009.

29- Mohammadhassani Mohammad., Experimental and analytical study on HSC deep beam with particular reference to the stress/strain distribution and to the evolution of the neutral axis, PhD Thesis., University Malaya, Kuala Lumpur, Malaysia. 2010.

30- N. Pannirselvam, P.N.Raghunath, K. Suguna, 2008, Neural Networks for performance of Glass Fiber Reinforced polymer plated RC beam, American J. of Engineering and Applied Science 1, p82-88

INTERNATIONAL JOURNAL OF
COASTAL & OFFSHORE ENGINEERING
IJCOE Vol.3/No. 1/Spring 2018 (45-57)

Available online at: http://ijcoe.org/browse.php?a_code=A-10-70-1&sid=1&slc_lang=en

Evaluatoin of Incompressible and Compressible SPH Methods in Modeling Dam Break Flows

Hassan Akbari[1]

[1] *Assistant Professor at Tarbiat Modares University, Tehran, Iran, h.akbari@modares.ac.ir*

ARTICLE INFO

Article History:
Received: 27 Nov. 2017
Accepted: 15 Jun. 2018

Keywords:
ISPH
WCSPH
Accuracy
Stability
free surface boundary

ABSTRACT

Smoothed Particle Hydrodynamic (SPH) is an attractive Lagrangian tool for simulating flows with large displacement at free surface boundary. Two widely used subcategories of this method are Weakly compressible SPH (WCSPH) and truly Incompressible SPH (ISPH) methods. Each method has its individual advantages while there is not yet a global agreement about the preference of one method to another one. In this study, accuracy, stability and efficiency of these methods are compared in simulating dam break flow as a well-known hydraulic problem. To decrease unrealistic particle fluctuation especially at free surface boundary, a practical solution is applied to both methods while keeping their total accuracy. In addition, different solid boundary treatments are studied and their effect on total accuracy and stability of SPH methods are investigated.

Based on the results, both ISPH and WCSPH methods can model free surface profiles properly if a proper solid boundary treatment is utilized. Meanwhile, local surface fluctuations can be damped in both methods efficiently by means of the modified surface viscosity.

By means of original versions, it is concluded that ISPH method is generally more stable and more accurate particularly in modeling pressure field than WCSPH method. In addition, it is shown that ISPH method is faster than WCSPH method in solving a dam break flow with equal number of particles. On the other hand, ISPH in its original version using the divergence-free velocity scheme suffers from density loss problem. Since a lot of modifications have been introduced till now to overcome defections of both methods, it is not fair to compare methods with different modifications and therefore, similar modifications are applied in this study. Meanwhile, it can be concluded that each method is growing and is going its own way through enhancement.

1. Introduction

The Smoothed Particle Hydrodynamics (SPH) method is a particle method in Lagrangian coordinate that was originally introduced for the astrophysics by Monaghan (1992). Large deformations at free surface boundaries can be modeled efficiently by Lagrangian particle approaches and contrary to the Eulerian grid approaches, no numerical diffusion occurs in Lagrangian methods due to solving advection term directly. In addition, free surface profile can be easily traced via this method. At first, Weakly Compressible SPH (WCSPH) method applied to the fluid mechanics by Monaghan and Kos (1999) and later, Incompressible SPH (ISPH) method introduced by Shao and Lo (2003) based on a semi-implicit projection method. Gomez-Gesteira et al. (2010a) present the state-of-the-art of classical SPH for free surface flows and examined some improvement methods to classical SPH, especially for dam break problems. In WCSPH method, fluid is assumed compressible while incompressibility is ensured by means of pressure adjustment via equation of state. Lee et al. (2008) showed the efficiency of ISPH method particularly in improving the pressure field in comparison with WCSPH method. Later, several attempts have been made to improve the accuracy and functionality of ISPH method. Khayyer et al. (2008) revised the gradient of kernel function to improve the preservation of angular momentum. Xu et al. (2009) introduced a more stable method based on moving the

particles at the end of each time step through the streamlines and Rafiee et al. (2012) used modified Riemann solver to improve the accuracy of SPH methods.

To overcome unrealistic pressure oscillation in WCSPH methods, several attempts have been done such as density reinitializing, iteration or grid scheme methods (Monaghan 1989, Colagrossi and Landrini 2003, Fatehi and Manzari 2012, Violeau and Rogers 2016, Sun et al. 2017). However, this problem can be solved by means of ISPH method too.

Khayyer and Gotoh (2010b) modeled dam break flow using different modified forms of SPH, WCSPH and moving particle semi-implicit (MPS) methods. They concluded that the improved versions of these particle methods outperform the original versions in terms of both free surface profile and pressure field. According to their results, the WCSPH method modified using a moving least square (MLS) density re-initialization technique results in smoother pressure field than the modified MPS method. However, a distinctive disadvantage of WCSPH method in comparison with two other methods is that WCSPH methods need calibration constants. Khayyer and Gotoh (2010b) showed the importance of selecting a proper artificial viscosity in WCSPH methods. Later, Szewc et al. (2012) compared ISPH and WCSPH through simulating lid-driven cavity flow. They neglected the stability of pressure term and concluded that WCSPH needs more computational cost while density error accumulation occurs in the original forms of ISPH methods. However, the mentioned errors can be removed by means of relaxation coefficient or imposing additional viscosities (Lee et al. 2008, Xu et al. 2009, Asai et al. 2012, Akbari, 2017). Using higher orders Poisson Pressure Equation (PPE) or particle shifting can also improve the results of ISPH (Khayyer et al. 2017, Khayyer and Gotoh 2010a). Although ISPH method are concluded to be more efficient than WCSPH method in some of the studies (Lee et al. 2008, Lee et al. 2010, Gotoh and Khayyer, 2016), there is not yet a global agreement about this issue. Hughes and Graham (2010) by simulating dam break and wave impact on vertical wall concluded that in the optimum configuration, WCSPH could perform as well as ISPH and even in some respects better than ISPH. There is a similar conclusion in Shadloo et al.'s (2012) study where the accuracy of WCSPH method is mentioned as reliable as those of the ISPH and FEM. In addition, by comparing the numerical results with laboratory data corresponding to dam breaking flow, Lee et al. (2008) reported more unreliable fluctuations at the surface boundary in the case of utilizing ISPH method than WCSPH method. Meanwhile, Akbari (2017) introduced an efficient method that is applicable in both WCSPH and ISPH methods to control these unrealistic fluctuations at free surface profile. Gomez-Gesteira et al. (2010b) reported these ongoing debates among the SPH community about the different approaches to treat the compressibility of the fluid and proves that additional research should be conducted to elucidate the pros and cons of the different approaches.

In this study, performance of ISPH and WCSPH methods in modeling a well-known dam break flow is studied and it is tried to clarify the main reasons of different conclusions in literatures. In next sections, after presenting basic equations and numerical issues, different numerical concerns including accuracy, stability, boundary conditions and computational cost of both ISPH and WCSPH methods are investigated and reported separately. Then, the main outcomes are summarized in conclusion part.

2. Governing Equations and Numerical models

2.1. Governing Equations

The well-known continuity equations for fluids are:

$$\frac{1}{\rho_w}\frac{D\rho_w}{Dt} + \nabla.\vec{U}_f = 0 \quad (1)$$

$$\vec{\nabla}.\vec{U}_f = 0 \quad (2)$$

Where, ρ_w and $\vec{U}_f$ are density and velocity of the fluid, respectively. For a turbulent viscous flow, the Lagrangian format of momentum equation is:

$$\frac{D\vec{U}_f}{Dt} = \frac{-1}{\rho_w}\vec{\nabla}P + \upsilon_E\nabla^2\vec{U}_f + \vec{g} \quad (3)$$

Where, P and $\vec{g}$ represent total flow pressure and gravitational acceleration vector, respectively. Terms on the right hand side of Eq. (3) represents the pressure force caused by the pressure gradient, the viscous force and the gravitational acceleration, respectively. The effective viscosity $\upsilon_E = \upsilon_w + \upsilon_T$ is summation of fluid kinematic viscosity υ_w (1.0 E-6 for water) and Smagorinsky turbulent viscosity υ_T.

2.2. WCSPH and ISPH: Explicit and Semi-implicit methods

In WCSPH method, little compressibility is applied on the fluid via equation of state such as one proposed by Monaghan (1994) to calculate the pressure term:

$$P = \frac{\rho_w V_s^2}{7}\left(\left(\frac{\rho}{\rho_w}\right)^7 - 1\right) \quad (4)$$

Where ρ and ρ_w are computed and reference fluid density, respectively. V_s is the sound velocity normally taken as ten times the maximum fluid velocity as reported by Lee et al. 2008 to limit the density variation to one percent. Because of the large speed of the sound and implemented power coefficient in Eq. (4), a small fluctuation in the density generate a large pressure between two

adjacent particles and keep them away. Then, the particle velocity in the next time step (n+1) can be calculated explicitly based on the forces from the previous time step (n) i.e. F^n and the selected time step Δt as:

$$\vec{U}_f^{n+1} = \vec{U}_f^{n} + F^n.\Delta t;$$
$$F^n = \frac{-1}{\rho_w}\vec{\nabla}P^n + \upsilon_E \nabla^2 \vec{U}_f^{n} + \vec{g} \quad (5)$$

The predictor corrector time stepping method is applied in this study for WCSPH method.

On the other hand, in the ISPH method, fluid incompressibility is imposed by means of semi-implicit projection method as introduced by Shao and Lo (2003). Density invariant (DI) method and divergence-free velocity (DV) method are two main categories of the projection methods. Xu et al. (2009) reported that DV method is more accurate than DI method as utilized in this study. In this method, an intermediate velocity $\vec{U}_f^{*}$ is used and the momentum equation is written in two equations their summation generates the complete form of the momentum equation.

$$\frac{\vec{U}_f^{*} - \vec{U}_f^{n}}{\Delta t} = \upsilon_E \nabla^2 \vec{U}_f + \vec{g} \quad (6)$$

$$\frac{\vec{U}_f^{n+1} - \vec{U}_f^{*}}{\Delta t} = \frac{-1}{\rho_w}\vec{\nabla}P \quad (7)$$

By means of Eq. (6), intermediate velocity is obtained explicitly as:

$$\vec{U}_f^{*} = \vec{U}_f^{n} + \Delta t \times \left[\upsilon_E \nabla^2 \vec{U}_f + \vec{g}\right]^n \quad (8)$$

After Applying the divergence operator on both sides of Eq. (7) and considering a free divergence criterion ($\vec{\nabla}.\vec{U}_f^{n+1} = 0$), the unknown pressure term at the next time step (P^{n+1}) can be obtained by solving the obtained system of linear equations as:

$$\frac{\vec{\nabla}.\vec{U}_f^{*}}{\Delta t} = \vec{\nabla}.\left(\frac{1}{\rho_w}\vec{\nabla}P^{n+1}\right) \quad (9)$$

This system is solved in this study by means of the Preconditioned Bi-conjugate Gradient Stabilized Method with Jacobi pre-conditioner as an iterative method with the converged normalized residual as 0.01. Then, the particle velocity is obtained simply by:

$$\vec{U}_f^{n+1} = \vec{U}_f^{*} - \Delta t \times \left[\frac{1}{\rho_w}\vec{\nabla}P^{n+1}\right] \quad (10)$$

After computing the velocity of particles at the new time step (by means of WCSPH or ISPH), each particle moves to its new position ($\vec{r}^{n+1}$) by making use of the averaged velocity as:

$$\vec{r}^{n+1} = \vec{r}^{n} + \frac{(\vec{U}_f^{n+1} + \vec{U}_f^{n})}{2}\Delta t \quad (11)$$

2.3. SPH principles

In SPH method, each arbitrary function $f(x)$ is estimated at particle i by

$$f(x_i) = f_i \approx \sum_j f(x_j) W_{ij} V_j \; ; \; V_j = \frac{m_j}{\rho_j} \quad (12)$$

Where, j denotes neighboring particles and W_{ij} is the value of kernel function of particle i at the position of particle j. Supporting domain of each particle is a function of smoothing length (h) of the kernel function. Selection of smoothing length is important. Large values increase the computational cost and increase the smoothing effects on the results. On the other hand, small values of this parameter may results in numerical instabilities due to no interaction between two adjacent particles. In this study, the effect of this parameter is studied and its default value is selected as 1.2 times of particle spacing according to other studies (Shao 2010, Khayyer et al. 2008, Price 2012). In this study, cubic B-Spline kernel function with dominant error of $O(h^2)$ in integral interpolant is used as proposed by Monaghan (1992). In SPH methods, the computational domain is divided to several particles and each particle i represents a mass of m_i and occupies a volume of V_i. Density of the fluid at that particle is ρ_i and is obtained based on the concentration of its neighbor particles j by means of density summation method i.e.

$$\rho_i = \sum_j m_j W_{ij} \quad (13)$$

Or, by making use of density variation method which is based on the mass continuity equation in WCSPH method:

$$\frac{D\rho_i}{Dt} = \sum_{j \neq i} m_j (\vec{u}_{ij}.\vec{\nabla}_i W_{ij}) \quad (14)$$

In this equation, gradient of kernel function taken with respect to the particle i ($\vec{\nabla}_i W_{ij}$) is used and $\vec{u}_{ij} = \vec{U}_{fi} - \vec{U}_{fj}$ where $\vec{U}_{fi}$ and $\vec{U}_{fj}$ are particle velocities. Based on SPH algorithm, pressure gradient and velocity divergence is estimated as (Monaghan, 1992):

$$\vec{\nabla}P_i = \rho_i \sum_{j \neq i} m_j \left(\frac{p_i}{\rho_i^2} + \frac{p_j}{\rho_j^2}\right)\vec{\nabla}_i W_{ij} \quad (15)$$

$$\vec{\nabla}.\vec{U}_f^{*} = \sum_{j \neq i} V_j \left(\vec{U}_{fj}^{*} - \vec{U}_{fi}^{*}\right).\vec{\nabla}_i W_{ij} \quad (16)$$

Where $\vec{U}_{fi}^{*}$ and $\vec{U}_{fj}^{*}$ are intermediate velocities at particle i and j, respectively. Viscosity term can be estimated by combining the first derivative of SPH and FDM methods as discussed by Shao and Lo (2003):

$$\left(\upsilon_E \nabla^2 \vec{U}_f\right)_i = \sum_{j\neq i} m_j \frac{2(\upsilon_{Ei}+\upsilon_{Ej})}{\rho_i+\rho_j}.\frac{\vec{\nabla}_i W_{ij}.\vec{r}_{ij}}{\left|\vec{r}_{ij}\right|^2+\eta^2}\vec{u}_{ij} \quad (17)$$

In this equation, $\vec{r}_{ij}=\vec{r}_i-\vec{r}_j$ where $\vec{r}_i$ and $\vec{r}_j$ are the position vectors of the particles and $\eta=0.1h$ as proposed by Lee et al. (2008). υ_{Ei} and υ_{Ej} are effective viscosity of particle i and j, respectively. Similarly, the pressure gradient can be estimated as:

$$\vec{\nabla}.\left(\frac{1}{\rho_w}\vec{\nabla}P\right)_i = \sum_{j\neq i} m_j \frac{8}{\left(\rho_i+\rho_j\right)^2}.\frac{\vec{\nabla}_i W_{ij}.\vec{r}_{ij}}{\left|\vec{r}_{ij}\right|^2+\eta^2} p_{ij} \quad (18)$$

Where, $p_{ij}=P_i-P_j$. Eq. (18) is actually the discrete form of Eq.(9) and therefore, it is not applicable in WCSPH method where the pressure is obtained using the equation of state instead of solving the presented system of linear equations. On the other hand, angular momentum is not preserved in the common SPH method. However, this problem can be solved by correcting the kernel gradient via applying a corrective matrix $\widehat{L}_i$ as introduced by Bonet and Lok (1999). Khayyer et al. (2008) extended this improvement into SPH method and concluded that any linear velocity field gradient would be exactly evaluated via employment of the corrected kernel function as:

$$\tilde{\vec{\nabla}}_i W_{ij} = \left(\sum V_j \vec{\nabla}_i W_{ij} \otimes (\vec{r}_j-\vec{r}_i)\right)_i \vec{\nabla}_i W_{ij} \quad (19)$$

This correction factor is applied on the kernel gradient in this study for both WCSPH and ISPH methods to improve the accuracy of the equation discretization.

2.4. Tensile instability, artificial and surface viscosity

Tensile instability is one of the difficulties of the standard SPH where the particles attract each other and make unrealistic clumps when the fluid is compressed. Swegle et al. (1995) defined the criteria of this instability based on the negative pressure and the sign of the second derivative of the interpolating kernel. As a result, if distance between to pair particles gets closer than $2h/3$ in the case of using Cubic-Spline kernel function that is used in this study, these particles attract each other and perform a tensile instability. Dehnen and Aly (2012) reported less instability in the case of implementing Wendland kernel function. In addition, Monaghan (2000) suggested that the SPH tensile instability can be removed by implementing a small repulsive term between the SPH particles and this solution is used in this study for sensitivity analysis. He used a small artificial pressure even if the pressure was positive to remove the tendency of particles in forming the local linear structures.

Monaghan (1992) introduced artificial viscosity for making the SPH numerical model stable. He suggested replacing the artificial viscosity with the effective viscosity term in the momentum equation by the following definition:

$$\Pi_{ij} = \frac{-2\alpha_\Pi.C_s}{\rho_i+\rho_j}.\frac{h\vec{u}_{ij}.\vec{r}_{ij}}{\left|\vec{r}_{ij}\right|^2+\eta^2} \quad if: \vec{u}_{ij}.\vec{r}_{ij}<0 \quad (20)$$

Where α_Π is an empirical coefficient that is set to 0.1 in this study. If it is necessary to use artificial viscosity instead of effective viscosity, the viscosity term in the momentum equation should be considered as:

$$\Phi_{art} = -\sum_{j\neq i} m_j \Pi_{ij} \vec{\nabla}_i W_{ij} \quad (21)$$

Main drawback of this type of artificial viscosity is that utilizing improper coefficients can generate additional unrealistic damping throughout the whole flow domain. To limit the damping effect only to the surface boundary where the results of SPH method is not realistic due to the kernel truncation, a local surface viscosity is utilized in this study. The concept of surface viscosity was introduced by Xu (2010) and later, its workability was improved by the improvements suggested by Akbari (2017). In the modified surface viscosity method, the viscosity of surface particles is replaced with a modified viscosity as $\upsilon_m=\upsilon_E+\upsilon_{art-s}$ where the effective viscosity (υ_E) is the summation of laminar and turbulent viscosities and the surface artificial viscosity (υ_{art-s}) is defined as:

$$\upsilon_{art-s} = \alpha_s.(dr_0)^2 \frac{\left|\vec{U}_f\right|}{U_{\max}}.\left|\vec{\nabla}.\vec{U}_f\right| \quad (22)$$

dr_0 is the initial particle spacing and $U_{\max}$ is the absolute of the maximum particle velocities at each time step. α_s is a damping coefficient that controls the influence of the artificial viscosity and it is selected as unity as recommended by Akbari (2017). This type of surface viscosity is applicable in both ISPH and WCSPH methods and in contrast to the Xu (2010)'s approach, it can be used in variety of models with different accuracies and the damping coefficient has been defined via a rigorous method. For example, in an ideal model with a free divergence velocity condition, no excess viscosity is applied to the model.

In addition, the surface viscosity is a function of local inaccuracy and therefore, it varies from a particle to another one as a function of their local inaccuracies. The workability of this modified method in damping unrealistic fluctuation at free surface boundary is investigated in this study too. It was shown by Khayyer et al. (2008) that unrealistic surface fluctuation can be decreased by use of modified gradient kernel and particle surface tracking would be improved accordingly. This modification is also used in this study to conserve the angular momentum and its efficiency in damping surface fluctuations is also investigated.

2.5. Calculation time-step

CFL, mass force and viscous force are the three criteria used for calculating the time step that varies during the simulation as:

$$\Delta t = \min\left(\alpha_t \frac{\Delta x}{U_{\max}}; \alpha_t \sqrt{\frac{h}{f_a}}; \alpha_t \frac{h}{U_{\max} + \beta_{visc} h}\right); \quad \beta_{visc} = \frac{\vec{u}_{ij}.\vec{r}_{ij}}{\left|\vec{r}_{ij}\right|^2 + \eta^2} \tag{23}$$

f_a is the force per unit mass of the fluid that is equal to the minimum magnitude of particle accelerations and α_t is set to 0.1 in our numerical models. $U_{\max}$ is maximum velocity of particles in ISPH method and celerity of sound (numerically 10 times the maximum velocity) in WCSPH method.

2.6. Free surface boundary

SPH integration is not accurate at the free surface boundary because the kernel function is truncated at this boundary. As a result, predicted density of surface particles via Eq. (13) is less than the actual water density. This shortcoming is utilized at each time step to detect particles located at free surface boundary. In other words, a particle i is located at the free surface boundary if its predicted density fulfills (Shao and Lo 2003):

$$\rho_i < \beta_{surf} \rho_w; \ \beta_{surf} \cong 0.9 \tag{24}$$

After recognizing the surface particles, their pressure set to zero. In addition, a surface viscosity as introduced in Eq. (22) is applied to the surface particles to diminish any unreliable fluctuation.

2.7. Solid boundary

Different methods have been introduced for modeling solid boundary particles and several attempts have been done to make these methods more accurate. Generally, one line of fixed particles is used to model a solid boundary condition and to make density of these particles different from the truncated density of surface particles; several lines of dummy particles are also applied parallel to the main solid boundary line to remedy the truncation error. Ferrari et al. (2009) combined different methods to get more reliable results near the wall boundary and Ferrand et al. (2012) improved modeling of solid boundaries by normalizing density of particles near this boundary. Several other methods have been introduced too; however, all of these methods can be categorized in three general groups as repulsive force methods (Monaghan 1994), fixed dummy particle methods (Shao and Lo 2003) and mirror particle methods (Colagrossi and Landrini 2003). In the first method, a repulsive force exerts on those fluid particles getting close to the solid boundary. In the second method, governing equations are solved for solid boundary particles as well as fluid particles and therefore, internal pressure will be increased when fluid particles get close to the boundary particles and prevent them from penetrating into the solid boundary. Boundary particles are fixed in this method and the pressure of outer dummy particles is set equal to the pressure of nearest wall particle to impose the homogenous Neumann boundary condition. The last method is based on considering mirror particles outside the solid boundary while their parameters are equal to the mirrored parameters of fluid particles closing to the solid boundary. Therefore, when a particle gets close to a solid boundary, it will sense its mirrored particle and pressure will be increased accordingly. Consequently, this method is comparable with the second method because the pressure term is modified by means of solving governing equations instead of imposing extra repulsive force. Therefore, the accuracy of repulsive force method in comparison with artificial particle method is investigated in this study.

Following Monaghan (1994), when distance between fluid particle and solid boundary particle get less than a defined value of r_b, in repulsive force method, an extra force (F_{ij}^R) exerts on the pair particle as:

$$\vec{F}_{ij}^R = D\left[\left(r_b / \left|\vec{r}_{ij}\right|\right)^{n1} - \left(r_b / \left|\vec{r}_{ij}\right|\right)^{n2}\right]\frac{\vec{r}_{ij}}{\left|\vec{r}_{ij}\right|} \quad ; \left|\vec{r}_{ij}\right| < r_b \tag{25}$$

Where, $n1$ and $n2$ are empirical coefficients that are suggested by Monaghan (1994) as 12.0 and 4.0, respectively and D is an empirical parameter that depends on the considered case for simulation.

3. Accuracy of WCSPH and ISPH methods

Well-known dam break flow is selected to study the performance of WCSPH and ISPH methods in modeling free surface flows. Accuracy of simulated surface profile and pressure term are investigated and the effects of different terms are discussed. Following Akbari (2017), the geometry of the problem is selected as indicated in Fig.1. The bed is wet with

depth of 0.02m and height and width of the initial water column are 0.25m and 0.28m, respectively. Total number of particles is 3280 with initial spacing as 0.005 and the total simulation time is selected as 3.2s. The simulations have been carried out on a Core2 Duo CPU T7500, 2.13 GHz and RAM 2.0 GB Laptop.

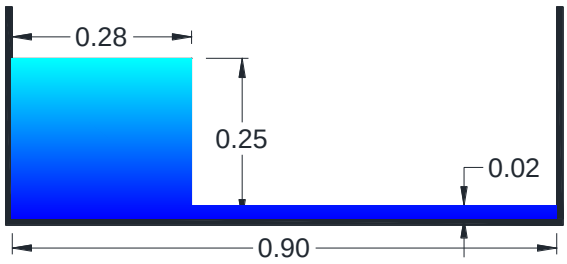

Figure 1. Initial geometry for dam break simulation

The density summation method as Eq. (13) have been used and the simulated results at t=0.3s are shown in Fig. 2 for WCSPH with artificial viscosity as Eq. (21) and ISPH methods with artificial viscosity and modified surface viscosity as Eq. (21) and Eq. (22), respectively. Solid line shows the free surface profile modeled with WCSPH method. As shown in Fig. 2(a) and Fig. 2(b), the simulated surface profiles are nearly similar in both WCSPH and ISPH methods with artificial viscosity. Yet, the pressure fluctuation in WCSPH method is significantly more than fluctuation in ISPH method. For example, time series of the simulated pressures at a point on the tank floor (red point in Fig.2 at x=0.4m,z=0.0) are depicted in Fig. 3. Although both methods have resulted in nearly same averaged values, high fluctuations are generated in WCSPH method. Since equation of state is used to calculate the pressures of each individual particle in WCSPH method, a little inaccuracy in particle density can generate a significant local error in the pressure term. Actually imposing incompressibility in WCSPH done via pressure adjustment and during this procedure pressure accuracy sacrifices. On the other hand, a system of linear equations is solved in ISPH method to calculate the pressure and therefore, the fluctuations in ISPH results are less accordingly. It should be noted that the theoretical background of ISPH in deriving the incompressible equations is more robust than empirically introduced equation of state in WCSPH method. However, a divergence-free velocity ISPH method is implemented in this study that can suffer from conserving continuity equation during the simulation.

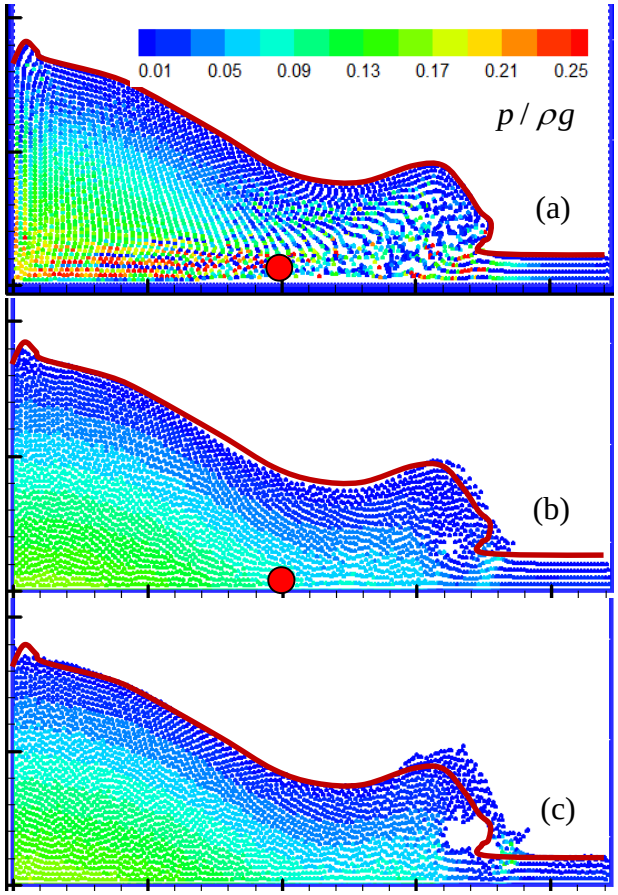

Figure 2. Simulated pressure at t=0.3s: a:up)WCSPH with artificial viscosity; b:middle) ISPH with artificial viscosity; c:down) ISPH with effective viscosity; (Solid line shows the surface profile in "a"), results are compatible with Akbari (2017)

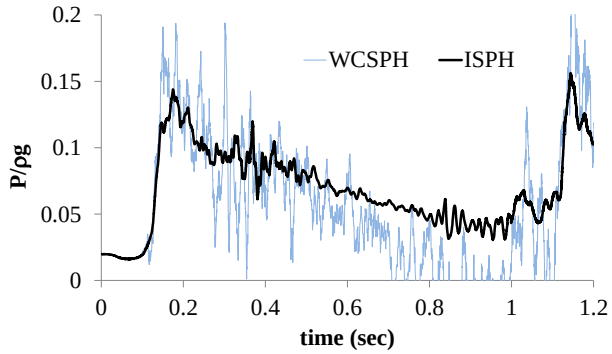

Figure 3. Time series of the simulated pressures (at x=0.4m, z=0.0m) using WCSPH and ISPH with the same artificial viscosity

To further investigate the results, density conservation during the simulations are calculated and the error in the mean values (averaged density of all particles at each time step) are presented in Fig. 4 for both methods. It can be seen that the utilized WCSPH method is more accurate in conserving mass during the simulation than the utilized ISPH. The maximum errors in the mean density in WCSPH and ISPH methods are nearly 2% and -3%, respectively. It should be noted that local density fluctuations exist yet in WCSPH method; however variation of the mean density is smoother due to averaging between all particles. In other words, although density (and

consequently pressure) fluctuation at each particle is more in WCSPH than in ISPH, the total mass conservation is better satisfied in WCSPH model.

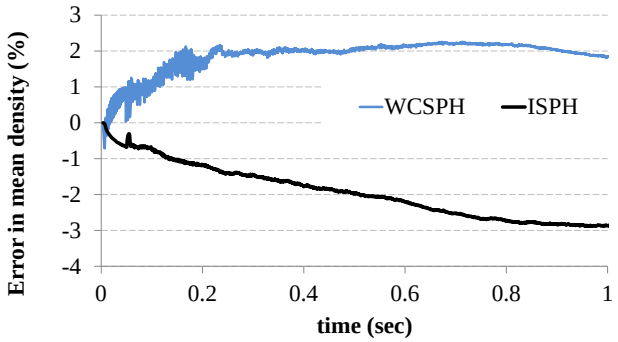

Figure 4. Error in the mean density using WCSPH and ISPH with the same artificial viscosity

As discussed by Szewc et al., (2012), mechanism of the density error in ISPH and WCSPH methods is completely different. Using an equation of state in WCSPH method generates local errors, while movement of particles with a velocity projected onto a divergence-free space with no constraint on density variation causes accumulated density errors in ISPH method. Therefore, the error of WCSPH in Fig.4 has reached to a stable point earlier than ISPH method. This drawback of ISPH can be corrected using a density invariant scheme, yet suffering from errors in velocity divergence field. Some improvements such as combining these two schemes (Xu et al., 2009) or using higher order source terms in equations (Gotoh et al., 2014) were introduced to overcome these problems of ISPH method. On the other hand, some improvements such as normalizing particle densities or using a smoothed density (Hughes and Graham, 2010) were introduced to overcome the problem of local variations in WCSPH method. There are also other modifications such as particle shifting or density normalization applicable to both methods to improve density conservation during the simulation. Since a lot of modifications have been introduced to improve ISPH and WCSPH methods, models with a similar condition are utilized in this study for making a fair comparison.

4. Stability of WCSPH and ISPH methods

Although ISPH method is shown to be more robust and more accurate than WCSPH method particularly in simulating pressure term, using a global artificial viscosity can damp the real flows as a result of the utilized artificial viscosity (α_Π). As mentioned before, artificial viscosity is used to stabilize the numerical solution. However, high artificial viscosity will generate unrealistic damping and inadequate empirical coefficient may affect the model accuracy (even in predicting surface profile). The importance of selecting an appropriate artificial viscosity in modeling dam break flows has been studied by Khayyer and Gotoh (2010b). Although the empirical coefficient (α_Π) can be calibrated via experimental studies, laboratory data are not always available and therefore, the better solution is implementing effective viscosity instead of artificial viscosity. Considering effective viscosity, simulated pressure pattern by means of ISPH method is shown in Fig. 2(c). By comparing Fig. 2(b) with Fig. 2(c), it is clear that a sharp wave profile can be modeled more clearly by means of implementing effective viscosity rather than artificial viscosity. On the other hand, by comparing the free surface profiles, it can be concluded that an extra damping has been occurred in the case of using artificial viscosity.

In addition to the additional viscosities, the smoothing length in kernel function can affect the results and control the numerical stability of the methods. If higher (doubled) smoothing length as $h = 2.4dr_0$ is taken into account instead of $h = 1.2dr_0$, surface profile will not be as smooth as before because more particles may stick together as a result of tensile instability problem. Particle clustering during wave breaking is shown in Fig. 5(b) while there will be no problem if less smoothing less is used in simulation as Fig. 5(a). A part of the wave profile is presented in higher resolution in this figure to clarify particle clustering. Actually, when particles get closer than a specific distance (i.e. $2h/3$ in the case of using Cubic-Spline kernel), they will affected by tensile instability problem and if higher smoothing length is utilized more particles may be surrounded making the results inaccurate while the simulation is still stable. However, the WCSPH method is not stable and the simulation diverges as presented in Fig. 6(a) if effective viscosity is used without any stabilization technique. As shown in this figure, in addition to solution divergence, tensile instability is performed even by means of $h = 1.2dr_0$ and some particles are moving as a collocation surrounded inside the kernel function. This instability does not happen in ISPH method, however, if higher smoothing length is used, more particles may stick together and make even ISPH solution unstable. Although this problem can be solved by means of tensile correction technique, WCSPH method is unstable yet because of effective viscosity as shown in Fig. 6(b). This means that particle collocation due to tensile instability can be removed by decreasing the smoothing length in both ISPH and WCSPH methods, however, WCSPH can be yet unstable and there is a need to use artificial viscosities for making this method stable. On the other hand, decreasing the smoothing length is limited and inadequate reduction can lead to insufficient contribution of neighbor particles than will results finally in divergence problems during the solution.

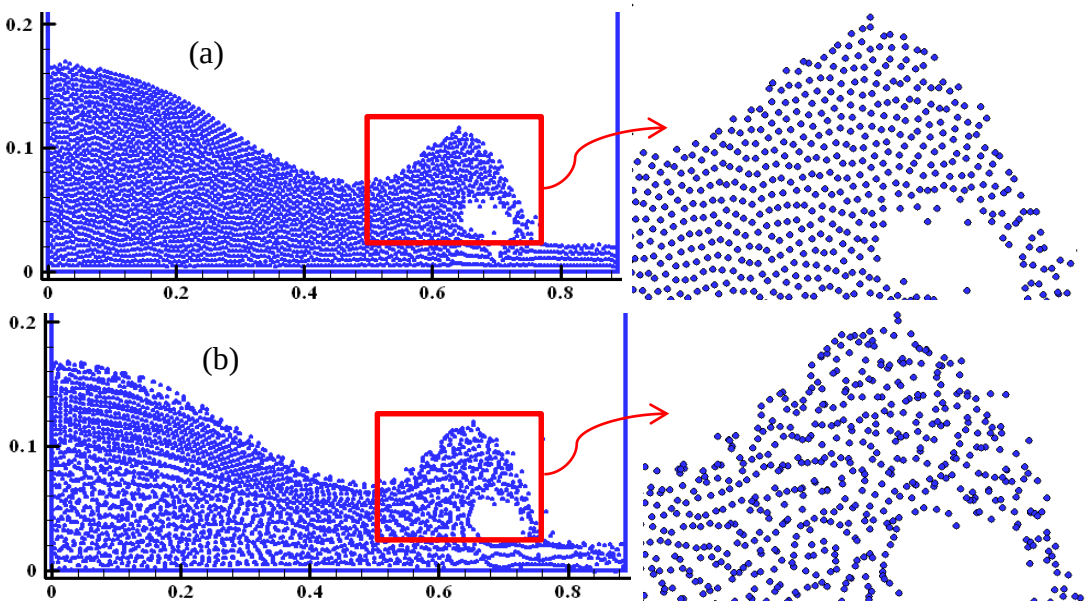

Figure 5. Particles during simulated wave breaking by ISPH method and effective viscosity at t=0.3s; a:up) $h = 1.2dr_0$ **; b:down)** $h = 2.4dr_0$

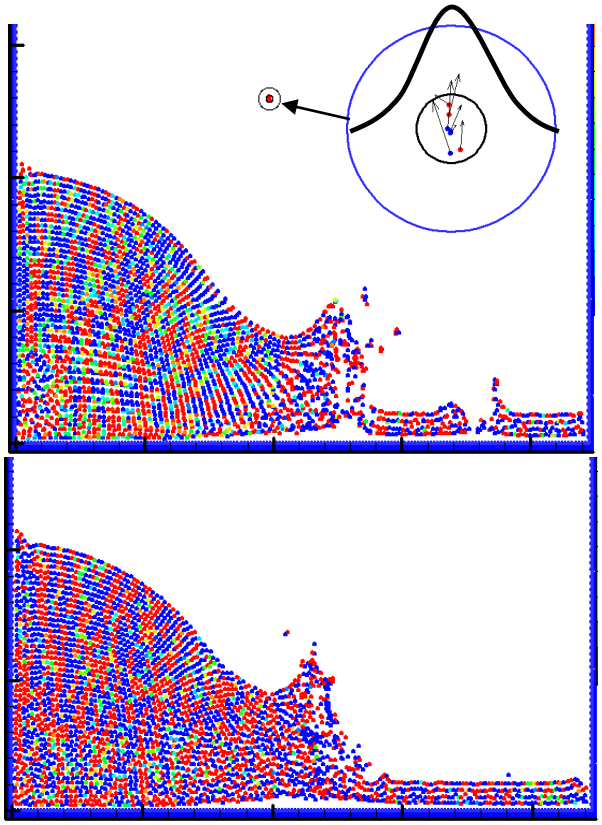

Figure 6. Simulated pressure by WCSPH method and effective viscosity at t=0.2s; a:up) without tensile correction; b:down) with tensile correction

5. Surface boundary and local fluctuations

According to the results, ISPH method is more stable than WCSPH method and it is also more reliable particularly in predicting pressure term. However, unreliable surface fluctuation may occur even in ISPH method. Although this problem can be solved by means of artificial viscosity as introduced by Monaghan (1992), accuracy of the results will be decreased by artificial viscosity as declared before. An effective method in controlling unreliable surface fluctuation is implementing additional surface viscosity as introduced by Akbari (2017) via Eq. (22). The effect of imposing surface viscosity in reducing particle jumps near free surface boundary is presented in Fig. 7.

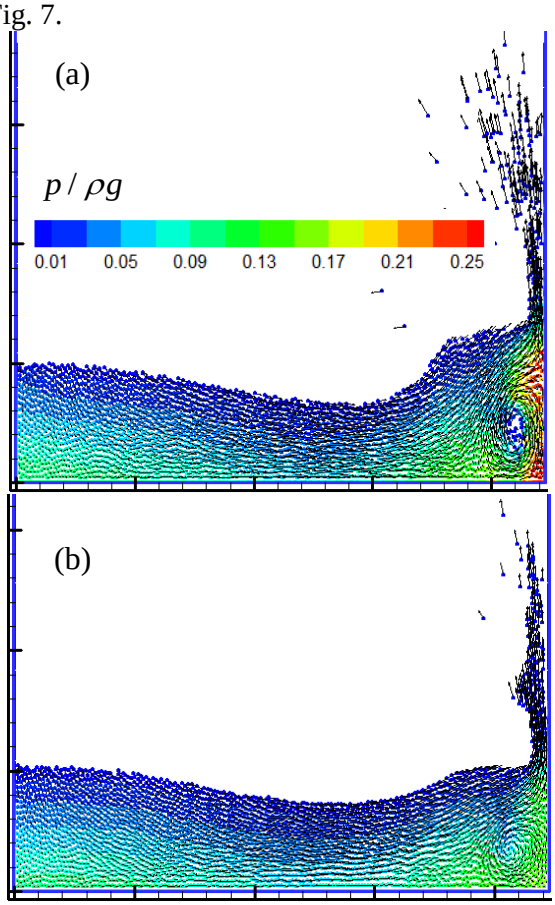

Figure 7. Simulated dame break flow by ISPH method at t=0.5s; a:up) non-viscous; b:down) modified surface viscosity

As shown in Fig. 7(a), if no viscosity is applied to the fluid, particles will move in a disordered condition particularly near the surface profile. However, these movements are controlled by means of imposing surface viscosity as indicated in Fig. 7(b) and a smoother surface profile has been modeled. It should be noted that utilizing very large damping coefficient can yet results in a global damping similar to the effect of imposing traditional artificial viscosities.

Khayyer et al. (2008) showed that unrealistic surface fluctuation could be decreased by means of modified gradient of kernel function. This modification is considered in this study because angular momentum is preserved by this modification. However, its efficiency in smoothing the surface profile should be studied more in comparison with the surface viscosity. Pressure contours in addition to surface particles are presented in Fig. 8 during wave breaking at t=0.3s.

As shown in Fig. 8(a), wave profile is straggly if neither kernel gradient modification nor surface viscosity is used and this uneven behavior will not be solved by use of kernel gradient modification as presented n Fig. 8(b). However, as shown in Fig. 8(c), a smooth wave profile can be simulated by means of surface viscosity even if no kernel modification is utilized.

In addition, if both modified kernel gradient and surface viscosity are used, simulated wave profile will be smooth and no fluctuation will be seen in the surface profile according to Fig. 8(d). Both of these modifications shall be used in numerical modeling because surface fluctuation can be efficiently removed by means of the surface viscosity while angular momentum can be preserved via modified gradient of kernel function. Although unreliable surface fluctuation may be decreased by utilizing modified kernel gradient, the effect of the surface viscosity in controlling the surface profile is clearly more significant and the model accuracy will be conserved by this modification. It should be noted that a general damping effect can be generated by means of imposing an artificial viscosity (as was indicated in Fig. 2(b)), however, no general damping has been occurred in the case of using surface viscosity (as indicated in all the cases in Fig. 8).

It can be concluded that by means of surface viscosity, surface fluctuation will be damped and there is no need to use stabilizing methods such as artificial viscosity.

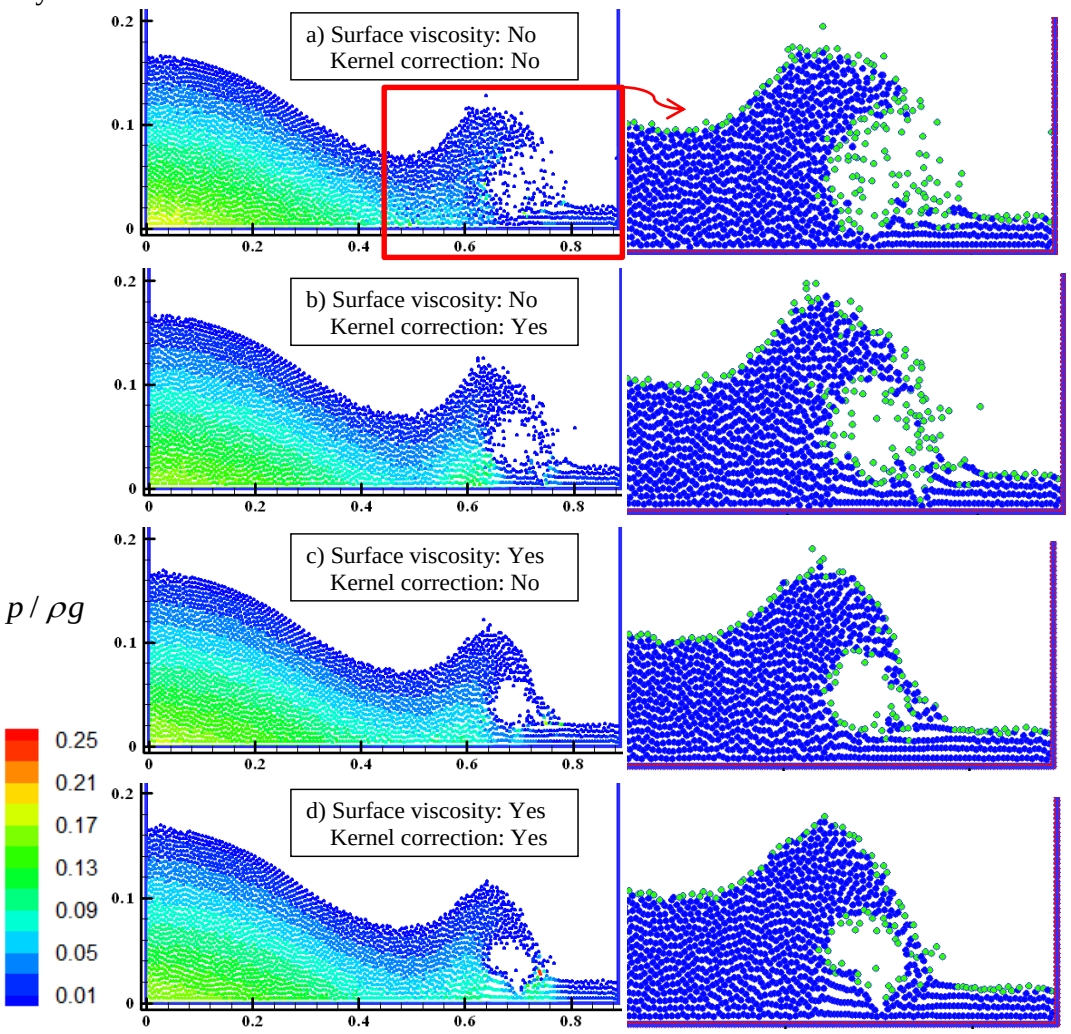

Figure 8. Simulated dame break flow by ISPH method with effective viscosity at t=0.3s; a) Without any modification; b) modified kernel; c) modified surface viscosity; d) modified kernel and surface viscosity

6. Solid boundary treatments

Both repulsive boundary and dummy boundary methods are used in this study to simulate dam break flow (fluid dam with 0.2m height and 0.1m width in a box with 0.3m length) by means of both WCSPH and ISPH methods. Initial particle spacing is set to 0.005m and the results of simulation by making use of dummy particle method are shown in Fig. 9 at t=0.3s. In this figure, ISPH result is shown with two WCSPH results based on density summation and density variation methods as Eq. (13) and Eq. (14). Similar to simulated dam break flow in the previous section, surface profile is nearly alike in the results of both ISPH and WCSPH method based on density summation method but, density variation method is not an accurate as density summation method in predicting particle positions and as shown in Fig. 9(c), particles are not uniformly distributed in the fluid domain that shows incompressibility criteria will not be satisfied completely if density summation method is used. However, dummy particle method can be utilized efficiently in modeling solid boundary both in WCSPH and ISPH methods and there is no particle penetration into solid boundary by means of this method.

Contrary to dummy particle method, there are some empirical parameters in the repulsive boundary method. The force coefficient (D) and covered distance (r_b) are two important parameters that influence on the amount of repulsive force and define those fluid particles that the repulsive force should be exerted on. To study the efficiency of the repulsive force method, different simulation results for dam break flow is shown in Fig. 10 by considering different empirical parameters and utilizing WCSPH method. As shown before, solid boundary can be simulated properly by dummy particle method in WCSPH method that is however less accurate than ISPH method. In Fig. 10(a), empirical coefficients are set in a way to have no particle penetration to solid boundary (i.e. $r_b = 1.2dr_0$, $D = 4E-4$). If small distance is used (i.e. $r_b = 0.001$), fluid particles will not affected by the repulsive force at a proper time because they are too close to the boundary when they receive the repulsive force and fluid particles will penetrate into solid boundary accordingly as shown in Fig. 10(b). In addition, if repulsive force does not properly set fluid particles will pass through the solid boundary as shown in Fig. 10(c). In this figure, considered repulsive force is less than what is required for preventing particles from penetrating into boundary. On the other hand, if large repulsive force is taken into account, extra force will be exerted on the fluid particles make particles reflecting back from the boundary with an unreliable velocity. Therefore, the efficiency of the repulsive boundary method depends on its empirical coefficients and unrealistic results may be obtained by means of utilizing inadequate parameters. However, this difficulty does not happen in dummy particle method because actual fluid pressure is used to satisfy boundary condition.

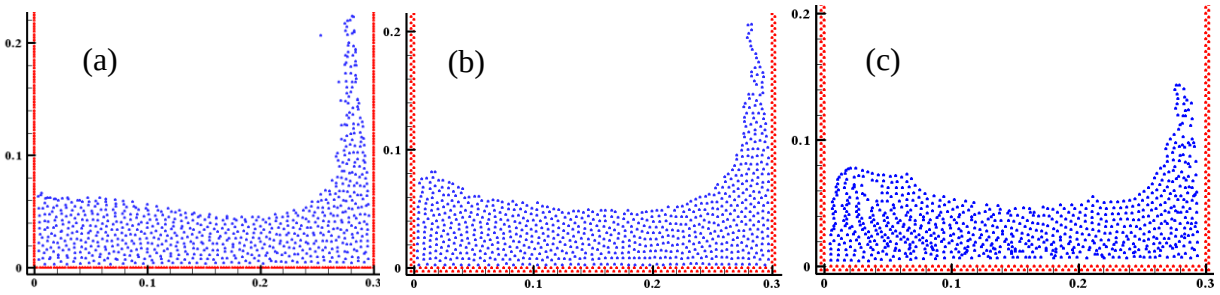

Figure 9. Simulated dam break at t=0.3s with dummy particle method;
a:left) ISPH; b:middle) WCSPH with density summation, c:right) WCSPH with density variation

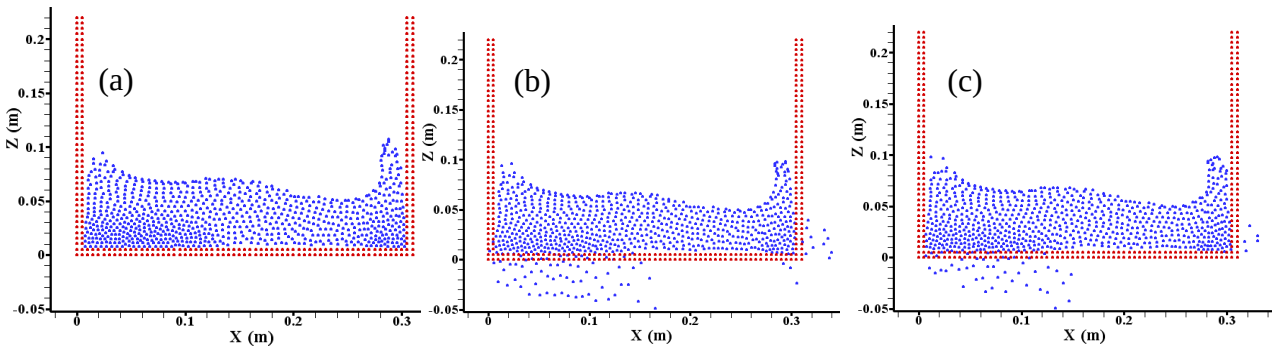

Figure 10. Simulated dam break at t=0.3s with repulsive method;
a:left) (rb=1.2dr0, D=4E-4); b:middle) small distance: (rb=0.001, D=4E-4); c:right) small repulsive force: (rb=1.2dr0, D=4E-6)

7. Computational cost of ISPH vs. WCSPH

Computational times of ISPH and WCSPH methods are compared in modeling the dam break flow with initial condition in Fig. 1. Different special resolutions are also selected to study the computational cost of SPH methods versus number of particles. All the simulations have been performed on a Core2 Duo CPU T7500, 2.13 GHz and RAM 2.0 GB Laptop.

The required CPU times for different cases are presented in Table 1 and Fig. 11. As shown in this figure, ISPH method is more computationally efficient than WCSPH for all of these cases. It should be noted that similar search algorithm (i.e. linked list method) is used for searching neighbor particles and a similar time step based on Eq. (23) is implemented. According to the transient behavior of the flow, maximum flow velocities and consequently minimum time steps change continuously during simulations. According to the time step criteria defined in Eq. (23), minimum time step will be decreased if higher velocity is observed in the simulation. For calculating the time step, speed of sound is taken into account in WCSPH method while maximum flow velocity is used in ISPH method. Therefore, time step is less in WCSPH method than in ISPH method.

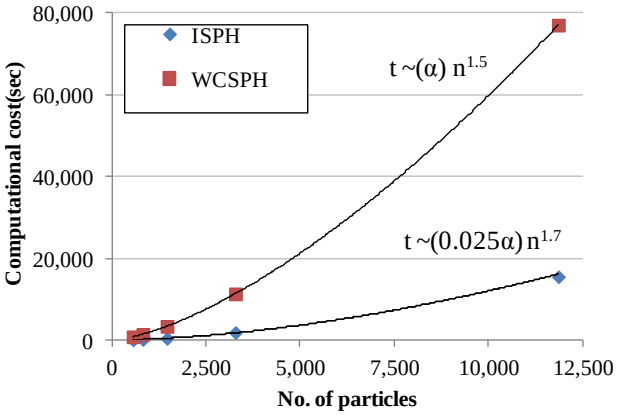

Figure 11. Computational cost of ISPH and WCSPH in simulating dam break flow

Total computational cost depends on both time step increment and computational cost per time step. Time step increment is related to flow behavior as defined in Eq. (23) while computational cost per time step is related to the implemented algorithm as well as efficient programming. According to Table 1, averaged time step in simulating the case II by ISPH method is approximately eleven times more than required time step in WCSPH, however, ISPH method is only six times faster than WCSPH method (11322/1867). The main reason is more computational cost per time step in ISPH method that is due to solving a system of linear equations in ISPH method. In other words, for the mentioned case (case II), computational cost per time step in ISPH method should be nearly two times (i.e. 11/6) more than what is in WCSPH method to decrease the total ratio of CPU time from eleven to six. Time step can be calculated simply, yet researchers might consider various algorithms that influence on the computational cost per time step. In addition, ratio of the required computational cost of ISPH and WCSPH is a function of the number of particles. Although ISPH is generally faster than WCSPH, the efficiency ratio is less for larger number of particles. For example, in case I with larger number of particles, ISPH is 5 times faster than WCSPH while in case II it is 6 time faster. Since WCSPH programming is simpler than ISPH and most of its programming techniques exist in ISPH method too, it can be concluded that the most important issue in comparing computational cost of ISPH method against WCSPH method is the utilized technique in developed ISPH model. The main distinguishing item in ISPH method is solving linear equations that are not performed in WCSPH method. Since dimension of this linear system is equal to the square of particle numbers (i.e. $n_p \times n_p$), computational cost of ISPH method would be more sensitive to the number of particles in comparison with WCSPH method. As shown in Fig. 11, ISPH computational cost is proportional to $n_p^{1.7}$ while the power of particle numbers is 1.5 (instead of 1.7) in case of WCSPH method. Therefore, in case of utilizing very large number of particles, WCSPH method can become more efficient than an ISPH method that works with a sensitive solver to the number of particles. In addition, parallel programming, as a good solution for solving large number of particles, can be applied simpler to

Table 1. Computational cost of ISPH and WCSPH in simulating dam break flow

Case	dx0	No. of particles	Computational cost (s)			Averaged time step (s)		
			ISPH	WCSPH	WCSPH/ISPH	ISPH	WCSPH	ISPH/WCSPH
I	0.0025	11861	15520	77102	4.97	1.80E-04	1.60E-05	11.25
II	0.005	3280	1867	11322	6.06	3.80E-04	3.40E-05	11.18
III	0.0075	1461	418	3372	8.07	7.30E-04	5.20E-05	14.04
IV	0.01	820	165	1422	8.62	9.50E-04	7.20E-05	13.19
V	0.012	560	77	810	10.52	1.30E-03	8.30E-05	15.66

WCSPH than to ISPH.

The results show that the utilized ISPH is faster than WCSPH method in solving common dam break flows. This is compatible with the results of some previous studies such as Lee et al. (2008) and Lee et al. (2010) that have reported a shorter CPU time for ISPH than WCSPH in the order of (2 to 20) times. However, these values depend on the utilized programming techniques as well as the number of particles. This is why different researchers have reported dissimilar computational costs for ISPH versus WCSPH method.

8. Conclusions

The accuracy, stability and efficiency of both WCSPH and ISPH methods are compared in this paper by means of simulating dam break flow. In addition, modeling of free surface and solid boundaries are studied to introduce an effective technique in modeling boundaries. Computational costs of these methods are then compared in solving a similar problem. It should be emphasized that each method has its individual advantage and drawbacks and a lot of modifications have been introduced to amend drawbacks. Meanwhile, original forms or similar modifications are taken into account in this study to get fair comparison results and discover intrinsic drawbacks. Based on the results:

a) Simulated free surface profile is nearly similar in both ISPH and WCSPH methods. However, simulated pressure is not accurate in WCSPH method while no unrealistic pressure fluctuation occurs in ISPH method.

b) Unrealistic fluctuation of surface particles can be removed by means of the surface viscosity while keeping the model accuracy. In simulated cases, the effect of surface viscosity in smoothing surface profile is more significant than modifying the gradient of kernel function.

The results of WCSPH method are more accurate in case of utilizing density summation method in comparison with utilizing density variation method. Although density fluctuation at each particle is more sensible in WCSPH than in ISPH method, the total mass continuity is better satisfied in original form of WCSPH method than in original form of ISPH method written based on divergence-free velocity scheme.

c) Dummy and mirror particle methods are more accurate than repulsive force method in modeling solid boundaries.

d) ISPH method is generally more stable than WCSPH method. Although artificial viscosity can be used to stabilize WCSPH method, the model accuracy will be decreased in this situation.

e) Both models will be unstable in case of utilizing small smoothing length because of insufficient number of interaction particles; however, tensile instability may occur in addition to unreliable smoothing effect if improper large smoothing length is utilized. Therefore, smoothing length is proposed as 1.2 times of the initial particle spacing.

f) Time step and computational cost per time step are two important items in total efficiency of models. Although WCSPH is more efficient than ISPH in solving each time step (nearly twice faster in the modeled cases in this study), bigger time steps (nearly ten times based on the maximum particle velocities versus sound velocity) can be used in ISPH method. Computational cost per time step depends on the number of particles as well as the utilized solver in ISPH method. According to the simulated cases in this study, ISPH is nearly five times faster than WCSPH method, however, this conclusion would be different in case of using other solvers.

g) In comparison with WCSPH method, the computational cost of ISPH method is more sensitive to the number of particles because a system of linear equations should be solved in each step of the solution that is an important item in ISPH efficiency.

It should be noted that

Meanwhile

9. References

1- Akbari, H., (2017). *Simulation of wave overtopping using an improved SPH method*. Coastal Engineering. 126, 51–68.

2- Asai, M., Aly, A.M., Sonoda, Y., Sakai, Y. (2012). *A stabilized incompressible SPH method by relaxing the density invariant condition*. Journal of Applied Mathematics. 2012, 24 pages.

3- Bonet, J., Lok, T.S. (1999). *Variational and momentum preservation aspects of smooth particle hydrodynamic formulation*. Computer Methods in Applied Mechanics and Engineering. 180, 97–115.

4- Colagrossi, A., Landrini, M. (2003). *Numerical simulation of interfacial flows by smoothed particle hydrodynamics*. Journal of Computational Physics. 191(2), 448 -475.

5- Dehnen W., Aly H. (2012), *Improving convergence in smoothed particle hydrodynamics simulations without pairing instability*. Monthly Notices of the Royal Astronomical Society. 000, 1-15.

6- Fatehi, R., Manzari, M.T. (2012). *A consistent and fast weakly compressible smoothed particle hydrodynamics with a new wall boundary condition.* International Journal for Numerical Methods in Fluids. 68, 905–921.

7- Ferrari, A., Dumbser M., Toro E. F., Armanini A. (2009). *A new 3D parallel SPH scheme for free surface flows*. Computers & Fluids. 38, 1203–1217.

8- Ferrand, M., Laurence, D., Rogers, B., Violeau, D., Kassiotis, C. (2012), *Unified semi-analytical wall boundary conditions for inviscid, laminar or turbulent flows in the meshless SPH*

method. International Journal for Numerical Methods in Fluids. 71(4), 446–472.

9- Gomez-Gesteira, M., Rogers, B.D., Dalrymple, R.A., Crespo, A.J.C. (2010a). *State-of-the-art of classical SPH for free-surface flows.* Journal of Hydraulic Research. 48(Extra Issue), 6-27.

10- Gomez-Gesteira, M., Rogers, B.D., Violeau, D., Grassa, J.M., Crespo, A.J.C. (2010b). *Foreword: SPH for free-surface flows.* Journal of Hydraulic Research. 48(Extra Issue), 3-5.

11- Gotoh, H., Khayyer, A., Ikari, H., Arikawa, T., Shimosako, K. (2014). *On enhancement of Incompressible SPH method for simulation of violent sloshing flows*, Applied Ocean Research. 46, 104-115.

12- Gotoh, H., Khayyer, A. (2016). *Current achievements and future perspectives for projection-based particle methods with applications in ocean engineering.* J. Ocean Eng. Mar. Energy 2(3), 251–278.

13- Hughes, J.P., Graham, D.I. (2010). *Comparison of incompressible and weakly-compressible SPH models for free-surface water flows.* Journal of Hydraulic Research. 48, 105-117.

14- Khayyer, A., Gotoh, H., Shao, S.D. (2008). *Corrected Incompressible SPH method for accurate water-surface tracking in breaking waves.* Coastal Engineering. 55, 236–250.

15- Khayyer, A., Gotoh, H., 2010a. *A higher order Laplacian model for enhancement and stabilization of pressure calculation by the MPS method.* Appl. Ocean. Res. 32(1), 124–131.

16- Khayyer, A., Gotoh, H., 2010b. *On particle-based simulation of a dam break over a wet bed*. Journal of Hydraulic Research. 48(2), 238–249.

17- Khayyer, A., Gotoh, H., Shimizu, Y., 2017. *Comparative study on accuracy and conservation properties of two particle regularization schemes and proposal of an optimized particle shifting scheme in ISPH context.* Journal of Computational Physics. 332, 236–256.

18- Lee, E.S., Moulinec, C., Xu, R., Violeau, D., Laurence, D., Stansby, P. (2008). *Comparisons of weakly compressible and truly incompressible algorithms for the SPH mesh free particle method.* Journal of Computational Physics. 227, 8417–8436.

19- Lee, E.S., Violeau, D., Issa, R., Ploix, S. (2010). *Application of weakly compressible and truly incompressible SPH to 3-D water collapse in waterworks.* Journal of Hydraulic Research. 48, 50-60.

20- Monaghan, J.J. (1989). *On the problem of penetration in particle methods.* Journal of Computational Physics. 82(1), 1–15.

21- Monaghan, J.J. (1992). *Smoothed particle hydrodynamics.* Annual Review of Astronomy and Astrophysics. 30, 543–574.

22- Monaghan, J.J. (1994). *Simulating free surface flows with SPH.* Journal of Computational Physics. 110 (2), 399-406.

23- Monaghan, J.J., Kos, A. (1999). *Solitary waves on a Cretan beach.* Journal of Waterway, Port, Coastal, and Ocean Engineering (ASCE). 125, 145–154.

24- Monaghan, J.J. (2000). *SPH without a Tensile Instability.* Journal of Computational Physics. 159, 290–311.

25- Price, D.J. (2012). *Smoothed particle hydrodynamics and magnetohydrodynamics.* Journal of Computational Physics. 231(3), 759–794.

26- Rafiee, A., Cummins, Sh., Rudman, M., Thiagarajan, K. (2012). *Comparative study on the accuracy and stability of SPH schemes in simulating energetic free-surface flows.* European Journal of Mechanics - B/Fluids. 36, 1–16.

27- Shadloo, M.S., Zainali, A., Yildiz, M., Suleman, A. (2012). *A robust weakly compressible SPH method and its comparison with an incompressible SPH.* International Journal for Numerical Methods in Engineering. 89, 939–956.

28- Shao, S.D., Lo, E.Y.M. (2003). *Incompressible SPH method for simulating Newtonian and non-Newtonian flows with a free surface.* Advances in Water Resources. 26, 787–800.

29- Shao, S.D. (2010). *Incompressible SPH flow model for wave interactions over porous media.* Coastal Engineering. 57, 304–316.

30- Sun, P.N., Colagrossi, A., Marrone, S., Zhang, A.M., 2017. *The δplus-SPH model: Simple procedures for a further improvement of the SPH scheme.* Comput. Meth. Appl. Mech. Eng. 315, 25–49.

31- Swegle, J., Hicks, D.L., Attaway, S.W. (1995). *Smoothed Particle Hydrodynamics stability analysis.* Journal of Computational Physics. 116, 123-134.

32- Szewc, K., Pozorski, J., Minier, J-P. (2012). *Analysis of the incompressibility constraint in the smoothed particle hydrodynamics method.* International Journal for Numerical Methods in Engineering .92, 343-369.

33- Violeau, D., Rogers, B.D., 2016. *Smoothed particle hydrodynamics (SPH) for free-surface flows: past, present and future*, J. Hydraul. Res. 54(1), 1–26.

34- Xu, R., Stansby, P.K., Laurence, D. (2009). *Accuracy and stability in incompressible SPH (ISPH) based on the projection method and a new approach.* Journal of Computational Physics. 228, 6703-6725.

35- Xu, R. (2010). *An Improved Incompressible Smoothed Particle Hydrodynamics Method and its Application in Free-Surface Simulations.* PhD Thesis. School of Mechanical, Aerospace and Civil Engineering, University of Manchester, United Kingdom.

INTERNATIONAL JOURNAL OF
COASTAL & OFFSHORE ENGINEERING
IJCOE Vol.3/No. 1/Spring 2018 (59-66)

Available online at: http://ijcoe.org/browse.php?a_code=A-10-61-1&sid=1&slc_lang=en

Free Vibration Analysis of Very Large Rectangular Floating Structures

Tannaz Hadizade Asar[1], Keyvan Sadeghi[2*], Arefeh Emami[3]

[1] *MSc graduate, Faculty of Civil Engineering, University of Hormozgan; tannaz.1365@yahoo.com*
[2*] *Corresponding author: Assist. Prof., Buein Zahra Technical University, Qazvin, Iran; keyvan.sadeghi@bzte.ac.ir*
[3] *PhD candidate, Faculty of Civil Engineering, Sahand University of Technology, Tabriz, Iran; a_emami@sut.ac.ir*

ARTICLE INFO

Article History:
Received: 29 Apr. 2018
Accepted: 9 Jun. 2018

Keywords:
Very large floating structure
Mindlin theory
Hydroelastic behavior
Finite element method

ABSTRACT

The dynamic behavior of a very large rectangular floating structure is considered. The structure is modelled as a plate with free edges. Two different thicknesses are considered for the model. The Mindlin plate theory is used to formulate the structure behavior. Natural frequencies, mode shapes, and stress resultants of the structure are predicted by using finite element method. For this purpose, a MATLAB code is written. The same analysis is performed by using the ANSYS software. The results of these two analysis are compared with each other and with the available results in the literature, where close agreement is observed. Therefore, the written finite element code is found to be acceptable for prediction of the dynamic behavior of very large rectangular floating structures in early stages of design.

1. Introduction

A very large floating structure (VLFS) is a viable alternative for land reclamation from coastal waters. VLFSs have been constructed as floating bridges, airports/heliports, oil storage systems, emergency rescue bases, industry spaces, hotels and amusement facilities. Compared to the traditional land reclamation methods, VLFSs are environmentally friendly, easy to construct and to remove or expand, less susceptible to earthquakes and cost effective, especially in deep coastal waters.

There are two major types of VLFS; namely the pontoon type and the semi-submersible type. The pontoon type has high stability, low manufacturing cost and is easy to repair. However, this type of VLFS is only suitable for calm waters in naturally sheltered areas or where breakwaters are constructed nearby [1]. The structure of a typical pontoon-type VLFS features a small depth to length ratio so it can be considered as a thin flat structure. In the horizontal plane, and for the design of the mooring system, the structure can be assumed to be rigid, however, in the vertical plane the elastic behavior of the thin structure cannot be ignored. A hydroelastic response analysis is, therefore, necessary. In this regard, the entire structure of a pontoon-type VLFS is usually modelled as a two-dimensional floating elastic plate with free edges [2]. For the hydroelastic analysis, different plate theories can be employed. The classical thin plate theory and the first-order shear deformation (Mindlin) plate theory are commonly used. For a VLFS the fluid-structure interaction problem includes the elastic deformations as well as the rigid body motions

In literature, there are many studies regarding to VLFS dynamical behavior where a variety of analytical and numerical methods have been used. Liew and Hun [3] investigated the dynamic behavior of a rectangular plate using the approximate least squares method. They considered the effect of shear deformation, flexural and torsional moments and shear forces using Winkler assumption and Mindlin plate theory. Xiang [4] studied the eigenvalues of vibrating plates using the first-order shear deformation theory. Rossi and Bambill [5] evaluated analytically the transverse vibrations and natural frequencies of a homogeneous rectangular plate with four different boundary conditions. Wang et al [6] showed that the Ritz and finite element methods do not satisfy natural boundary conditions in stress resultants of shear force and twisting moments at plate free edges. Beirao da Veiga [7] presented an extension of different families of well-known optimal plate models based on a modified free boundary model for plates with free edges. The hydroelastic analysis of a pontoon-type VLFS was studied by Wang et al. [8]. They studied the wave forces, drift forces, the geometrical shape and the mooring system of a VLFS. To overcome the difficulties reported in [6] they used the least squares finite difference (LSFD) method. They showed that the LSFD method is better than the Ritz and Galerkin methods for prediction of stress resultants for plates with free edges. Wu et al [9] used the LSFD method based on the classical plate theory for prediction of

natural frequencies, mode shapes, and stress resultants of freely vibrating plates with circular, elliptic and triangular shapes. Ma and Ang [10] used a finite element formulation based on the Mindlin plate theory in terms of a relative displacement concept and an assumed strain method and find results that agree with theoretical solutions. Sadrnejad and Saedi Daryan [11] investigated the vibration of a thick rectangular plate using the first order shear deformation theory. They calculated the natural frequencies of a thick plate with different boundary conditions and discussed the effect of plate thickness and dimensions on its oscillatory behavior. Xiang et al [12] proposed a discrete singular convolution (DSC) method for the free vibration of moderately thick plates based on the first-order shear deformation theory. Xiang et al [13] applied DSC-Ritz element method for the vibration of rectangular plates with mixed edge supports using the same plate theory. Hosseini-Hashemi et al. [14] analytically investigated the free vibrations of moderately thick rectangular plates with different boundary conditions. Hosseini-Hashemi et al. [15] proposed an exact solution for free vibrations of Levy-type rectangular thick plates using the third-order shear deformation plate theory. Another study regarding a new exact analytical solution for free vibrations of Reissner-Mindlin functionally graded rectangular plates is reported by Hosseini-Hashemi et al. [16]. Ramu and Mohanty [17] studied the free vibrations of rectangular plate structures using finite element method. Pereira et al. [18] addressed a dynamic formulation for thick elastic plates using the boundary element method. Eftekhari and Jafari [19] used a modified mixed Ritz-differential quadrature formulation in which all natural boundary conditions were exactly implemented. Cho et al. [20] proposed a procedure based on the assumed mode method for vibration analysis of rectangular plates with openings and arbitrary edge constraints. Thai and Choi [21] analytically studied the bending, buckling, and vibration analysis of thick rectangular plates with various boundary conditions by a refined plate theory. Senjanovic et al [22] modified the Mindlin plate theory and proposed a shear locking-free finite element formulation. Praveen et al. [23] analyzed the hydroelastic behavior of floating elastic thick plates in shallow water depth. They investigated the effect of various boundary conditions. The vibrations of moderately thick plates were studied by Senjanovic et al. [24] based on the modified Mindlin theory using a dynamic finite element technique. Khezri et al. [25] studied thin to moderately thick plates based on the shear locking-free Mindlin theory formulation using a meshless analysis. Shirkol and Nasar [26] carried out a coupled boundary element-finite element method for analyzing the hydroelastic behavior of floating plates.

For preliminary design purposes an analytical/semi-analytical approach can be employed for hydroelastic analysis of vertical motions. In this simplified model the entire pontoon-type VLFS can be modelled as a two-dimensional floating plate with free edges. In a linear theory the hydroelastic response of the floating plate (the wet plate) can be obtained by the so-called dry mode superposition method [2], where the unknown flexural response of the wet plate is assumed as a linear combination of the mode shapes of an elastic plate in air (the dry plate). Once the unknown coefficients of the superposition response, i.e., the modal amplitudes are obtained, the stress resultants of the VLFS can be predicted.

In the modal method, the classical thin plate theory or the first-order shear deformation theory are commonly employed. In the latter theory, the transverse shear deformation and the rotary inertia are allowed. In addition, the stress resultants are related to first order derivatives of the deflections and rotations while in the classical thin plate theory third order derivatives of those functions are required to compute the stress resultants. That is why more accurate stress resultants can be obtained from the Mindlin plate theory compared to the classical thin plate theory.

The natural frequencies of the wet plate are lower than the corresponding values of the dry plate. This is because of the higher effective mass due to the added mass associated with the kinetic energy transferred to the heavy fluid. However, the mode shapes of the wet and dry plates are usually assumed to be virtually the same. It is well known that the finite element method (FEM) predicts the natural frequencies and the mode shapes of plates with free edges with excellent accuracy, however, the FEM results for stress resultants, especially for the transverse shear forces and the twisting moments are not satisfactory for plates with free edges. This is partly due to the presence of very steep gradients in the stress resultant distributions near the free edges and partly due to the fact that in a FEM solution, the natural boundary conditions are imposed in a weak form [8].

For correct prediction of hydroelastic behavior of VLFS structures, it is vital to obtain accurate natural frequencies, mode shapes and stress resultants of plates with free edges. In this paper, the natural frequencies, mode shapes and stress resultants of dry plates are derived by using the finite element method based on the first-order shear deformation plate theory. In this regard, a computer code is written in MATLAB. In addition the same problem is analyzed using the ANSYS software. The results of the MATLAB code and those of ANSYS are compared with each other as well as with the relevant LSFD results [8] and the accuracy of the written code is verified. It is shown that the written code can be used to predict the hydroelastic behavior of the pontoon-type VLFS in early stages of design.

2. Problem definition

Consider an isotropic, elastic, rectangular plate with length a and width b. The origin of the Cartesian

coordinate system is placed at the plate center in its mid-plane. The xy plane coincide with the plate mid-plane and the *z*-axis is vertically upwards. According to the first-order shear deformation theory, the differential equations of motion are as follows:

$$k\frac{1-\nu}{2}\left(w_{,xx}+w_{,yy}+\psi_{x,x}+\psi_{y,y}\right)=\frac{\rho h^3}{12D}w_{,tt} \tag{1}$$

$$\psi_{x,xx}+\frac{1-\nu}{2}\psi_{x,yy}+\frac{1+\nu}{2}\psi_{y,xy}-\frac{6k(1-\upsilon)}{h^2}\left(w_{,x}+\psi_x\right)=\frac{\rho h^3}{12D}\psi_{x,tt} \tag{2}$$

$$\psi_{y,yy}+\frac{1-\nu}{2}\psi_{y,xx}+\frac{1+\nu}{2}\psi_{x,xy}-\frac{6k(1-\upsilon)}{h^2}\left(w_{,y}+\psi_y\right)=\frac{\rho h^3}{12D}\psi_{y,tt} \tag{3}$$

where, w, ψ_x and ψ_y are the generalized displacement functions associated with an arbitrary point on the plate's mid-plane. They are the displacement in the vertical direction and rotations about x and y axes, respectively. In Eqs. (1) to (3) the comma notation is used to denote the partial differentiation. The parameters k, h and ν are the shear coefficient, the plate thickness and Poisson's ratio, respectively, and D is the flexural rigidity:

$$D=\frac{Eh^3}{12(1-\nu^2)}$$

where E is Young's modulus. The following equations relate the stress resultants to the generalized displacement functions:

$$M_{xx}=D\left(\psi_{x,x}+\nu\psi_{y,y}\right) \tag{4}$$

$$M_{yy}=D\left(\nu\psi_{x,x}+\psi_{y,y}\right) \tag{5}$$

$$M_{xy}=M_{yx}=D\frac{1-\nu}{2}\left(\psi_{x,y}+\psi_{y,x}\right) \tag{6}$$

$$Q_x=k\frac{Eh}{2(1+\nu)}\left(w_{,x}+\psi_x\right) \tag{7}$$

$$Q_y=k\frac{Eh}{2(1+\nu)}\left(w_{,y}+\psi_y\right) \tag{8}$$

The first two equations are for bending moments and the last two equations are for shear forces. The middle equation represnts the twisting moments. The boundary conditions at free edges are given by the following relation:

$$Q_x=Q_y=M_{xx}=M_{yy}=M_{xy}=0 \tag{9}$$

2.1. Free Vibrations of rectangular plate

The free vibrations are studied in the absence of external loads such as waves, winds and currents. If the continuous plate is approximated by a discrete system such as a finite element mesh, the equation of undamped free vibrations can be written as

$$[M]\{\ddot{x}\}+[K]\{x\}=0 \tag{10}$$

where $[M]$ and $[K]$ are the mass and stiffness matrices and $\{x\}$ is the vector of nodal displacements. Each node has three degrees of freedom, which are w, ψ_x and ψ_y. Therefore, if the number of nodes in the mesh is N the vector $\{x\}$ will be a $3N\times 1$ vector. Assuming harmonic displacements, Eq. (10) can be rewritten as

$$([K]-\omega_i^2[M])\{\hat{x}\}_i=0 \tag{11}$$

where $\{\hat{x}\}_i$ is the vector of nodal amplitudes or the i^{th} mode shape and ω_i is the i^{th} natural frequency.

2.2. Numerical Formulation

Each node in the finite element mesh is assumed to have three degrees of freedom, i.e., w_i, ψ_{x_i} and ψ_{y_i}. Therefore, the stiffness and mass sub-matrices associated with the i^{th} and j^{th} nodes of an element will be 3×3 symmetric matrices as follows

$$[K]_{ij}=\begin{bmatrix}K_{ij}^{11} & K_{ij}^{12} & K_{ij}^{13}\\ K_{ij}^{21} & K_{ij}^{22} & K_{ij}^{23}\\ K_{ij}^{31} & K_{ij}^{32} & K_{ij}^{33}\end{bmatrix}$$

$$[M]_{ij}=\begin{bmatrix}M_{ij}^{11} & 0 & 0\\ 0 & M_{ij}^{22} & 0\\ 0 & 0 & M_{ij}^{33}\end{bmatrix} \tag{12}$$

The generalized displacement functions are approximated as interpolations between nodal values, that is

$$\begin{aligned} w&=\textstyle\sum_{j=1}^{n} w_j\varphi_j\\ \psi_x&=\textstyle\sum_{j=1}^{n}\psi_{x_j}\varphi_j\\ \psi_y&=\textstyle\sum_{j=1}^{n}\psi_{y_j}\varphi_j\end{aligned} \tag{13}$$

where n is the number of nodes per element, and φ_j is the interpolation function of the j^{th} node of the element. Introducing from Eq. (13) into motion Eqs. (1) to (3), integrating over the element area and using the integration by parts technique, the weak form of the governing equations can be derived. Then, following the common procedure in the finite element method, the elements of the stiffness and mass sub-matrices can be obtained from the following relations:

$$K_{ij}^{11}=kGh\iint\left(\varphi_{,x_i}\varphi_{,x_j}+\varphi_{,y_i}\varphi_{,y_j}\right)dxdy$$

$$K_{ij}^{12} = kGh \iint \varphi_{,x_i} \varphi_j dxdy$$
$$K_{ij}^{13} = kGh \iint \varphi_{,y_i} \varphi_j dxdy$$
$$K_{ij}^{22} = \iint \left(D\varphi_{,x_i}\varphi_{,x_j} + \frac{Gh^3}{12}\varphi_{,y_i}\varphi_{,y_j} + kGh\varphi_i\varphi_j \right) dxdy$$
$$K_{ij}^{23} = \iint \left(\nu D\varphi_{,x_i}\varphi_{,y_j} + \frac{Gh^3}{12}\varphi_{,y_i}\varphi_{,x_j} \right) dxdy$$
$$K_{ij}^{33} = \iint \left(\frac{Gh^3}{12}\varphi_{,x_i}\varphi_{,x_j} + D\varphi_{,y_i}\varphi_{,y_j} + kGh\varphi_i\varphi_j \right) dxdy \quad (17)$$

and

$$M_{ij}^{11} = \rho h \iint \varphi_i \varphi_j dxdy$$
$$M_{ij}^{22} = M_{ij}^{33} = \frac{\rho h^3}{12} \iint \varphi_i \varphi_j dxdy \quad (18)$$

where in Eqs. (17) and (18) integrations are over the element area. The rectangular plate is discretized by 20×7=140 elements. Each element in the mesh is an eight-node rectangular serendipity element with quadratic interpolation functions.

2.3. Modeling by Ansys Software

ANSYS is a powerful finite element software that is widely used for solving various engineering problems including dynamic analysis of structures. In this paper, in addition to a MATLAB code, the ANSYS software is employed for the dynamic response analysis of a plate with free edges. For this purpose the Shell 93 element is used. Each node in this element, in general, has six degrees of freedom: three displacements in *x*, *y* and *z* directions and three rotations about the same axes. The displacement in the *x* and *y* directions and the rotation about the *z*-axis are fixed to reduce the number of degrees of freedom per node to 3. The dynamic analysis is carried out by using the modal module of ANSYS and the results are presented in the following sections.

3. Results and discussion

A rectangular plate with 4 m length, 1 m width, and a thickness of 0.1 m is analyzed by both the MATLAB code and the ANSYS software. Young's modulus, Poisson's ratio and the mass density are assumed to be 210 GPa, 0.3 and 7830 kg/m^3, respectively. The results of two numerical methods are compared with each other as well as with those of Wang et al [8], which are obtained from a least squares finite difference (LSFD) method.

3.1. Natural frequencies and mode shapes

Disregarding the rigid body modes, the frequency parameters for the first four mode shapes are reported in the following table. The dimensionless frequency parameter is defined as follows:

$$\Omega = \omega b^2 \sqrt{\frac{\rho h}{D}} = \frac{\omega b^2}{h} \sqrt{\frac{12\rho(1-\nu^2)}{E}} \quad (19)$$

In this table, the FEM (MATLAB and ANSYS) and LSFD results [8] are presented. As can be seen, they are in good agreement. The maximum values of the dimensionless generalized displacement functions corresponding to the first four mode shapes are given in Table 2. Figs 1-12 show the 1st to 4th mode shapes obtained from the MATLAB, ANSYS, and LSFD methods. As can be seen, the mode shapes are in close agreement. This confirms the findings of the previous research that the finite element method is very accurate in calculating natural frequencies and mode shapes of plates with free edges. However, mode shapes derived from the written code are not as accurate as those obtained from ANSYS. This can be due to using a rather coarse mesh in MATLAB and also due to the shear locking phenomenon.

Table 1. Frequency parameters of the 1st to 4th mode shapes of the rectangular plate.

Method	Ω_1	Ω_2	Ω_3	Ω_4
MATLAB Code	1.355	3.1506	4.065	6.6.13
ANSYS software	1.357	3.159	4.076	6.635
LSFD method [8]	1.356	3.303	3.733	6.827

Table 2. Maximum value of the generalized displacement functions for the 1st to 4th modes of the rectangular plate.

	Method	1st Mode	2nd Mode	3rd Mode	4th Mode
w	MATLAB	0.036452	0.044939	0.04029	0.051884
	ANSYS	0.036494	0.045174	0.04042	0.052141
	% Error	0.115	0.52	0.32	0.493
ψ_x	MATLAB	0.042879	-0.029977	0.0828	0.054614
	ANSYS	0.042895	-0.029832	0.08295	0.054309
	% Error	0.0373	-0.45	0.181	0.558
ψ_y	MALTAB	0.0050769	-0.09035	-0.01392	-0.093806
	ANSYS	0.0051129	-0.09077	-0.01396	-0.094166
	% Error	0.704	0.463	0.286	0.382

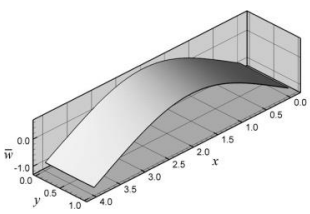

Figure 1. 1st Mode by LSFD

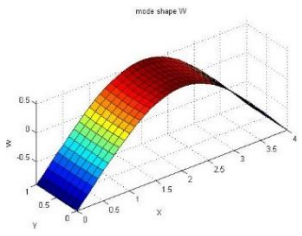

Figure 2. 1st Mode by Ansys

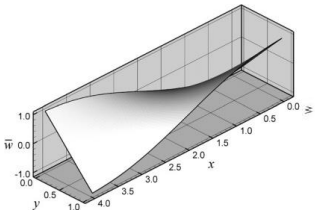

Figure 3. 2nd Mode by LSFD

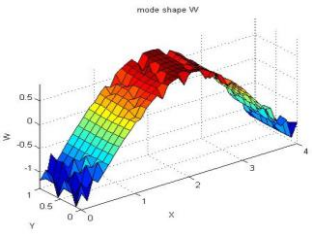

Figure 4. 1st Mode by Matlab

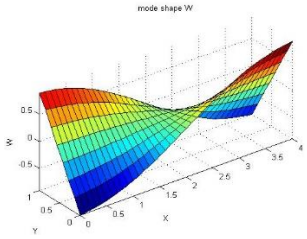

Figure 5. 2nd Mode by Ansys

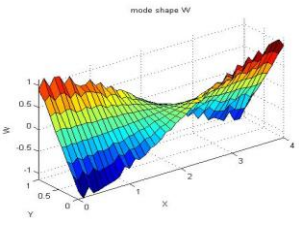

Figure 6. 2nd Mode by Matlab

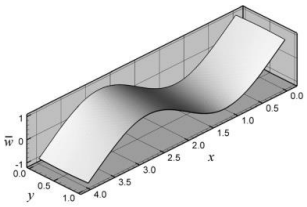

Figure 7. 3rd Mode by LSFD

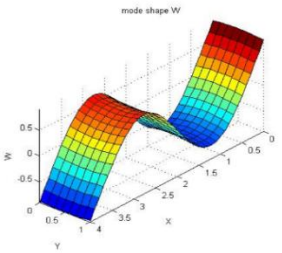

Figure 8. 3rd Mode by Ansys

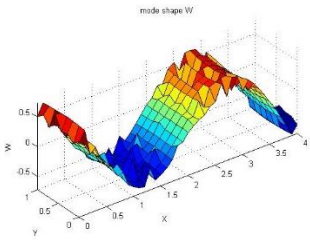

Figure 9. 3rd Mode by Matlab

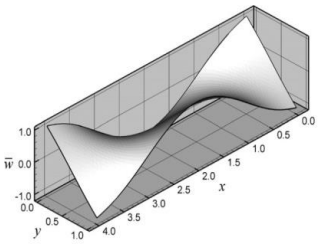

Figure 10. 4th mode by LSFD

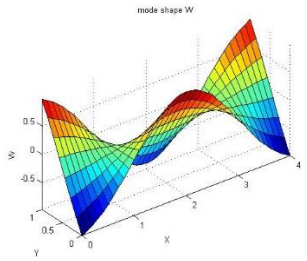

Figure 11. 4th mode by Ansys

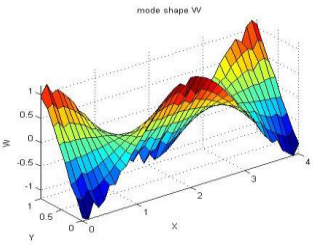

Figure 12. 4th mode by Matlab

3.2. The stress resultants of the rectangular plate

In Table. 3, the maximum values of the stress resultants corresponding to the 1st to 4th mode shapes of the rectangular plate are given. The results are obtained from the MATLAB code, ANSYS software, and LSFD method [8]. Also, figures 13-21 show $\bar{M}_{xx}$, $\bar{M}_{xy}$, and $\bar{Q}_x$ stress resultants associated with the 1st mode, and Figs. 22-27 show $\bar{M}_{yy}$ and $\bar{Q}_y$ stress resultants associated with the 2nd mode. As can be seen, in all three methods, the maximum value of the stress resultants are close enough. However the results of finite element code show some oscillations near free edges as reported in previous research [6].

3.3. The effect of thickness

In order to assess the effect of thickness on the natural frequencies of the rectangular plate, a similar plate with a thickness that is 10% of the original thickness is considered. This plate is modeled by the finite element MATLAB code and the ANSYS software. According to [27] a pontoon-type VLFS can be from few hundred to 5000 meters in length with a depth of 2 to 10 meters. This means a typical VLFS has a depth to length ration greater than 2×10^{-3}. Our numerical model with 4 m length and two thicknesses of 0.1 and 0.01 m have 25×10^{-3} and 2.5×10^{-3} depth to length ratios which are in the acceptable range. For this model, the natural frequencies and frequency parameters are given in Tables 4 and 5, respectively. The two FEM outputs (MATLAB and ANSYS) and the results of LSFD method [8] are compared with each other.

A comparison of values in Tables 1 and 5 shows that for corresponding mode shapes, by increasing the plate thickness the frequency parameter does not change significantly.

In addition, since the frequency parameter Ω in Eq. (19) is proportional with the ratio of natural frequency to thickness, ω/h, its variation for the same thickness is the same as that of ω.

Table 3. Maximum value of the stress resultants for the 1st to 4th modes of the rectangular plate.

Stresses resultants	Method	1st mode	2nd mode	3rd mode	4th mode`
$\bar{M}_x$	MATLAB	1.1021	0.4276	2.985	1.96
	ANSYS	0.9768	0.3367	2.485	1.576
	LSFD[8]	1.016	0.382	2.676	1.717
$\bar{M}_y$	MATLAB	0.0723	0.1901	0.323	0.588
	ANSYS	0.0505	0.1398	0.268	0.502
	LSFD[8]	0.0575	0.145	0.28	0.535
$\bar{M}_{xy}$	MATLAB	0.0474	1.2781	0.401	2.014
	ANSYS	0.045	0.9781	0.288	1.756
	LSFD[8]	0.0499	1.066	0.302	1.942
$\bar{Q}_x$	MATLAB	2.832	43.2382	21.15	73.201
	ANSYS	3.0863	36.2382	18.33	71.498
	LSFD[8]	3.15	38.043	19.126	72.137
$\bar{Q}_y$	MATLAB	0.1368	12.04	0.7126	44.018
	ANSYS	0.1001	10.6515	0.5166	39.797
	LSFD[8]	0.118	11.063	0.593	41.516

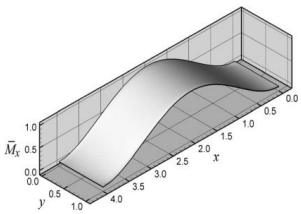

Figure 13. Bending moment $\bar{M}_x$ for 1st mode by LSFD [8]

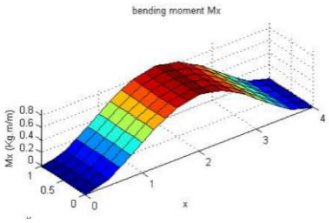

Figure 14. Bending moment $\bar{M}_x$ for 1st mode by ANSYS

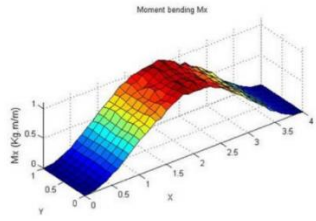

Figure 15. Bending moment for 1st mode by MATLAB

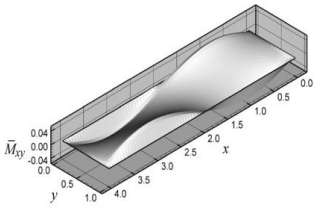

Figure 16. Twisting moment $\bar{M}_x$ $\bar{M}_{xy}$ for 1st mode by LSFD [8]

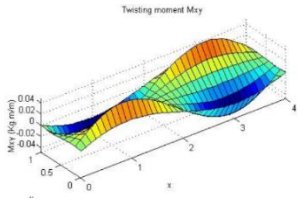

Figure 17. Twisting moment $\bar{M}_{xy}$ for 1st mode by ANSYS

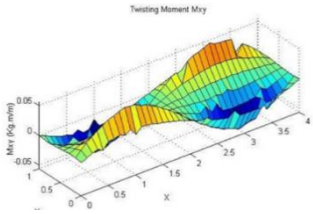

Figure 18. Twisting moment $\bar{M}_{xy}$ for 1st mode by MATLAB.

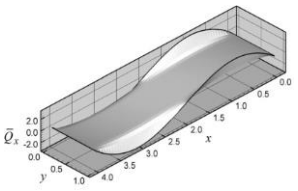

Figure 19.Shear force $\bar{Q}_x$ for 1st mode by LSFD [8]

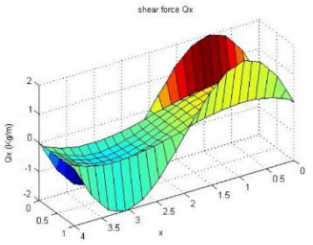

Figure 20. Shear force $\bar{Q}_x$ for 1st mode by ANSYS.

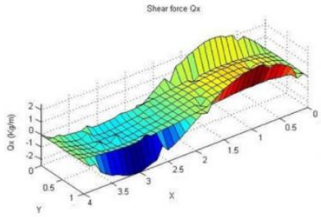

Figure 21.Shear force $\bar{Q}_x$ for 1st mode by MATLAB

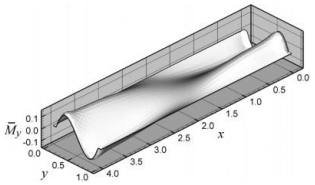

Figure 22. Bending moment $\bar{M}_y$ for 2nd mode by LSFD [8]

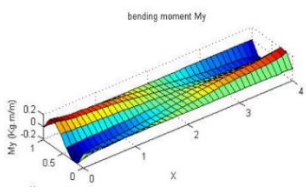

Figure 23. Bending moment $\bar{M}_y$ for 2nd mode by ANSYS

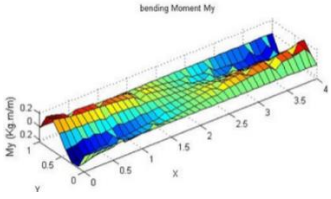

Figure 24. Bending moment $\bar{M}_y$ for 2nd mode by MATLAB

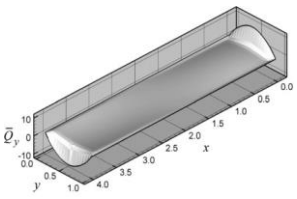

Figure 25. Shear force $\bar{Q}_y$ for 2nd mode by LSFD [8]

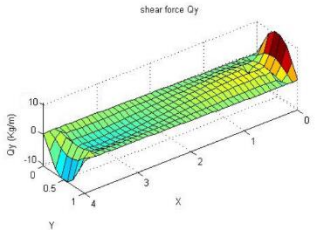

Figure 26. Shear force $\bar{Q}_y$ for 2nd mode by ANSYS.

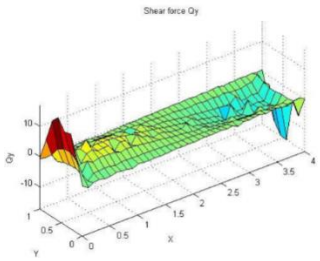

Figure 27. Shear force $\bar{Q}_y$ for 2nd mode by MATLAB

Table. 4. Natural frequencies of the 1st to 4th mode shapes of the rectangular plate with 0.01 m thickness

Method	ω_1	ω_2	ω_3	ω_4
MATLAB	1.0573	2.5724	2.9714	5.3463
ANSYS	1.0568	2.5561	2.9657	5.3080
Error	0.0473	0.634	0.192	0.716

Table. 5. Frequency parameters of the 1st to 4th mode shapes of the rectangular plate with 0.01 m thickness

Method	Ω_1	Ω_2	Ω_3	Ω_4
Matlab	1.3405	3.2614	3.767	6.778
Ansys	1.339	3.2407	3.76	6.729
LSFD[8]	1.338	3.256	3.711	6.751

Table 6. shows the maximum values of the dimensionless stress resultants of the rectangular plate with 0.01 m thickness obtained by FEM (MATLAB and ANSYS) and LSFD [8] methods corresponding to the 1st mode shape. Figs. 28-39 present the distribution of the stress resultants associated with the same mode shape. As can be seen, there are some discrepancies between FEM results and LSFD results at plate free boundaries. This can be due to several reasons. As mentioned before, two major factors are associated with: (1) the presence of steep gradients in stress resultant distributions near free edges, and (2) the weak form of imposing natural boundary conditions at free edges in FEM. It can also be observed that the results of MATLAB code are worse than those of ANSYS. This is because the finite element mesh in MATLAB was rather coarse (140 elements) and the selective reduced integration technique was not implemented.

Table. 6. Maximum value of stress resultants of the 1st mode shape of the rectangular plate with 0.01 m thickness

Method	$\bar{M}_x$	$\bar{M}_y$	$\bar{M}_{xy}$	$\bar{Q}_x$	$\bar{Q}_y$
MATLAB	0.8933	0.0595	0.0552	17.0845	0.2916
ANSYS	0.9121	0.0623	0.0695	17.2976	0.2916
LSFD[8]	1.02	0.0574	0.0676	18.2	0.31

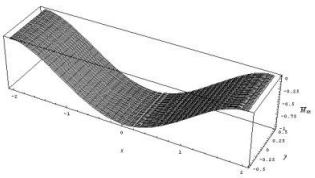

Figure.28. Bending moment $\bar{M}_x$ for 1st mode by LSFD [8]

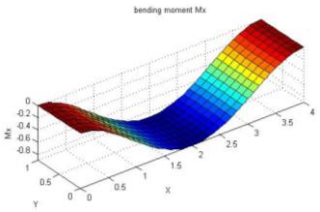

Figure.29. Bending moment $\bar{M}_x$ for 1st mode by ANSYS.

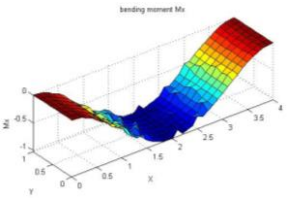

Figure.30. Bending moment $\bar{M}_x$ for 1st mode by MATLAB

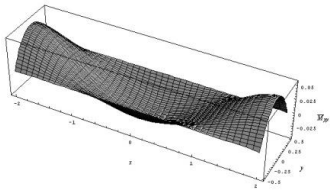

Figure.31. Bending moment $\bar{M}_y$ for 1st mode by LSFD [8]

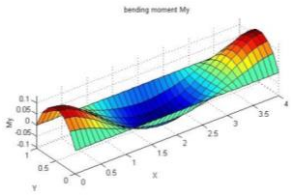

Figure.32. Bending moment $\bar{M}_y$ for 1st mode by ANSYS.

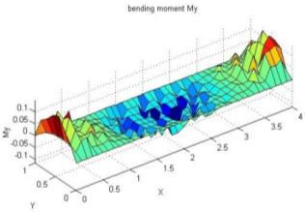

Figure.33. Bending moment $\bar{M}_y$ for 1st mode by MATLAB.

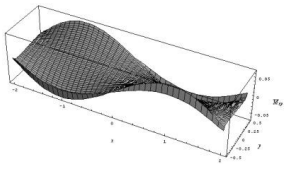

Figure.34. Twisting moment $\bar{M}_{xy}$ for 1st mode by LSFD [8]

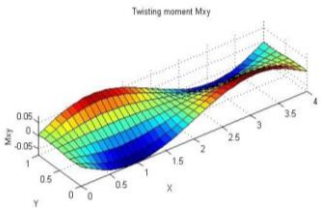

Figure.35. Twisting moment $\bar{M}_{xy}$ for 1st mode by ANSYS.

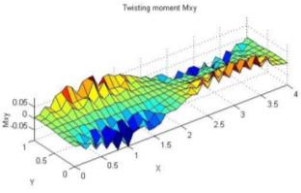

Figure.36. Twisting moment$\bar{M}_{xy}$ for 1st mode by MATLAB.

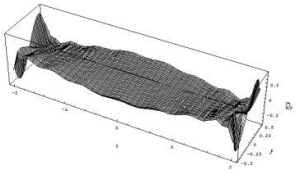

Figure.37. Shear force $\bar{Q}_y$ for 1st mode by LSFD [8]

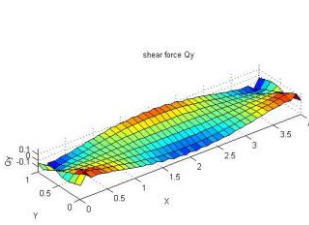

Figure.38. Shear force $\bar{Q}_y$ for 1st mode by ANSYS.

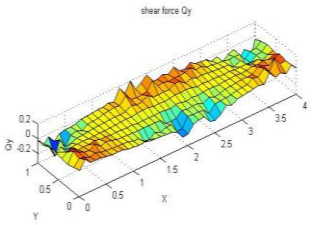

Figure.39. Shear force $\bar{Q}_y$ for 1st mode by MATLAB.

4. Conclusions

An attempt has been made to investigate the dynamic behavior of very large pontoon-type floating structures using finite element method. To this end, the structure has been modelled as a rectangular plate with free edges. A finite element code was written in MATLAB based on the Mindlin plate theory. The same problem was analyzed with ANSYS. Two plates with 0.1m and 0.01m thicknesses are considered. Natural frequencies, mode shapes and stress resultants of rectangular plates were predicted. The effect of thickness on plate's dynamic behavior was studied. It is observed that the increase in plate natural frequencies is proportional with the increase in plate thickness. The FEM results obtained from the MATLAB code and ANSYS software were compared with each other as well as with the results of a least squares finite difference method reported by [8]. It is revealed that the FEM results are satisfactory for natural frequencies and mode shapes, while the finite element results for stress resultants at plate' free edges were not satisfactory. This agrees with similar results reported in the literature.

5. References

1- Watanabe, E., Utsunomiya, T., and Wang, C.M., (2004), *Hydroelastic analysis of pontoon-type VLFS: a literature survey*, Engineering Structures Vol. 26, pp. 245-256.

2- Utsunomiya, T., (2008) *in* Very Large Floating Structures, Edited by Wang, C.M., Watanabe, E., and Utsunomya, T., Taylor & Francis.

3- Liew, K. M., Han, J. B., (1995), *Differential quadrature method for Mindlin plates on Winkler foundations*, International Journal of Mechanical Science. Vol. 38, pp. 405-421.

4- Xiang, Y., (1995), *Vibration analysis of rectangular Mindlin plates resting on elastic edge supports*, *Journal of Sound and Vibration*, Vol. 204, pp. 1-16.

5- Rossi, R. E., and Bambill, D. V., (1997). *Vibrations of a rectangular orthotropic plate with a free edge: A comparison of analytical and numerical results*, Ocean Engineering, Vol. 25, pp. 521–527.

6- Wang, C. M., Xiang, Y., Utsunomiya, T., Watanabe, E., (2000), *Evaluation of modal stress resultants in freely vibrating plates*, International Journal of Solids and Structures, Vol. 38, pp. 6525-6558.

7- Beirao da Veiga, L., (2004), *Finite element methods for a modified Reissner–Mindlin free plate model*, SIAM Journal on numerical analysis Vol. 42, pp. 1572–1591,

8- Wang, C. M., Wu, W. X., Sha, C., Utsanomiya, T., (2006), *LSFD method for accurate vibration modes and modal stress–resultants of freely vibrating plates that model VLFS*, Computers and Structures, Vol. 84, pp. 2329–2339.

9- Wu, W. X., Shu, C., Wang, C. M., (2006), *Computation of modal stress resultants for completely free vibrating plates by LSFD method*, Journal of Sound and Vibration, Vol. 297, pp. 704-726.

10- Ma, Y. Q., Ang, K. K., (2006), *Free vibration of Mindlin plates based on the relative displacement plate element*, Finite Element in Analysis and Design. Vol. 42, pp. 929-1030.

11- Sadrnejad, S. A., Saedi Daryan, A., (2009) *Vibration equation of thick rectangular plates using Mindlin plate theory*, Journal of Computer Science. Vol. 5, pp. 838-842.

12- Xiang, Y., Lai, S.k., and Zhou, L., (2010), *DSC-element method for free vibration analysis of rectangular Mindlin plates*, International Journal of Mechanical Sciences Vol. 52, pp. 548-560.

13- Xiang, Y., Lai, S.k., and Zhou, L., Lim, C.W., (2010), *DSC-Ritz element method for vibration analysis of rectangular Mindlin plates with mixed edge supports* European Journal of Mechanics, Vol. 24, pp. 619-628.

14- Hosseini-Hashemi, Sh., Rokni Damavandi Taher., Akhavan, H., and Omidi, M., (2010), *Free vibration of functionally graded rectangular plates using first-order shear deformation plate theory*, Applied Mathematical Modelling Vol. 34, pp. 1276-1261.

15- Hosseini-Hashemi, Sh., Fadaee, M., and Atashipour, S.R., (2011), *A new exact analytical approach for free vibration of Reissner-Mindlin Functionally graded rectangular plates*. International Journal of Mechanical Sciences Vol. 53, pp. 11-22.

16- Hosseini-Hashemi, Sh., Fadaee, M., and Rokni Damavandi Taher, H., (2011), *Exact solution for free flexural vibration of Levy–type rectangular thick plates via third-order shear deformation plate theory*. Applied Mathematical Modelling Vol. 35, pp. 708-727.

17- Ramu, I., and Mohanty, S.C., (2012). *Study on free vibration analysis of rectangular plate structures using finite element method,* Procedia Engineering Vol. 38, pp. 2758-2766.

18- Pereira, W.l.a., Karam, V.J., Carrer, J.A.M., and Mansur, W.J., (2012), *A dynamic formulation for the analysis of thick elastic plates by the boundary element method*. Engineering Analysis with Boundary Elements, Vol. 36, pp.1138–1150.

19- Eftekhari, S.A., and Jafari, A.A., (2013). *Modified mixed Ritz-DQ formulation for free vibration of thick rectangular and skew plates with general boundary conditions*, Applied Mathematical Modelling Vol. 37, pp. 7398-7426.

20- Cho, D.S., Vladimir, N., and Choi, T.M., (2013), *Approximate natural vibration analysis of rectangular plates with opening using assumed mode method*. Int. J. Naval Archit. Ocean Eng. Vol. 5, pp. 478-491.

21- Thai, H.T., and Choi, D.H., (2013), *Analytical solutions of refined plate theory for bending bucking and vibration analyses of thick plates*, Applied Mathematical Modelling Vol. 37, pp. 8310-8323.

22- Senjanovic, I., Vladimir, N., and Hadzic, N., (2015), *Modified Mindlin plate theory and shear locking–free finite element formulation*, Mechanics Research Communication Vol. 55, pp. 95-104.

23- Praveen, K.M., Karmakar, D., and Nasar, T., (2016), *Hydroelastic analysis of floating elastic thick plate in shallow water depth*, Perspectives in Science Vol. 8, pp. 770-772.

24- Senjanovic, I., Tomic, M., Hadzic, N., and Vladimir, N., (2017), *Dynamic finite element formulations for moderately thick plate vibtations based on the modified Mindlin theory*, Engineering Structures Vol. 139, pp. 100-113.

25- Khezri, M., Gharib, M., and Rasmusse, K.J.R., (2018), *A unified approach to meshless analysis of thin to moderately thick plates based on a shear-locking-free Mindlin theory formulation*, Thin-Walled Structures Vol. 124, pp. 161-179.

26- Shirkol, A.I., and Nasar, T., (2018), *Coupled boundary element method and finite element method for hydroelastic analysis of floating plate*. Journal of Ocean Engineering and Science Vol. 3, pp.19-37.

27- Wikipedia, (2018), Very Large Floating Structures, http://en.wikipedia.org/wiki/very_large_floating_structures. August 7, 2018.

INTERNATIONAL JOURNAL OF
COASTAL & OFFSHORE ENGINEERING
IJCOE Vol.3/No. 1/Spring 2018 (67-77)

Available online at: http://ijcoe.org/browse.php?a_code=A-10-215-1&sid=1&slc_lang=en

Numerical Simulation of the Wind-Induced Current in the Caspian Sea

Jalal Mofidi [1], Akbar Rashidi Ebrahim Hesari [2*]

[1] *Ph.D. Student, Department of Marine Physics, Hormozgan University, Iran; jalal.mofidi@yahoo.com*
[2*] *Assistant Prof., Department of Marine Physics, Tarbiat Modares University, Iran; akbar.rashidi@moares.ac.ir*

ARTICLE INFO

Article History:
Received: 14 May 2018
Accepted: 13 Jun. 2018

Keywords:
The Caspian Sea
primitive equation
finite difference
wind-induced currents

ABSTRACT

A three-dimensional primitive equation model has been developed to study wind-driven currents in the Caspian Sea (CS). The equations were solved in the spherical coordinate system with a vertical array of pressure-sigma using a finite difference Method on a staggered modified Arakawa c grid. Simulations showed that there is an anticyclonic eddy over the deep water of South Caspian Basin (SCB), which extended from surface to subsurface and persist throughout the year. The model successfully produced the coastal current along the eastern coast of the Middle Caspian Basin (MCB) with a prevailing southward component, resulting in upwelling on these coasts to compensate the surface drift. The results indicate that the bottom topography has a key role in steering currents and generated a divergence in the surface Ekman layer which balanced by convergence in the frictional bottom Ekman layer in deepest areas of the CS.

1. Introduction

The CS is the largest surrounded body of water on the Earth that constituting 44% of the global volume of lakes water and area of about 379,000 km^2. Abundant resources of oil and natural gas were found around and underwater of the CS caused the surrounding countries have started developing onshore and offshore exploitation facilities. These facilities developments have released a vast amount of pollutants into the water. These pollutants have accumulated into the water or sediment since there are no runoffs from the CS. This amount of pollutants might cause a collective death of living organisms such as a large die-off of seals during the spring of 2000[1]. Many of previous studies have been involved in monitoring projects for environmental impact assessment of pollutants transport in the CS and have been focused on biological and chemical environmental impacts, while water circulation has an important role in advection and diffusion of pollutants, it has been little measured and compared with other semi-enclosed and enclosed seas of the world, little is known of the CS variability [2]. The most urgent, still unresolved questions relating to the CS are: what is the 3-D general circulation of the sea and how is this circulation produced? The phenomenological evidence is too obscure or insufficient to give acceptable answers to these questions.

The CS has an elongated geometry that its longitudinal extent is three times larger than its latitudinal one (1000 km vs. 200-400 km), resulting in great variability of climatic conditions over the sea. There are three distinguished basins according to the geographical and topographical features: the northern shallow basin, central, and southern relatively deep basins. The North Caspian Basin (NCB) is a shallow extension with a maximum depth of 20 m. The central and the southern basins have maximum depths of 788 and 1025 m, respectively, and an underwater extension of the Apsheron peninsula with a maximum depth about 180 m separates two basins. Continental shelves areas with depth less than 100 m, mainly along the northern and eastern coasts, account for 62% of the total area of the sea [3].

The CS is enclosed sea and tidal currents are negligible. Many previous studies on the water circulation of the CS have shown that winds are primarily responsible for controlling the circulation, and changes in other forces (precipitation, evaporation and rivers run off) did not have any significant effects [3-6]. The elongated geometry and complex bottom topography of the CS, acted upon by variable wind forcing result in spatially and temporally variable currents in this basin [4, 7].

Despite the history of current observations in the CS over more than half a century, there has been a lack of data for an adequate reconstruction of the water circulation and its seasonal variability. This is due to

the fact that most of currents measurements were short-term in time, conducted in coastal areas shallower than 100m, and characterized by a small number of observational data [6, 8, 9, and 10].

Numerical modelling is one of the powerful instruments to understand water circulation as well as measurement. Several previous numerical simulations of water circulation in the CS were done using diagnostic models [6, 10, 11, 12 and 13]. The success of these models was limited due to low spatial resolution (50 km), lack of the available hydrological data and hydrodynamics structure of them. Korotenko et al. simulated the dispersal of oil due to the currents generated by constant wind using the Princeton Ocean Model (POM) in the coastal water of the CS [14]. Kara et al. investigated the impact of the wind, rivers discharge, evaporation, precipitation and salt fluxes on the sea surface current in the CS using a Hybrid Coordinate Ocean Model (HYCOM) [15]. The seasonal variability of the water circulation, sea level, and air-sea interaction in the CS were simulated by Ibrayev et al. using development of a three-dimensional primitive equation numerical Model in z-level[4]. Gunduz and Ozsoy have been investigated the wind and buoyancy-driven seasonal circulation in the Caspian Sea by using of HYCOM [16].

In recent decades, few numerical models have been specially developed to study circulation pattern in the CS. Ibrayev [17] developed a three-dimensional primitive equation numerical model (MESH) in spherical coordinates system with vertical array Z for simulation of water circulation in the CS. A conjunctive numerical model consisting of a 2D depth average model and a 3D pseudo compressible model in the Cartesian coordinate system was developed by Zounemat Kermani and Sabbagh Yazdi to simulate wind driven current in the CS [18]. Kitazawa and Yang (2012) simulated water circulation in the CS by means of developmet of a three dimensional numerical simulation based on a hydrodynamic ocean model (MEC) in the Cartesian coordinate system [19]. Nasimi and Ghiassi (2006) also developed a three-dimensional model of water circulation of the CS in the Cartesian coordinate system [20].

With regard to three basins with complex bottom topography and vast shallow water area in the CS, using numerical models in z-level is associated with many problems such as numerical instability. In addition, there is no possibility of accurately determining the topography and variability of the free surface level. Also, the lower number of vertical layers in shallow water areas reduces the accuracy of simulation of currents variations along the vertical direction in these areas. Therefore using of Sigma coordinate system in the vertical direction caused the numerical mesh fits the free surface and bed very closely that providing a higher resolution near boundaries. In addition, the number of layers along the vertical direction in the shallow water and deep areas is the same, which makes it possible to better understand of variability of currents at different depths of water. One of the other benefits of this model is the ability to couple with atmospheric models, as a result of using pressure sigma coordinate in vertical direction.

2. Model description

2.1. The basic equations in pressure-sigma coordinate

The pressure-sigma coordinate system is applied in the vertical direction. Since the bottom pressure can vary with time and space, the normalized pressure-Sigma coordinate has therefore been adopted, which is defined as [21]:

$$\sigma = \frac{p - p_a}{p_b - p_a} \tag{1}$$

Where p is the pressure, p_a is atmospheric pressure at the sea surface and p_b is the sea bottom pressure. Sigma will always be 0 at the sea surface at any time, and 1 at the sea bottom.

The primitive equation was rewritten in the spherical pressure-Sigma coordinate system using the method introduced by Kasahara [22]. In this method, a generalized vertical coordinate σ is assumed to be related to the height z by a single-valued monotonic function. In terms of the z coordinate, σ is a function of x, y, z, and t, as follows:

$$\sigma = \sigma(x,y,z,t) \tag{2}$$

On the other hand, in terms of σ as a vertical coordinate, z becomes a dependent variable, so that

$$z = z(x,y,\sigma,t) \tag{3}$$

Any other scalar (or vector) dependent variable, say A, can be expressed in terms of either coordinate system as $A(x,y,z,t)$ or $A(x,y,\sigma,t)$. These functions become identical when either z or σ is replaced by its functional form in terms of the other, as follows:

$$A(x,y,\sigma,t) = A(x,y,z(x,y,\sigma,t),t) \tag{4}$$

When a partial derivative is taken with respect to s, where s is x, y, or t, the result can be expressed by the following equation:

$$\left(\frac{\partial A}{\partial s}\right)_\sigma = \left(\frac{\partial A}{\partial s}\right)_z + \frac{\partial A}{\partial \sigma}\frac{\partial \sigma}{\partial z}\left(\frac{\partial z}{\partial s}\right)_\sigma \tag{5}$$

Where the subscript z or σ denotes the vertical coordinate. Similarly, the vertical derivatives are related as follows:

$$\frac{\partial A}{\partial \sigma} = \frac{\partial A}{\partial z}\frac{\partial z}{\partial \sigma} \tag{6}$$

or alternatively

$$\frac{\partial A}{\partial z}=\frac{\partial A}{\partial \sigma}\frac{\partial \sigma}{\partial z} \tag{7}$$

When (7) is substituted into (6), the result can be written as:

$$\left(\frac{\partial A}{\partial s}\right)_{\sigma}=\left(\frac{\partial A}{\partial s}\right)_{z}+\frac{\partial A}{\partial \sigma}\frac{\partial \sigma}{\partial z}\left(\frac{\partial z}{\partial s}\right)_{\sigma} \tag{8}$$

The last expression can be used successively with s = x and y to form the gradient of *A* and a vector *B* to give the two-dimensional divergence with the following equations:

$$\vec{\nabla}_{\sigma}A=\vec{\nabla}_{z}A+\frac{\partial A}{\partial \sigma}\frac{\partial \sigma}{\partial z}\vec{\nabla}_{\sigma}z \tag{9}$$

$$\vec{\nabla}_{\sigma}\cdot\vec{B}=\vec{\nabla}_{z}\cdot\vec{B}+\frac{\partial \vec{B}}{\partial \sigma}\frac{\partial \sigma}{\partial z}\cdot\vec{\nabla}_{\sigma}z \tag{10}$$

When s = t in (8), the result is defined as follows:

$$\left(\frac{\partial A}{\partial t}\right)_{\sigma}=\left(\frac{\partial A}{\partial t}\right)_{z}+\frac{\partial A}{\partial \sigma}\frac{\partial \sigma}{\partial z}\left(\frac{\partial z}{\partial t}\right)_{\sigma} \tag{11}$$

By using of the (8), can be written the transformation of horizontal derivatives from Spherical coordinates to pressure-sigma coordinate by the following equations:

$$\begin{cases}\left(\dfrac{\partial A}{\partial \lambda}\right)_{r}=\left(\dfrac{\partial A}{\partial \lambda}\right)_{\sigma}+\dfrac{\rho}{p_b-p_A}\dfrac{\partial A}{\partial \sigma}\left(\dfrac{\partial \Phi}{\partial \lambda}\right)_{\sigma}\\ \left(\dfrac{\partial A}{\partial \varphi}\right)_{r}=\left(\dfrac{\partial A}{\partial \varphi}\right)_{\sigma}+\dfrac{\rho}{p_b-p_A}\dfrac{\partial A}{\partial \sigma}\left(\dfrac{\partial \Phi}{\partial \varphi}\right)_{\sigma}\\ \dfrac{\partial A}{\partial r}=-\dfrac{\rho g}{p_b-p_A}\dfrac{\partial A}{\partial \sigma}\end{cases} \tag{12}$$

Where λ is the longitude, ϕ latitude, r radius of the Earth, ρ density, g acceleration due to gravity and Φ geopotential.

By using this method the horizontal momentum equations in pressure-sigma coordinate can be expressed by the following equations:

$$\begin{aligned}&\frac{\partial u}{\partial t}+\frac{u}{r\cos\phi}\frac{\partial u}{\partial \lambda}+\frac{v}{r}\frac{\partial u}{\partial \phi}-w\frac{\rho g}{p_b-p_A}\frac{\partial u}{\partial \sigma}=\\ &\frac{uv\tan\phi}{r}-\frac{uw}{r}+fv-ew\\ &-\frac{\alpha}{r\cos\phi}\left[\frac{\partial p}{\partial \lambda}+\frac{\rho}{p_b-p_a}\frac{\partial p}{\partial \sigma}\left(\frac{\partial \Phi}{\partial \lambda}\right)\right]+F_{\lambda}\end{aligned} \tag{13}$$

$$\begin{aligned}&\frac{\partial v}{\partial t}+\frac{u}{r\cos\phi}\frac{\partial v}{\partial \lambda}+\frac{v}{r}\frac{\partial v}{\partial \phi}-w\frac{\rho g}{p_b-p_A}\frac{\partial v}{\partial \sigma}=\\ &-\frac{u^2\tan\phi}{r}-\frac{uw}{r}-fu\\ &-\alpha\frac{1}{r}\left[\frac{\partial p}{\partial \phi}+\frac{\rho}{p_b-p_A}\frac{\partial p}{\partial \sigma}\left(\frac{\partial \Phi}{\partial \phi}\right)\right]+F_{\phi}\end{aligned} \tag{14}$$

Where

$$\frac{d...}{dt}=\frac{\partial...}{\partial t}+\frac{u}{r\cos\phi}\frac{\partial...}{\partial \lambda}+\frac{v}{r}\frac{\partial...}{\partial \phi}-w\frac{\rho g}{p_b-p_A}\frac{\partial...}{\partial \sigma} \tag{15}$$

Where u and v are the zonal and meridional velocity components, w the vertical Velocity, $f=2\Omega\sin\phi$ $e=2\Omega\cos\phi$ Coriolis parameters, Ω representing the angular velocity of Earth's rotation, F_{λ} and F_{ϕ} are frictional forces per unit mass.

The hydrostatic equation is obtained from the relation:

$$\frac{\partial \Phi}{\partial \sigma}=-\frac{p_b-p_A}{\rho} \tag{16}$$

The continuity equation is:

$$\begin{aligned}&\frac{1}{p_b-p_A}\frac{D}{Dt}\left(p_b-p_A\right)+\frac{1}{r\cos\phi}\frac{\partial u}{\partial \lambda}\\ &+\frac{1}{r}\frac{\partial v}{\partial \phi}+\frac{\partial \dot{\sigma}}{\partial \sigma}=0\end{aligned} \tag{17}$$

Where $\dot{\sigma}=\dfrac{d\sigma}{dt}$ is the representative of vertical velocity and obtained by integrating the continuity equation from the surface to an arbitrary vertical depth, as follows:

$$\begin{aligned}\dot{\sigma}(\sigma)=&-\frac{\sigma}{p_b-p_A}\frac{\partial}{\partial t}\left(p_b-p_A\right)-\\ &\frac{1}{p_b-p_A}\left\{\begin{aligned}&\int_{\sigma=0}^{\sigma=\sigma}\frac{1}{r\cos\phi}\frac{\partial}{\partial \lambda}\left[\left(p_b-p_A\right)u\right]d\sigma\\ &-\int_{\sigma=0}^{\sigma=\sigma}\frac{1}{r}\frac{\partial}{\partial \phi}\left[\left(p_b-p_A\right)v\right]d\sigma\end{aligned}\right\}\end{aligned} \tag{18}$$

The state equation of seawater is [22]:

$$\rho(S,T,p)=\frac{\rho(S,T,0)}{1-p/K_T(S,T,p)} \tag{19}$$

Where S and T are the salinity and temperature of sea water, K_T is the thermal diffusivity coefficient.

The geopotential height was calculated by integrating the hydrostatic equation from sea bottom to a specific depth, and can be written as:

$$\Phi_{(i,j,\sigma)}=\Phi_{(i,j,\sigma=1)}+\frac{\left(p_b-p_a\right)\left(1-\sigma\right)}{\left\langle\rho\right\rangle} \tag{20}$$

Where $\langle\rho\rangle$ is the mean density and calculated by the following equation:

$$\langle \rho \rangle = \frac{1}{1-\sigma} \int_{\sigma=1}^{\sigma=\sigma} \rho d\sigma \tag{21}$$

The pressure was calculated by the following equation:

$$p = p_A + \sigma \left(p_b - p_A \right) \tag{22}$$

In order to apply the hydrodynamic effects in the model, the Bottom pressure tendency equation is obtained by integrating the continuity equation from the sea surface to the sea bottom by the following equation:

$$\frac{\partial p_b}{\partial t} = - \int_{\sigma=0}^{\sigma=1} \frac{1}{r \cos\phi} \frac{\partial}{\partial \lambda} \left[\left(p_b - p_A \right) u \right] d\sigma - \int_{\sigma=0}^{\sigma=1} \frac{1}{r} \frac{\partial}{\partial \phi} \left[\left(p_b - p_A \right) v \right] d\sigma + \frac{\partial p_a}{\partial t} \tag{23}$$

The terms including the velocity in the above relation are the hydrodynamic parts of pressure distribution.

The finite difference method was employed for the numerical solution of model equations. The Lax-Wendroff and Dufort-Frankel schemes were used for advection and diffusion terms respectively. The Dufort-Frankel scheme is unconditionally stable since the Courant-Friedrichs-Lewy stability condition must be satisfied for the Lax-Wendroff scheme [24]. The staggered modified Arakawa C grid was used for the spatial discretization in this model.

2.2 Boundary Condition

The No-slip condition was used at lateral boundaries that tangential and normal components of velocity were set to be zero as follows:

$$\begin{cases} u(\lambda, \varphi, \sigma, t) \cdot \mathbf{n} = 0 \\ v(\lambda, \varphi, \sigma, t) \cdot \mathbf{n} = 0 \end{cases} \tag{24}$$

$$\begin{cases} u(\lambda, \varphi, \sigma, t) \cdot \mathbf{t} = 0 \\ v(\lambda, \varphi, \sigma, t) \cdot \mathbf{t} = 0 \end{cases} \tag{25}$$

Where $\mathbf{n}$ and $\mathbf{t}$ are the normal and tangential unit vectors.

At the sea surface the corresponding boundary conditions are:

$$p = p_A \tag{26}$$

$$\left(\frac{-\mathbf{A}_\sigma g}{p_b - p_A} \frac{\partial u}{\partial \sigma}, \frac{-\mathbf{A}_\sigma g}{p_b - p_A} \frac{\partial v}{\partial \sigma} \right) = \left(\frac{\tau_{s\lambda}}{\rho}, \frac{\tau_{s\phi}}{\rho} \right) \tag{27}$$

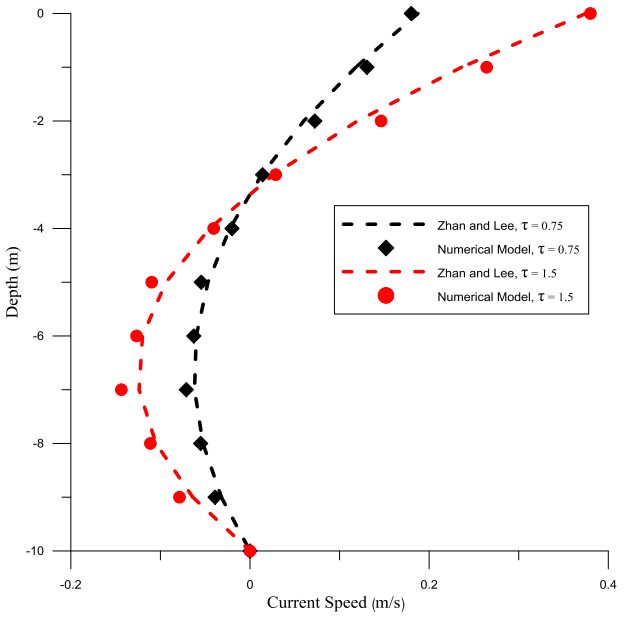

Fig.1. Comparison of numerical model predictions with analytical solution at the centre of the basin.

Where $\tau_{s\lambda}$ and $\tau_{s\phi}$ are the Sea surface frictional stresses caused by the wind in the longitude and latitude directions and can be calculated by:

$$\left(\tau_{s\lambda}, \tau_{s\phi} \right) = \left(c_D \rho_a |\mathbf{V}_{10}| u_{10}, c_D \rho_a |\mathbf{V}_{10}| v_{10} \right) \tag{28}$$

Where $\mathbf{V}_{10} = \left(u_{10}, v_{10} \right)$ is the wind velocity vector at 10 meters above the sea surface, ρ_a is air density equal 1.3 kg m^{-3}. C_D is the drag coefficient and calculated by Wu method as follows [25]:

$$c_D = \begin{cases} \left(0.8 + 0.065 |\mathbf{V}_{10}| \right) \times 10^{-3} & |\mathbf{V}_{10}| > 7.5 ms^{-1} \\ 1.2875 \times 10^{-3} & |\mathbf{V}_{10}| < 7.5 ms^{-1} \end{cases} \tag{29}$$

At the sea bottom, the boundary condition can be written as:

$$p = p_b \tag{30}$$

$$\left(\frac{-\mathbf{A}_\sigma g}{p_b - p_A} \frac{\partial u}{\partial \sigma}, \frac{-\mathbf{A}_\sigma g}{p_b - p_A} \frac{\partial v}{\partial \sigma} \right) = \left(\frac{\tau_{b\lambda}}{\rho}, \frac{\tau_{b\phi}}{\rho} \right) \tag{31}$$

Where $\tau_{b\lambda}$ and $\tau_{b\phi}$ are bottom frictional stresses in longitude and latitude directions respectively, and can be calculated by Nihoul's method as follows [26]:

$$\tau_b = -m \tau_s + D \bar{\mathbf{V}} |\bar{\mathbf{V}}| \tag{32}$$

Where τ_b is the bottom friction, $\bar{\mathbf{V}}$ is the mean flow velocity, m=0.07 and D=211×10^{-5} are two empirical coefficients.

2.3 Numerical model validation and sensitivity analyses

To prove the model accuracy and efficiency, a comparison of the model predictions with analytical solutions was performed for a standard case in a rectangular basin. This experiment was examined the vertical profile of horizontal velocity in a closed basin with a flat bed and with non-slip bottom condition.

In this test case, the Coriolis effect and the horizontal diffusion and cross (y-direction) terms were neglected, leading to a balance between the gravitational force due to the surface elevation gradient, the vertical diffusion of momentum, and the surface wind stress and the bottom friction term in the momentum equation. The analytical solution for the horizontal velocity component in a well-mixed channel with a known constant vertical eddy viscosity coefficient is calculated by method introduced by Li and Zhan as follows [27]:

$$u=\frac{\sigma(h+\eta)(3\sigma-2)}{4A_v\rho}\tau_{xz}^{s} \tag{33}$$

Where $\sigma=\frac{h+z}{h+\eta}$, u is the horizontal velocity, τ_{xz}^{s} is the surface wind stress, A_v is the vertical eddy viscosity, η is the surface elevation, *h* is the total water depth, z is the vertical coordinate which is equal to zero at the sea surface and equal to *h* at the sea bottom. In the numerical simulations, the following parameters were used;

h = 10 m, g = 9.8 m s^{-2}, ρ = 1025 kg m^{-3}, A_v = 0.01 m^2 s^{-1}; Δt = 5 s; f = 0.

The test basin was rectangular, with an area of 2 km long × 2 km wide and depth of 10 m. the simulations were performed using 21 pressure Sigma vertical layers and with a square grid by size of 100 m in both longitude and latitude directions. For this test case two steady wind conditions were applied, where the wind stress was set to τ_{xz}^{s} = 0·75 and τ_{xz}^{s} = 1.5 N m^2, respectively. The model was started with a zero velocity field and surface elevation and the simulation continued under constant wind stress. Comparisons of the model predictions with analytical solutions at the centre of the basin are shown in Fig. 1 where it can be seen that, as expected, the upper layer currents are in the wind direction whereas the lower layer currents are in the opposite direction, to maintain mass balance in the closed basin.

The Mean Absolute Percentage Error (MAPE) was used to calculate error rates. MAPE usually expresses accuracy as a percentage, and is defined by the following relation:

$$MAPE=\frac{1}{n}\sum_{i=1}^{n}\left|\frac{A_i-N_i}{A_i}\right|\times 100 \tag{34}$$

Where A_i is the analytical value and N_i is the numerical value. The comparison showed a discrepancy of approximately 10% between the numerical and analytical solution for wind stress 0.75 and about 8% for wind stress 1.5 N m^{-2}.

The Root Mean Square (RMS) Error value between prediction and analytical solution was found to be very small. The calculated RMS values for the wind stress of 0.75 and 1.5 N m^{-2} were equal to 0.007 and 0.015, respectively.

Several tests and sensitivity analysis were performed during the preparation of the model. The model was tested in a rectangular standard case study against the number of layers and cells, with and without Coriolis force, different depths, different vertical eddy viscosities, constant and variable amount of sigma. After achieving ideal conditions, the model was tested against actual bottom topography of the CS and different wind conditions. By eliminating the model's instabilities sources, the final model was used to simulation of wind induced currents in the Caspian Sea.

2.4 Model Inputs.

In the numerical simulation, the number of layers in vertical direction is equal to 21, time step is equal to 5 s, space step is equal to 0.125 degree, the number of points in longitude direction is 73 and in latitude directions is 97, salinity of sea water at the surface layer is equal to 20 ppt and sea surface temperature is equal to 25 c^o. The other model parameters in the numerical simulations were: Horizontal eddy viscosity = 10^2 m^2 s^{-1}, Vertical eddy viscosity = 10^{-2} m^2 s^{-1}, Air pressure = 101300 pa, Earth radius = 6370949 m and earth angular velocity = 7.2921 ×10^{-5} rad s^{-1}.

2.4.1 Bathymetry data

Fig. 2 shows the bottom topography of the CS. The model uses bathymetric data obtained from the General Bathymetric Chart of the Oceans (GEBCO) datasets. The minimum depth in the model is 3 m in the NCB, and a maximum depth of 1025 m occurs in the SCB. The grid resolution of the model is equal to 0.125^o in both latitude and longitude directions. The model grid area covers the entire CS from 36° to 48° N and 46° to 55° E.

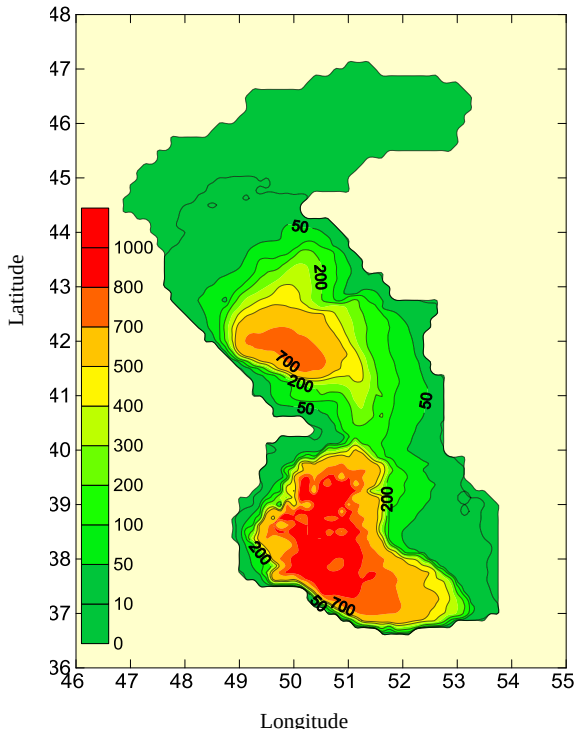

Fig.2. Bottom topography of the Caspian Sea (depths in meters).

2.4.2 Wind.

The spatiotemporally varying wind data in 10 meters height above the sea surface available from the European Centre for Medium-Range Weather Forecasts reanalysis (ECMWF ERA15) dataset for 1982, was utilized in the model. The substantial agreement is observed between these data and the climatologic winds measurements made at ships and 72 coastal meteorological stations [3]. The wind data time step is 24 hours (daily) and the data resolution is 0.125^{o} both in latitude and longitude directions. Fig. 3 shows Monthly mean wind velocity vectors computed based on the ECMWF ERA15 data set in 1982. The monthly mean wind speed is typically between 3-6 m s^{-1} during the selected year with a maximum of 5.8 m s^{-1} in June and a minimum of 3.2 m s^{-1} in December. The strongest winds occur in the SCB during February till November. In most months of the year, the north-northeast ward winds prevail in the NCB, and the southeast and southwest ward winds prevail in the MCB, Also, the south-southwest ward winds are dominated throughout the year in the SCB.

3. Result

The annual mean surface currents are computed based on the model results are shown in Fig. 4. They are generally found to be weak, with maximum values of about 5 cm s^{-1} in shallow water areas in the NCB and near the eastern coast of the SCB, as has also been noted numerically by Korotenko et al. and Ibraev et al., as well [14, 28]. Although surface currents driven by daily winds demonstrate significant variability, this is not reflected in the annual averaged circulation. According to Fig.4, an anticyclonic gyre almost entirely covered the MCB, also a sub-basin scale anticyclonic gyre is found in the SCB.

The Fig.5 shows the monthly averaged surface currents in the CS. In most month of the year, the east and northeast ward surface currents dominated in the NCB. The wind direction changes during February (Fig.3) and May (not shown), resulting change in current direction to become southeast and southwest ward respectively.

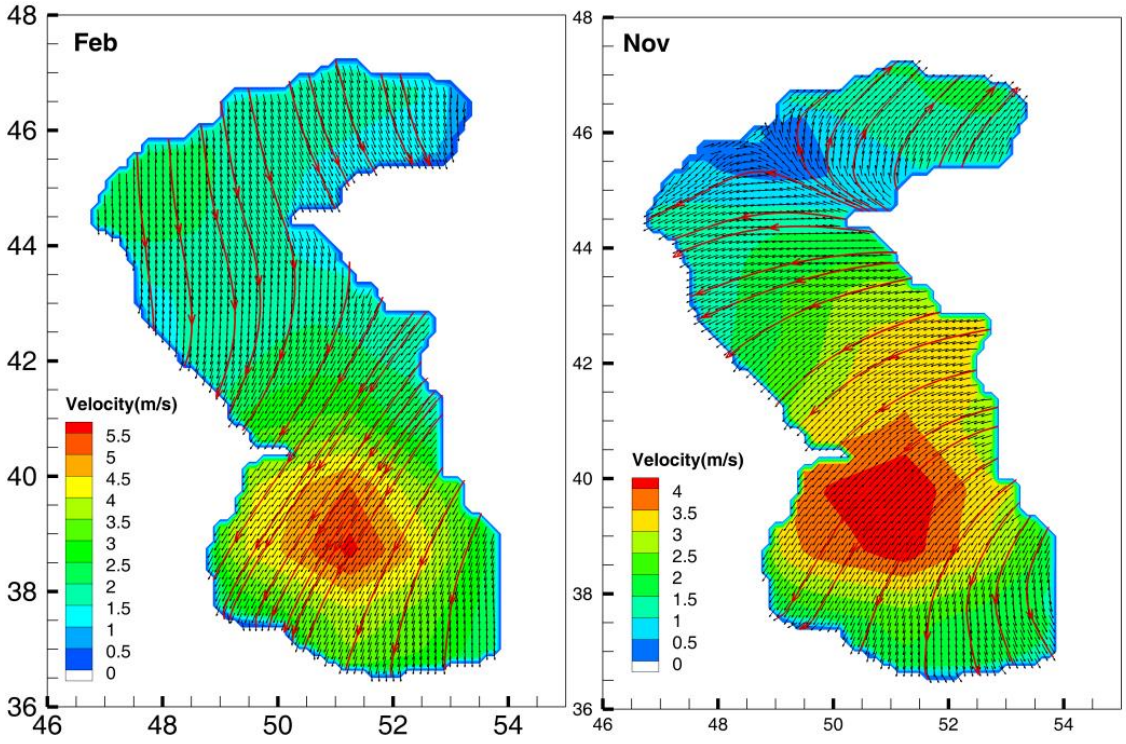

Fig.3. Monthly mean wind velocity vectors based on the ECMWF ERA15 data set.

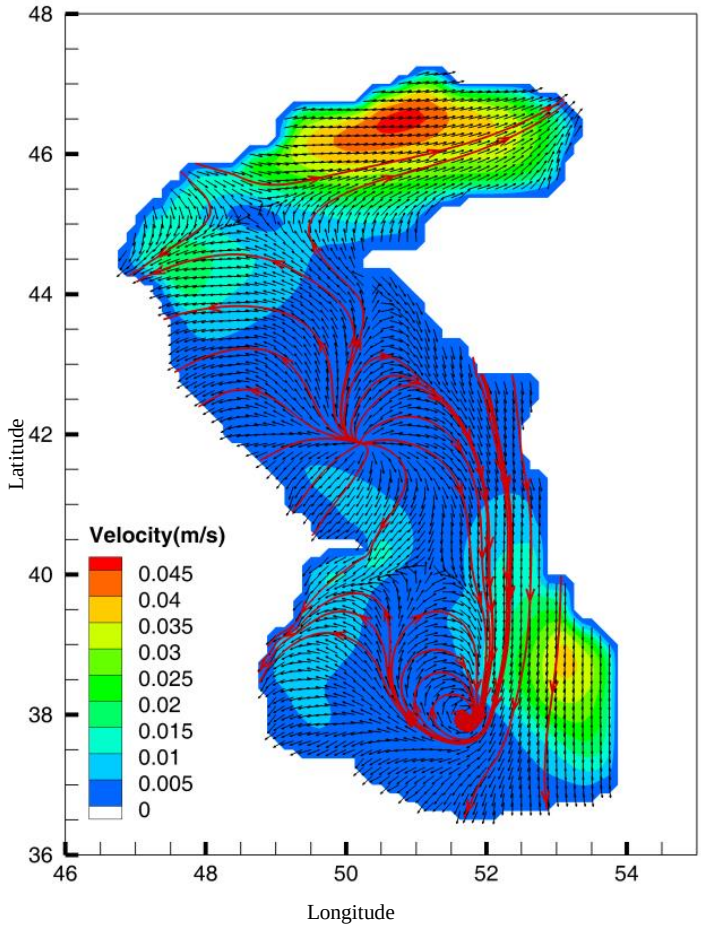

Fig.4. Annual mean surface current (m s^{-1}) in the Caspian sea

The circulation pattern in the eastern coast of the MBC can be divided into two periods (Fig.5): a) February-July when the southeast ward surface current resulting in an offshore transport of water mass and upwelling along these coasts, as has also been noted by Kosarev and Yablonskaya; Terziev et al.; Kara et al. and Ibrayev et al. [3-6]. b) August-January when the wind direction gradually changes cause a clockwise rotation in surface current to become northwest ward, resulting in onshore transport of water mass and downwelling along these coasts. This effect was also noted by Lednev and Ibrayev et al. [4, 29]. Also, there are found a divergence of surface currents over the deep water of MCB in most months of the year and an anticyclonic eddy in February which extended from surface to subsurface. An anticyclonic eddy and its adjacent currents are diverged in deeper regions of the SCB and establish a counter clockwise alongshore current near the western coasts and an eddy extended from surface to subsurface. An anticyclonic eddy and its adjacent currents are diverged in deeper regions of the SCB and establish a counter clockwise alongshore current near the western coasts and an eddy in the middle part of the basin all year round. The surface currents are very sensitive to change of wind direction and speed near the eastern coasts of the SCB due to the vast continental shelf of this area. The maximum of surface current velocities in the SCB usually take place near this coast. In most month of the year, the south and southwest ward surface currents dominated in this area, and change of wind direction to southeast ward during April to July resulting in change the direction of the surface current to become southeast ward.

The monthly averaged currents in subsurface layers in February are shown in Fig. 6. The maximum of monthly mean velocity of the surface and subsurface currents take place in the NCB in February. The depths of these areas are less than 10 m. By increase the depth the direction of southeast ward surface currents in the NCB changes to the northwest ward and the maximum of current velocity are reduced from 14.2 to 2.32 cms^{-1} on the fifth layer of sigma coordinates. The directions of currents in the next layers are in the northwest ward and the maximum of current velocity increases in the eighth layer to 5 cm s^{-1} due to the low depth of this area and changing the direction of current to compensate offshore currents at the surface. The maximum of current velocity decreases in the tenth layer to 1.78 cm s^{-1} due to the influence of bottom friction.

In the MCB, the anticyclonic eddy continues until the third layer and as the depth increases, the currents becomes to the northwest ward. The south and southeast ward along shore currents near the eastern coasts of MCB rotate clockwise by increasing the depth. They are completely in the opposite direction of surface current on the fifth layer to compensate the offshore transport of water mass on the surface layer.

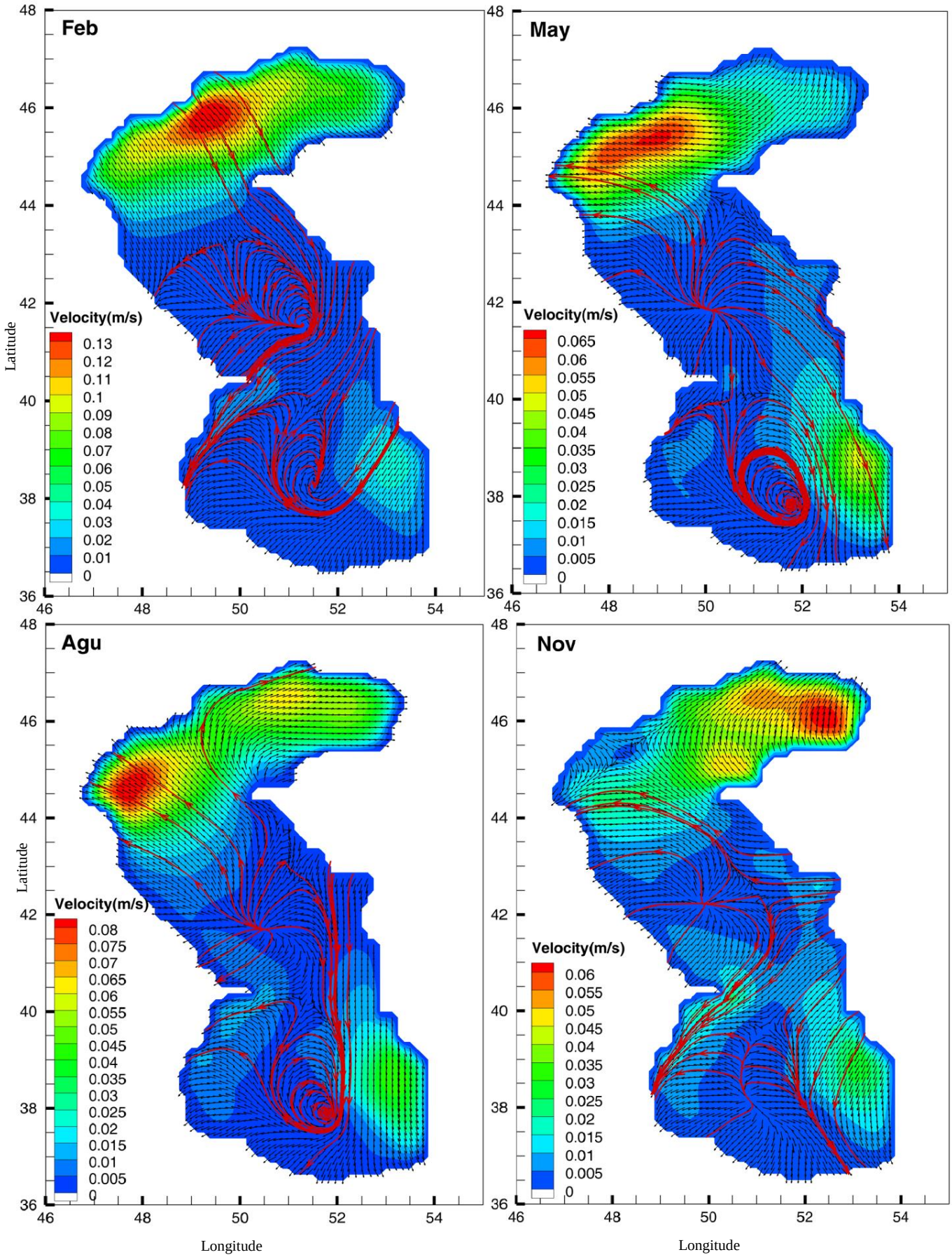

Fig.5. Monthly means surface currents (m s^{-1}) in the Caspian Sea.

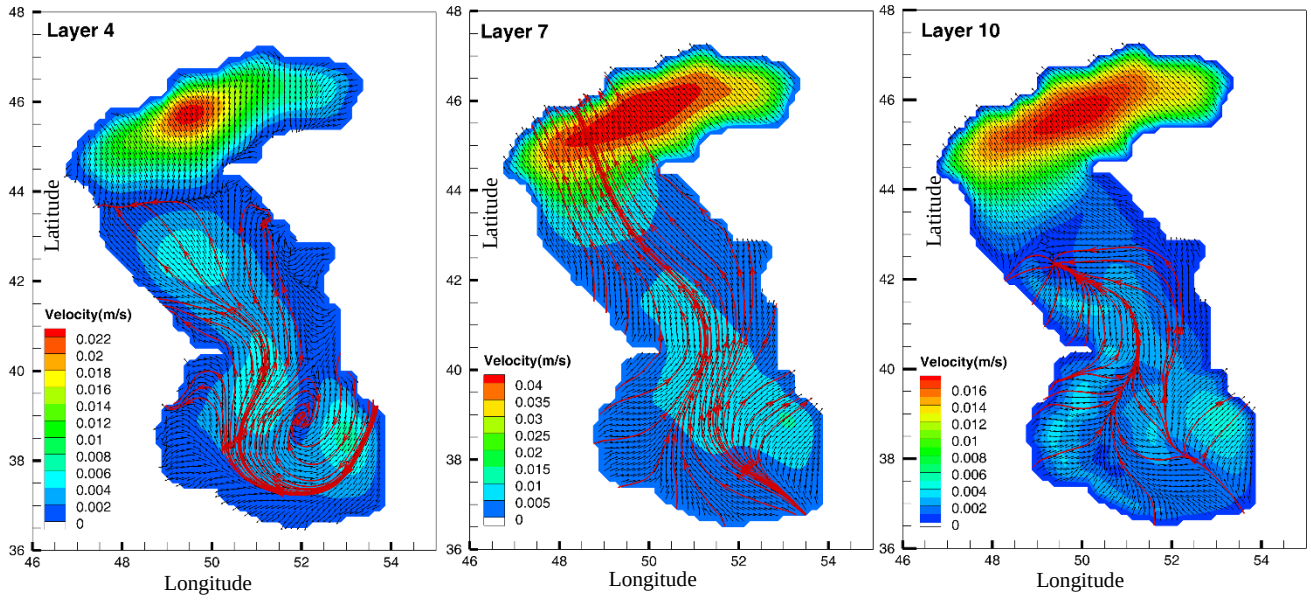

Fig.6. Monthly means currents in February for layers 4, 7 and 10 in pressure Sigma Coordinate.

The anticyclonic eddy over the deep water of SCB extended from surface to subsurface until the fifth layer. Near the western and eastern coasts of the SCB, the southwest ward surface current varies clockwise by increasing the depth and flowing to the northeast ward on the sixth layer of sigma.

As shown in Fig. 6, the currents in the layer near the sea bottom (layer 10) are converged together into deep regions of the MCB and SCB. The divergences in the surface Ekman layer are balanced by the convergences in the bottom Ekman layer. The divergence and convergence of currents of the SCB are more stable in terms of location and intensity against than the divergence and convergence of the MCB, which is the result of the SCB's steeper bed slope.

4. Conclusion

The study aims at reproducing mean values of wind-driven currents of the CS. Monthly mean values of current speed are more important for predicting the transport of pollution compared to currents occurring at extreme storm conditions. A 3-dimensional primitive equation model is presented to simulate monthly variability of the CS circulation. Due to the vast and shallow coastal waters and deep interior regions, a numerical model with convenient vertical coordinate systems is required to simulation wind driven current in the CS. In this study, this is accomplished by using a sigma-pressure Coordinate system. This simulation reveals fundamental features of the CS circulation as upwelling along the eastern coast and an anticyclonic eddy in both SCB and MCB.

The surface current must be theoretically aligned 45° clockwise from the wind direction in the northern hemisphere, while the angle between the directions of surface current and wind is very small in the shallow water areas of the CS due to the large effects of bottom friction. In these areas the circulation pattern is very sensitive to the wind direction and speed. In the CS deep waters the direction of the surface currents are changing continuously by the Coriolis force, and establish a number of eddies in the MCB and SCB. The anticyclonic eddy is the permanent feature of the SCB and is more stable against to the circulation patterns in the NCB and MCB, as a result of more depth and steeper bed slop of the SCB. This feature is in agreement with Peeters et al. [30], who explained enhanced the vertical stability of the SCB, according to the buoyancy frequency.

The simulation of circulation pattern in the CS demonstrates that a divergence in the surface Ekman layer is balanced by a convergence in the frictional Ekman layer near the sea bottom in both the SCB and MCB. These effects show the bottom topographic features have an important role in steering currents in the CS, as also has been noted by Ghaffari et al. [31].

Comparison of the results of this simulation with the previous numerical studies shows that this model is capable to simulation circulation pattern in a basin with complex bottom topography and spatio-temporal variable wind. Also, by increasing the resolution of the depth and wind data can be more accurately simulate wind-driven currents in the CS.

5. Acknowledgments

The numerical simulations were performed under the Numerical Modeling and high performance computing laboratory at the department of Marine Physics, Tarbiat Modares University, Iran. This research is funded by "Development of a three-dimensional numerical hydrodynamic oceanic model for Caspian Sea" project.

6. References

1- Watanabe, I., Kunito, T., Tanabe, S., Amano, M., Koyama, Y., Miyazaki, N., Petrov, E. and

Tatsukawa, R., (2002), *Accumulation of heavy metals in Caspian seals (Phoca caspica)*, Archives of Environmental Contamination and Toxicology, vol.43, p.109-120.

2- Mora, S., (2006), *An assessment of marine pollution in the Caspian Sea based on the CEP 2005 contaminant survey*, Caspian Environmental Programme.Akhverdiev, I. and Demin, Y., (1989), *O structure sinopticheskih techeniy Kaspiiskogo morya v letniy sezon po rezultatam diagnosticheskih raschetov. Kaspiiskoe more. Struktura i dinamika vod*, edited by: Kosarev, AN, Nauka, Moscow, USSR, 5-15.

3- Kosarev, A.N. and Yablonskaya, E., (1994), *The Caspian Sea*, SPB Academic Publishing The Hague.

4- Ibrayev, R., Özsoy, E., Schrum, C. and Sur, H., (2010), *Seasonal variability of the Caspian Sea three-dimensional circulation, sea level and air-sea interaction*, Ocean Science Discussions 6, p.1913–1970.

5- Kara, A., Wallcraft, A.J., Joseph Metzger, E. and Gunduz, M., (2010), *Impacts of freshwater on the seasonal variations of surface salinity and circulation in the Caspian Sea*, Continental Shelf Research vol. 30, p.1211-1225.

6- Terziev, F., Kosarev, A. and Kerimov, A., (1992), *Hydrometeorology and Hydrochemistry of the USSR Seas, V6, The Caspian Sea, Issue 1 Hydrometeorological Conditions*, Gidrometeoizdat, St. Petersburg.

7- Trukhchev, D., Kosarev, A., Ivanova, D. and Tuzhilkin, V., (1995), *Numerical analysis of the general circulation in the Caspian Sea*, Dokladi na Bulgarskata Akademia na Naukite, vol. 48, p.31-34.

8- Ibrayev, R., (2001), *Model of enclosed and semi-enclosed sea hydrodynamics*, Russian Journal of Numerical Analysis and Mathematical Modelling, vol. 16, p.291-304.

9- Katunin, D. and Sapozhnikov, V., (1997), *Complex Studies of the Southern Caspian Ecosystem (Seasonal Surveys at the Research Vessel Gilyan of the Russian-Iranian Expedition, August–September 1994–February 1996)*, Okeanologiya, vol. 37, p.152-154.

10- Tuzhilkin, V., Kosarev, A., Trukhchev, D. and Ivanova, D., (1997), *Seasonal features of general circulation in the Caspian deep water part*, Meteorology and Hydrology, vol. 1, p.91-99.

11- Badalov, A. and Rzheplinski, D., (1989), *Modelirovanie dinamiki deyatelnogo sloya Kaspiiskogo morya pod deystviem sinopticheskih atmosfernyh prosessov. Modelirovanie gidrofizicheskih prosessov i poley v zamknutyh vodoemah i moryah*, Nauka, Moscow, edited by: Sarkisyan, AS, USSR, 31-51

12- Sarkisyan, A., Zaripov, B., Kosarev, A. and Rzheplinski, D., (1976), *Diagnosticheskie raschety techeniy v Kaspiiskom more*, Izvestiya RAN, Atmospheric and Oceanic Physics, vol. 12, p.1106-1110.

13- Akhverdiev, I. and Demin, Y., (1989), *O structure sinopticheskih techeniy Kaspiiskogo morya v letniy sezon po rezultatam diagnosticheskih raschetov. Kaspiiskoe more. Struktura i dinamika vod*, edited by: Kosarev, AN, Nauka, Moscow, USSR, 5-15.

14- Korotenko, K., Mamedov, R., Kontar, A. and Korotenko, L., (2004), *Particle tracking method in the approach for prediction of oil slick transport in the sea: modelling oil pollution resulting from river input*, Journal of Marine Systems, vol. 48, p.159-170.

15- Kara, A., Wallcraft, A.J., Joseph Metzger, E. and Gunduz, M., (2010), *Impacts of freshwater on the seasonal variations of surface salinity and circulation in the Caspian Sea*, Continental Shelf Research vol. 30, p.1211-1225.

16- Gunduz, M. and Özsoy, E., (2013), *Modelling Seasonal Circulation and Thermohaline Structure of the Caspian Sea*, Ocean Science Discussions, 11. 10.5194/osd-11-259-2014.

17- Ibrayev, R., Sarkisyan, A. and Trukhchev, D., (2001), *Seasonal variability of circulation in the Caspian Sea reconstructed from normal hydrological data*, Izvestiia RAN, Atmospheric and Oceanic Physics, vol. 37, p.96-104.

18- Zounemat Kermani, M. and Sabbagh Yazdi, S.R., (2010), *Conjunction of 2D and 3D modified flow solvers for simulating spatio-temporal wind induced hydrodynamics in the Caspian Sea*, Ocean Science, vol. 45, p.113-128.

19- Kitazawa, D. and Yang, J., (2012), *Numerical analysis of water circulation and thermohaline structures in the Caspian Sea*, Journal of marine science and technology, vol. 17, p.168-180.

20- Nasimi, S. and Ghiassi, R., (2006), *A three-dimensional model of water circulation and temperature structure in the Caspian Sea*. Environmental Problems in Coastal Regions VI: p.261-272.

21- Phillips, N.A., (1957), *A coordinate system having some special advantages for numerical forecasting*, Journal of Meteorology, vol. 14, p.184-185.

22- Kasahara, A., (1974), *Various vertical coordinate systems used for numerical weather prediction*, Monthly Weather Review, vol. 102, p.509-522.

23- Gill, A.E., (2016), *Atmosphere and Ocean Dynamics*, Academic Press, New York.

24- Haltiner, G.J.W. and Williams, R., (1980), *Numerical prediction and dynamic meteorology*, 2nd Edition, Wiley, New York, 496 p.

25- Wu, J., (1982), *Wind-stress coefficients over sea surface from breeze to hurricane*, Journal of Geophysical Research, vol. 87, p.9704-9706.

26- Nihoul, J.C., (1977), *Three-dimensional model of tides and storm surges in a shallow well-mixed continental sea*, Dynamics of Atmospheres and Oceans, vol. 2, p.29-47.

27- Li, Y. and Zhan, J., (1993), *An efficient three-dimensional semi-implicit finite element scheme for simulation of free surface flows*, International journal for numerical methods in fluids, vol. 16, p.187-198.

28- Ibraev, I., Ozsoy, E., Ametistova, L., Sarkisyan, A. and Sur, H., (1998), *Seasonal variability of the Caspian Sea dynamics: barotropic motion driven by climatic wind stress and Volga River discharge*, In: Konstantin Fedorov Memorial Symposium, Sankt-Petersburg, Pushkin, St. Petersburg, p.18-22.

29- Lednev, V., (1943), *Techeniya Severnogo i Srednego Kaspiya*. Morskoy Transport, Moscow, USSR.

30- Peeters, F., Kipfer, R., Achermann, D., Hofer, M., Aeschbach-Hertig, W., Beyerle, U., Imboden, D.M., Rozanski, K. and Fröhlich, K., (2000), *Analysis of deep-water exchange in the Caspian Sea based on environmental tracers*, Deep Sea Research Part I: Oceanographic Research Papers, vol. 47, p.621-654.

31- Ghaffari, P., Isachsen, P. and LaCasce, J., (2013), *Topographic effects on current variability in the Caspian Sea*, Journal of Geophysical Research, Oceans 118, p.7107-7116.